UNIVERSITAT DE BARCELONA

Meson-Baryon interactions from effective Chiral Lagrangians

Albert Feijoo Aliau

Meson-Baryon interactions from effective Chiral Lagrangians.

Albert Feijoo Aliau

Departament de Física Quàntica i Astrofísica
Universitat de Barcelona

UNIVERSITAT DE
BARCELONA

Meson-Baryon interactions from effective Chiral Lagrangians.

Albert Feijoo Aliau

PhD thesis
Barcelona, April 2017.

Programa de Doctorat de Física,
Línia de Física de partícules i gravitació.

Departament de Física Quàntica i Astrofísica
Universitat de Barcelona.

Thesis advisors:
Volodymyr Magas and Àngels Ramos Gómez.

Thesis tutor:
Àngels Ramos Gómez.

A mis chicas y a mi padre

Contents

Agradecimientos

Este apartado quizá resulte el más difícil de todos, ya no por lo inevitable de dejarse cosas en el tintero, sino por ser la consumación de algo muy bueno en el plano personal. Éste no es uno de aquellos momentos donde coger el botín y quemar las naves bastaría. Me gustaría que fuese un imperativo con un doctorado de retraso. Escribir estas líneas significa retrotraerse al día en que me reuní con Volodymyr y Àngels para hablar de mi posible trabajo de máster y decirme que valdrá la pena. Ha valido la pena aprender de vosotros, ha valido la pena disfrutar de la física a vuestro lado; pero sobretodo, ha valido mucho la pena conoceros. Àngels y Volodymyr, os agradezco lo mucho que os habéis implicado en ésto, la ayuda y el apoyo recibido, la cercanía con la que me tratáis y esa incombustible energía positiva que contagia a cualquiera alrededor. Me habéis enseñado cómo trabajar con rigor, a desgranar las cosas y abordarlas sin pudor y con honestidad, y a huir de posturas contumaces. Gracias y mil veces gracias por vuestro ejemplo.

Durante este tiempo he tenido la fortuna de compartir despacho con Glòria, Àxel, Pere y Jordi a los que les agradezco la buena sintonía y el compañerismo generado entre nosotros. Concretamente, me gustaría resaltar la bonhomía y predisposición de todos ellos a lo largo de este trayecto.

Es ineludible no mencionar la cálida acogida que he recibido por parte de la pequeña família que conforman Artur, Assum, Bruno, Laura, Martin y Joan Carles junto a mis

directores. A ellos les debo buenos consejos, una imponderable dosis de buen humor y un agradecimiento sincero por su amistad.

Me gustaría tener unas palabras de agradecimiento para Eulogio Oset del cual he tenido la oportunidad de aprender mucho directa e indirectamente. La pasión e intensidad con las que trabajas hacen de la física un tren del que uno no quiera apearse.

Permitidme la falta de rigor al referirme a este departamento, aunque ya extinto, como 'Estructura i Constituents de la Matèria'. Sólo tengo palabras de agradecimiento para el exquisito trato que siempre he recibido por parte de todo el personal de ECM, ya sea con los profesores con los cuales he compartido docencia o con la dirección del mismo. Ha sido un honor poder pertenecer a este departamento. Asímismo, extender este agradecimiento al staff técnico y administrativo de quienes he recibido una gran predisposición y ayuda.

No podía dejar de agradecer a mi hermana Ruth su apoyo y cariño, el saber que siempre puedo confiar en ti y por hacerme participe de tu familia. Especialmente, de mis preciosas sobrinas a las cuales debo las mejores tardes de juegos que nunca he tenido.

Madre, nos has legado lo mejor que una madre puede transmitir a los hijos, una actitud vital de la cual tomar ejemplo. Tu lucha incansable por tu familia, la generosidad mostrada con tus sacrificios que casi te ha desdibujado, la destreza con la que has desempeñado un papel dual en nuestras vidas y tu ímpetu para seguir adelante. Gracias por tu categoría humana.

Cris, gracias por tu apoyo incondicional, por tu comprensión y paciencia, por tu profundo respeto hacia este proyecto personal y por enseñarme que una suma es el mejor de los operadores.

This part is maybe the most difficult to write, not because of the inevitability of leaving things unsaid but because of a reluctance to finalize a very fulfilling period of my life. This is not one of those moments when taking your life in your hands and burning your boats could be enough. With hindsight I would not have hesitated to undertake this doctorate. Writing these lines means turning my thoughts back to the day that I met Volodymyr and Àngels for the first time to talk about the subject matter of my Master's degree and telling myself it was all worth it. It has been most worthwhile learning from you all, worthwhile enjoying the physics at your side and worthwhile knowing you all. Àngels and Volodymyr, I thank you both for being involved in my time at the university, for your help and the support I have received, how close you have been and for your never ending supply of contagious enthusiasm for everybody in contact with yourselves. You have shown me how to work rigorously, to break things down, to be fearless while being honest and open-minded. A thousand thanks for setting me such a good example.

During this time I have had the good fortune of sharing an office with Àxel, Pere and Jordi whom I thank for the harmonious atmosphere and for the friendship shared between us. I would specially like to highlight the bonhomie and helpfulness of all of them.

It would be unthinkable not to mention the small family consisting of Artur, Assum, Bruno, Laura, Martin and Joan Carles, in addition to my advisors, for welcoming me so warmly into their midst. I owe them a great deal for good advice, for an uncountable amount of laughter and I sincerely appreciate their valuable friendship.

I would like to say a few words of appreciation regarding Eulogio Oset from whom I had the opportunity of learning so much, directly and indirectly. The passion and intensity with which you work makes physics a train from which you never want to get off.

Allow me the liberty of referring to this department although it no longer exists as 'Estructura i Constituents de la Matèria'. I only have words of appreciation for the excellent treatment that I have received at the hands of all the personnel, whether it be the lecturers with whom I have shared teaching or with the management of the department. It has been an honour to be a member of this department. Likewise, I would like to extend my appreciation to the technical and administrative staff from whom I have received great help and support.

Introduction

The increasing amount of hadrons which were discovered in the middle of the past century as well as their finite sizes, together with their anomalous magnetic moments, were the first hints that made the community of particle and nuclear physicists suggest the existence of a substructure by means of which hadrons break down into more fundamental degrees of freedom. These building blocks are called quarks for which six flavours can be distinguished, namely, u (up), d (down), s (strange), c (charm), b (bottom), and t (top). Hadrons are basically divided into two groups: mesons which have an antiquark-quark pair ($\bar{q}q$), while baryons consist of three quarks (qqq). However, other exotic configurations, such as pentaquarks, tetraquarks, glueballs or hadron molecules, depending on the number of their constituents can also exist.

The existence of spin-$\frac{3}{2}$ baryons, such as the $\Delta^{++}(uuu)$, $\Delta^{-}(ddd)$ or $\Omega^{-}(sss)$ seems to be in contradiction with the Pauli Exclusion Principle. Since quarks are spin-$\frac{1}{2}$ fields, two quarks being in the same state cannot have identical quantum numbers. For this reason only two quarks with opposite third spin component $(\frac{1}{2}, -\frac{1}{2})$ could share the

same orbital quantum numbers. Hence, the introduction of a new quantum number, namely the colour, was mandatory.

Quantum Chromodynamics (QCD) is a gauge theory that describes the strong interaction with colour $SU(3)$ as the underlying gauge group. Such a theory must include a proper mathematical formalism to deal with the complex composition of hadrons as well as incorporating all the symmetries satisfied by the interaction. The $SU(3)$ gauge invariance of the lagrangian in question requires the presence of vector fields, namely gluons, coupling to the fermions via the covariant derivative. But the constraint by means of which the vector fields should transform under $SU(3)$ carries consequences for the gauge field part of the lagrangian. The field strength tensor needs to be redefined by including an extra term in order to get rid of terms which appear in the transformed gauge field part of the lagrangian. This extra term introduces self-interactions of the gauge fields, specifically vertices involving three and four vector fields. In fact, this effect is general in all gauge theories based on Non-Abelian gauge symmetries. Consequently, it is straightforward to see that the eight gluon fields, as many as there are generators of the colour $SU(3)$ group, not only act as mediators of the interaction but they also interact between themselves.

Apart from the local colour symmetry, QCD exhibits further global symmetries. One of these concerns the fact that the difference in the number of quarks and anti-quarks for each flavour is a constant of motion. This is an exact symmetry of QCD which is independent of the quark mass, which is the reason why its origin is a global invariance under a direct product of $U(1)$ for each quark flavour. Other symmetries can be considered. The $SU(3)$ flavour symmetry is more or less satisfied by considering the u-,d- and s- masses as being almost equal and by neglecting electromagnetic

effects, since the hadron spectrum might be organized in terms of degenerate states of the same basis. The extension to $SU(6)$ is barely satisfied. From now on, we will only pay atention to the three light quarks.

In the limit in which the masses of the light quark tend to zero, QCD has an extra symmetry by means of which the unitary flavour transformations are separately applied to right- and left-handed quark fields. The group associated with these transformations is called $SU(3)_R \times SU(3)_L$, implying 16 conserved Noether currents in contrast to the 8 currents which appear in the simple $SU(3)$ flavour symmetry group. This symmetry is referred to as Chiral symmetry. As it is expected, if we restore the mass term into the QCD Lagrangian this symmetry is explicitly broken.

It is a remarkable fact that when the pseudoscalar mesons are compared with the vector mesons, a large mass gap arises between the isospin triplet of pions (150 MeV) and the isospin triplet of ρ mesons (770 MeV). This gap remains, although to a lesser extent, between the multiplets involving strange mesons. This could be understood as a signal of the special role played by the pseudoscalar mesons as Nambu-Goldstone bosons which point out towards a spontaneous breaking of the chiral symmetry. In general, Goldstone's theorem states that for any broken global symmetry of a given Lagragian a massless boson must exist. The pseudoscalar mesons ($\pi^{\pm}, \pi^0, K^0, \bar{K}^0, K^{\pm}, \eta$) are not massless, but this is solely a consequence of the nonzero light quark masses. The first chapter of this thesis presents details about these issues.

The running coupling strength $\alpha_s = g_s^2/4\pi$, which characterizes the strong interaction in QCD, has the following dependence on the energy scale μ

$$\alpha_s(\mu) = \frac{4\pi}{\beta_0 \ln(\frac{\mu^2}{\Lambda^2})} \tag{1}$$

where $\beta_0 = 11 - 2N_f/3$, $\Lambda \approx 0.2$ GeV and N_f is the number of possible flavours. QCD behaves in a simple way at high momentum transfers above several GeV, where it accepts a perturbative treatment in terms of powers of the running coupling constant. This is feasible due to the sufficiently weak quark-gluon coupling. In opposition to this, at low energies and momenta ($\mu < 1$ GeV) where most of the hadronic and nuclear processes take place, α_s becomes larger than 1 and, consequently, an expansion in powers of the running coupling strength diverges making this procedure impossible. In order to overcome the previous difficulty, one has to turn to effective lagrangians which are based on the same symmetries and symmetry breaking patterns of QCD. In such an energy region, under this reformulated QCD, composite hadronic quasi-particles become the fundamental degrees of freedom instead of the elementary quarks and gluons.

Chiral Perturbation Theory (ChPT) is an effective theory which has proved to be appropriate to describe the interaction of hadrons at low energies. Specifically, up to the characteristic energy scale $\Lambda_{ChPT} \sim 1$ GeV , the pseudoscalar mesons, which can be considered the softest exitations of the QCD ground state, should govern the physics therein. As we have mentioned before, this fact can be understood by the invariance under chiral symmetry for the light quark sector which spontaneously breaks down giving rise to these Goldstone bosons. The very nature of the chiral Goldstone bosons strongly constrains the symmetry conditions to be imposed on the Effective Lagrangian [1–6]. In ChPT, the dynamics is described by arranging the Effective Lagrangian as an expansion on the powers of the external momenta of the Goldstone bosons over Λ_{ChPT}. Although the strong constraints imposed by chiral-symmetry-breaking allow one to take into consideration processes which are restricted to the energy limit given by Λ_{ChPT}, ChPT has only proved to be valid up to energies around

500 MeV. Moreover, Effective Chiral theories have drawbacks when a resonance appears in the region of interest, unless we have included it as an explicit degree of freedom in the corresponding field, since it is associated to a pole in the scattering amplitude which cannot be reproduced by means of a perturbative expansion. Due to the previous facts, nonperturbative schemes need to be developed in order to get around this difficulty while maintaining the predictive power of the theory. In addition, the energy region where such an approach can be applied becomes larger compared to the validity region of ChPT.

The meson-baryon interaction in the $S = -1$ sector is one of those scenarios which require a nonperturbative resummation of ChPT, since the $\bar{K}N$ interaction is strong enough to produce a "quasi-bound" state, associated with the $\Lambda(1405)$ resonance, which is located only 27 MeV below the $\bar{K}N$ threshold. Since the late nineties, numerous studies [7–17] have been devoted to this topic, but the latest more precise measurements of the energy shift and width of the 1s state in kaonic hydrogen by the SIDDHARTA collaboration [18] at DAΦNE have renewed the interest in these last years. As a response to the need to extend the approach to higher orders aiming for a greater accuracy in describing these new experimental data, the theoretical models have been revisited [19–26].

In Chapter 2 of the present work we address this issue taking into account the descriptive power of the Unitarized Chiral Perturbation Theory (UChPT) approach. We study the meson-baryon interaction in s-wave for different two body channels present in the $S = -1$ sector by means of a chiral lagrangian up to next-to-leading order (NLO) and implementing unitarization in coupled channels. This necessarily passes through the determination of the low energy constants, particularly those which are not well

established yet, namely the NLO coefficients. One should bear in mind that these parameters, which appear in the expansion of ChPT, are not fixed by the symmetries which the theory is based on, but the values come from fits to the experimental data. This could be a very hard and tedious task, almost intractable if we go to higher orders than NLO, due to the appearance of a rapidly increasing number of free parameters as one increases the order of the calculation.

The novelty of our work lies in the fact that we pay a special attention to the $K^- p \to K\Xi$ reactions, which offer us good complementary information to determine the low energy constants. Actually, as far as we know, our study is the first to consider the reproduction of $K\Xi$ production cross section employing chiral models in [27].

The reason for the special role of the $K\Xi$ production channels stems from the fact that the $K^- p \to K\Xi$ reactions receive a null contribution from the Weinberg-Tomozawa (WT) term, which is the dominant one at leading order (LO), and the rescattering terms due to the coupled channels are not sufficient to reproduce the experimental scattering data. This fact confers an interesting role to the $K^- p \to K\Xi$ reactions as a privileged framework in the $S = -1$ sector to get information about the next terms in the hierachy beyond the WT one, namely the direct and cross Born terms present at LO and the NLO term. From studies which were based on lagrangians extended to NLO [15,19,23], one finds that the contribution of the cross and direct Born terms is very moderate. Assuming this and for simplicity, the Born contributions are disregarded in the first stage of our study leaving only the NLO term as the significant one in order to reach good agreement between the theoretical predictions and the experimental data in the $K\Xi$ channels. The possible relevance acquired by NLO contributions is the seed from which this thesis arises, since we are interested in obtaining more reliable values for

the NLO constants at low energy.

We fit our model to the branching ratios at K^-p threshold, the precise SIDDHARTA values of the shift and width of the 1s state of the kaonic hydrogen and the cross-sections for the different two body channels ($\pi\Sigma, \pi\Lambda, \bar{K}N, K\Xi$) by means of the minimization techniques embedded in the MINUIT package. After comparing different fitting procedures, the sensitivity of the $K^-p \to K\Xi$ reactions to the NLO term of the chiral Lagrangian is demonstrated and, therefore, more reliable values of the low energy constants are obtained.

The natural next stage of our work was to determine whether the assumption of a non significant contribution of the Born diagrams in the interaction kernel is still realistic, once the $K\Xi$ channels are included in the fits. This is the aim of our study of Ref. [28] which is also presented in Chapter 2. We will see that, merely employing a chiral model which takes into account the Born terms, the particular importance of these diagrams in the $K\Xi$ channels are revealed by significant modifications of the NLO parameters. In fact, we find an equally shared role of the NLO and the Born terms. The relevance of the Born terms becomes even more visible in the isospin projected amplitudes of the $K^-p \to K\Xi$ reactions, which differ substantially from what was found for the models that ignored these contributions. This fact points towards the idea that processes that filter a single isospin component are an essential requirement to get much more reliable values for the NLO coefficients. Consequently, we finish this chapter by developing a new model that includes experimental data from the $K^-p \to \eta\Lambda, \eta\Sigma^0$ reactions in the fitting procedure which are the most natural filtering processes that might be provided. These two reactions are very useful to discriminate possible ambiguities in the isospin distributions since they are pure $I = 0$

and $I = 1$ processes, respectively. In addition, motivated by the recent proposal [29] of creating a secondary K_L^0 beam at Jlab that offers a great opportunity for measuring the $K_L^0 p \to K^+\Xi^0$ reaction, we also present a prediction for this $I = 1$ filtering process.

In order to study the accuracy and stability of our parameters, we include high spin and high mass resonances applying the Rarita-Schwinger method [30–32]. This method permits building resonant amplitudes that we add explicitly to our chiral scattering amplitude, aiming for studying their effects on the NLO coefficients. Based on the phenomenological study of [32] and in our previous work [27], we choose as candidates the $\Sigma(2030)$, $\Sigma(2250)$ and $\Lambda(1890)$ resonances and, as we will see in Chapter 3, we achieve very good agreement with the experimental data. As expected, we obtain a more precise and trustable determination of the corresponding NLO parameters.

In order to provide new isospin filtering scenarios from which we can extract additional information to constrain even more the NLO coefficients, we study the weak decay of the Λ_b into $J/\psi\ K\ \Xi$ and $J/\psi\ \eta\ \Lambda$ states based on our work of Ref. [33]. These processes involve an elementary weak transition at the quark level, which proceeds via the creation of a $c\bar{c}(J/\psi)$ meson and an excited sud system with $I = 0$ that hadronizes into a final $I = 0$ meson-baryon pair. Thus, an experimental determination of these decays would contribute to a better understanding of the chiral dynamics at higher energies. The results of this study are shown and discussed in Chapter 4, where we also present the results of our exploratory study about the possibility of finding a hidden-charm strange pentaquark in the decay of the Λ_b into the $J/\psi\ \eta\ \Lambda$ from the invariant mass spectrum of $J/\psi\ \Lambda$ pairs. This study is analogous to the one carried out in [34], but implementing the new developed models in final meson-baryon interaction. Hidden charm pentaquark states of molecular nature are advocated by some unitary

approaches [35–39] that also predict pentaquark partners in the strangeness $S = -1$ sector. Our study is motivated by the fact that the recent observation of the hidden charm pentaquark state $P_c(4450)$ at LHCb via the $\Lambda_b \to J/\psi\ K^-\ p$ decay [40,41] is well reproduced by the molecular state implemented in the analysis of Ref. [42]. We study the dependence of our results on reasonable changes in the parameters of the models as well as on the unknown properties of the speculated hidden charm strange pentaquark. We observe that, while there appear changes in the position of the peak and in the shapes of the distributions, a resonance signal in the $J/\psi\Lambda$ invariant mass spectrum is clearly seen in all the cases. This gives us confidence that such an experimental study could result into a successful proof of the existence of this new state.

Chapter 1

Chiral unitary approach

The non-abelian character of QCD is reflected in the twofold very nature of gluons. They do not act only as colour carriers but they also, joinly with quarks, are the fundamental elements sensitive to the strong force. Thus, it is easy to see why the strength of the interaction between these elements depends on the transferred energy of the gluons involved in such an interaction process. The strong interaction between quarks behaves in such a way that it reaches large values for the coupling strength for small momentum transfers, while in the limit of large momentum transfers the coupling strength tends to zero. This double behaviour demonstrated by QCD is not an abnormal situation in physics, and is generally handled by studying the behaviour of the same physical system on separate scales by means of different approaches. Therefore, the application of a particular physical mechanism rather than another to describe a process is completely subordinated to the scale at which the process takes place. The validity of each mechanism is determined by certain control parameter which characterizes the system. An example of this fact would be the negligible relativistic

effects in our everyday experience where the velocities are far less than the speed of light, $v \ll c$. There is no conceptual difference on extrapolating this idea to QCD, a theory which fails in describing low-energy phenomena pertubatively while this method is completely valid at a higher energy scale. Such an idea is the foundation of the Effective Field Theories (EFTs) whose domain of validity is limited below some scale. In order to address our low-energy hadron physics phenomena by means of an EFT, it is crucial to identify a clear scale-spacing. In connection with this, we pointed out in the introduction that the hadronic spectrum is distributed in a peculiar fashion on both sides of a gap along the energy range as can be seen form Fig. 1.1. Indeed, there are a large number of meson resonances and baryons above 1 GeV while only a few pseudoscalar states are present in a lighter mass region. This is explicitly seen from the values of the masses of these pseudoscalar mesons $M_\pi \approx 140$ MeV, $M_K \approx 495$ MeV and $M_\eta \approx 550$ MeV in comparison with the masses of the rest of mesons and baryons. In fact, this energy scale of ($\Lambda_{ChPT} \approx 1$ GeV) allows us to define a small parameter as the mass and momentum of the interacting particles, denoted by p here, over this factor $\left(\frac{p}{\Lambda_{ChPT}}\right)$. The systematic expansion in powers of this parameter basically constitutes the effective lagrangian which describes the system at the given energy scale. This procedure is nothing but the way to carry out the approximation known as EFT. Let us comment in addition that there need not be any matching between the degrees of freedom present in the EFT with the ones from the fundamental theory. For instance, Chiral Perturbation Theory (ChPT) [1,43] is formulated in terms of hadrons as degrees of freedom instead of quarks and gluons, which are the corresponding degrees of freedom for QCD. Regardless of the approach used to describe a physical phenomenon, the system which is intended to be studied should maintain the nature of the interaction that governs this process. This nature is encoded in the symmetries, which reveal

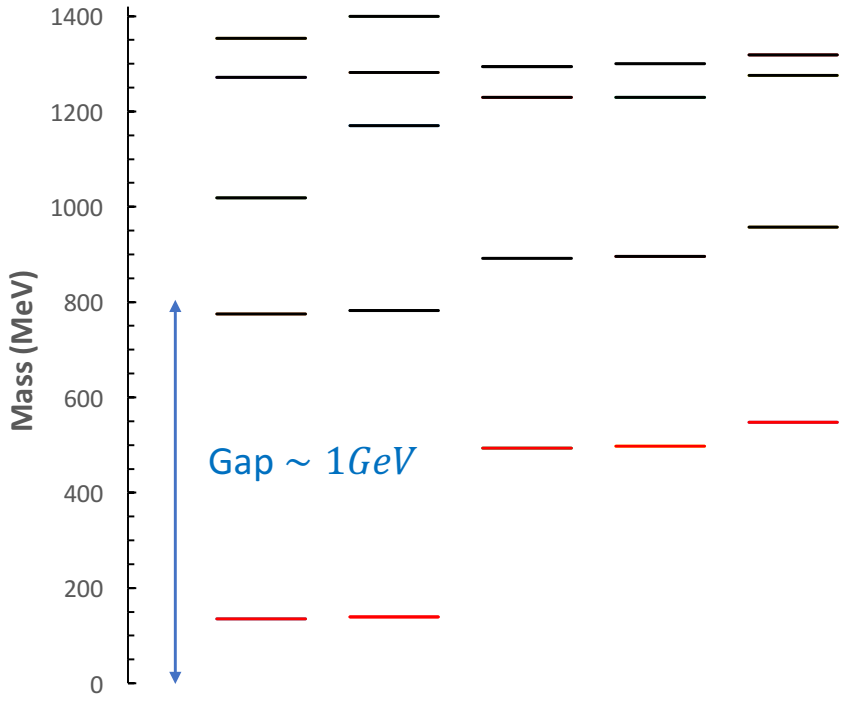

Figure 1.1: Spectrum of the mesons containing $u(\bar{u}), d(\bar{d}), s(\bar{s})$ quarks up to 1400 MeV. The corresponding masses are taken from [44], but excluding the controversial mesons. The pseudoscalar octet is represented in red, from left to right: π^0, $\pi^{\pm}$, $K^{\pm}$, $(\bar{K}^0, K^0)$, η. While the rest of mesons are represented by the black segments in increasing order of mass, namely: $(\rho^0, \rho^{\pm})$, ω, $K^{*\pm}$, $(\bar{K}^{*0}, K^{*0})$, η', ϕ, $h_1(1170)$, $b_1(1235)$, $a_1(1260)$, $f_2(1270)$, $K_1(1270)$, $f_1(1285)$, $\eta(1295)$, $\pi_1(1400)$, $K_1(1400)$.

the invariance of the system under certain transformations. Therefore, the inherent symmetry principles must be present, whether we employ a fundamental theory or an effective one to describe, in this case, the strong interaction. Apart from the local $SU(3)$ colour gauge symmetry which constitutes the basis of the formulation of QCD, and besides the obvious symmetries like Lorentz-invariance and the discrete symmetries of parity (P), charge conjugation (C) and time reversal (T), the strong interaction of hadrons is governed by another global unitary symmetry: the chiral symmetry. We are going to pay special attention to this last symmetry due to the relevant role played in

the strong-interaction processes at low energies.

1.1 Chiral symmetry in QCD

The global $SU(3)_L \times SU(3)_R \times U(1)_V$ symmetry of the QCD Lagrangian in the limit of massless light quarks is the basis of ChPT. This limit is hoped to be not too far of the real world since the masses of the three light quarks are small on the typical hadronic scale ($m_u = 0.005$ GeV, $m_d = 0.009$ GeV, $m_s = 0.175$ GeV $\ll \Lambda_{ChPT}$). With this assumption, the three-flavour massless QCD Lagrangian is given by

$$\mathcal{L}^0_{QCD} = \bar{q} i\gamma^\mu D_\mu q - \frac{1}{4} G^a_{\mu\nu} G^{\mu\nu}_a \tag{1.1}$$

which comes in terms of the covariant derivative that is independent of the flavour and which is defined as

$$D_\mu = \partial_\mu - ig \sum_{a=1}^{8} \frac{\lambda_a}{2} A^a_\mu \tag{1.2}$$

and where the gluonic field tensor reads

$$G^a_{\mu\nu} = \partial_\mu A^a_\nu - \partial_\nu A^a_\mu + g f_{abc} A^b_\nu A^c_\mu \tag{1.3}$$

being $q^T = (u\ d\ s)$ the quark field, A^a_μ the eight gluon fields, each of which identifiable by the a label ($a = 1 - 8$), and λ_a the so-called Gell-Mann matrices, which satisfy the commutation relation $\left[\frac{\lambda_a}{2}, \frac{\lambda_b}{2}\right] = i f_{abc} \frac{\lambda_c}{2}$ with the corresponding structure constant f_{abc}.

At this point, we need to take into account some definitions and concepts to a better

comprehension of the chiral symmetry which is exhibited by the QCD Lagrangian (1.1). To this end, we introduce the right-handed (R index) and left-handed (L index) projection operators

$$P_R = \frac{1}{2}(1+\gamma_5) = \frac{1}{2}\begin{pmatrix} 1_{2\times 2} & 1_{2\times 2} \\ 1_{2\times 2} & 1_{2\times 2} \end{pmatrix} = P_R^\dagger, \tag{1.4}$$

$$P_L = \frac{1}{2}(1-\gamma_5) = \frac{1}{2}\begin{pmatrix} 1_{2\times 2} & -1_{2\times 2} \\ -1_{2\times 2} & 1_{2\times 2} \end{pmatrix} = P_L^\dagger, \tag{1.5}$$

with the chirality matrix γ_5 defined as $\gamma_5 = i\gamma^0\gamma^1\gamma^2\gamma^3$, and satisfying $\{\gamma^\mu, \gamma_5\} = 0$ and $\gamma_5^2 = 1$.

The completeness, idempotence and orthogonality relations can be proved from eq. (1.4) and eq. (1.5):

$$P_R + P_L = 1, \qquad P_R^2 = P_R, \quad P_L^2 = P_L, \qquad P_R P_L = P_L P_R = 0. \tag{1.6}$$

Given the nature of P_R and P_L as projection operators, one can obtain new states projecting P_R and P_L onto the Dirac field q:

$$q_R = P_R q \qquad\qquad q_L = P_L q \ . \tag{1.7}$$

These states are eigen-states of the chirality matrix.

$$\gamma_5 q_R = q_R \qquad\qquad \gamma_5 q_L = -q_L \ . \tag{1.8}$$

Although chiral fields have been defined above, chirality seems to be a non intuitive concept. In order to shed some light on this, one might focus on the helicity of a particle that is defined as the projection of the spin onto the direction of momentum. For massless particles or ultrarelativistic particles, particles for which the mass can be neglected with respect to energy, chirality and helicity become the same concept. Therefore, Chirality could be understood as the extension of the helicity. If we consider the positive-energy solution of the Dirac equation with three-momentum $\vec{p}$ and take the ultrarelativistic case, the terminology right- and left-handed fields can be easily illustrated, namely

$$u(\vec{p},\pm) = \sqrt{E+M}\begin{pmatrix} \chi_\pm \\ \frac{\vec{\sigma}\cdot\vec{p}}{E+M}\chi_\pm \end{pmatrix} \quad \begin{matrix} E \gg M \\ \longrightarrow \end{matrix} \quad u_\pm(\vec{p}) = \sqrt{E}\begin{pmatrix} \chi_\pm \\ \pm\chi_\pm \end{pmatrix}, \tag{1.9}$$

where it is assumed that the spin is parallel or anti-parallel to the direction of the momentum in the rest frame $\vec{\sigma}\cdot\hat{p}\chi_\pm = \pm\chi_\pm$.

When we apply the operators the P_R and P_L to the positive and negative helicity eigenstates $u_\pm$, we obtain

$$P_R u_+ = \frac{\sqrt{E}}{2}\begin{pmatrix} 1_{2\times2} & 1_{2\times2} \\ 1_{2\times2} & 1_{2\times2} \end{pmatrix}\begin{pmatrix} \chi_+ \\ \chi_+ \end{pmatrix} = u_+, \tag{1.10}$$

and $P_R u_- = 0, \quad P_L u_+ = 0, \quad P_L u_- = u_-$. Therefore, the concept of chirality becomes the same as helicity in the ultrarelativistic or massless limit.

Before analysing the symmetry of the QCD Lagrangian with respect to independent global transformations of the left- and right-handed fields, it is convenient to express

the field q in terms of its q_R and q_L components as:

$$q = (P_R + P_L)q = P_R q + P_L q = q_R + q_L \tag{1.11}$$

Introducing this decomposition into eq. (1.1) the QCD Lagrangian is decoupled into two terms which are independent from each other. Thus, the QCD Lagrangian in the chiral limit can be written as

$$\mathcal{L}^0_{QCD} = \bar{q}_R i\gamma^\mu D_\mu q_R + \bar{q}_L i\gamma^\mu D_\mu q_L - \frac{1}{4} G^a_{\mu\nu} G^{\mu\nu}_a \tag{1.12}$$

As we have said, the covariant derivative is flavour independent, a fact that turns the $\mathcal{L}^0_{QCD}$ into an invariant under chiral $U(3)_L \times U(3)_R$ flavour transformations, that is to say a chiral $SU(3)$ symmetry in addition to the invariance under a global phase transformation ($U(3)_{L,R} = U(1)_{L,R} \times SU(3)_{L,R}$):

$$q_{R,L} \longrightarrow U_{R,L} q_{R,L} = \exp\left(-i \sum_{a=1}^{8} \alpha_a^{R,L} \frac{\lambda_a}{2}\right) \cdot \exp\left(-i\alpha^{R,L}\right) q_{R,L} \tag{1.13}$$

where $\alpha_a^{R,L}$ are real transformation parameters.

By virtue of Noether's theorem, there will be one conserved current for each satisfied symmetry. Because of the double $U(3) = SU(3) \times U(1)$ symmetry, one for the right-handed and another for the left-handed, we expect a total of $18 = 2 \times (8+1)$ conserved currents: 8 due to the fact that we are dealing with 3 possible flavours and, hence, we have $3^2 - 1$ generators and 1 associated to the phase transformation. These currents

are:

$$L^{\mu,a} = \bar{q}_L \gamma^\mu \frac{\lambda^a}{2} q_L, \qquad \partial_\mu L^{\mu,a} = 0, \tag{1.14}$$

$$R^{\mu,a} = \bar{q}_R \gamma^\mu \frac{\lambda^a}{2} q_R, \qquad \partial_\mu R^{\mu,a} = 0. \tag{1.15}$$

where we have extended the possible values of "a" in such a way that the values from 1 to 8 account for the generators of the unitary group acting on q while the extra $a = 0$ value accounts for the identity in order to include the phase transformation in this general formulation. For each conserved current, there is a time independent charge that is written by

$$\begin{aligned} Q_L^a &= \int d^3x L^{0,a}(x), \quad \dot{Q}_L^a = -i\,[Q_L^a, H] = 0, \\ Q_R^a &= \int d^3x R^{0,a}(x), \quad \dot{Q}_R^a = -i\,[Q_R^a, H] = 0. \end{aligned} \tag{1.16}$$

Alternatively, it is common to talk about vector ($V^{\mu,a}$) and axial ($A^{\mu,a}$) currents instead of the left- and right-handed currents. These currents are defined as linear combinations of the previous ones and they have their own associated charge.

$$\begin{aligned} V^{\mu,a} = R^{\mu,a} + L^{\mu,a} = \bar{q}\gamma^\mu \frac{\lambda^a}{2} q, \qquad Q_V^a = \textstyle\int d^3x V^{0,a}(x), \\ A^{\mu,a} = R^{\mu,a} - L^{\mu,a} = \bar{q}\gamma^\mu\gamma_5 \frac{\lambda^a}{2} q, \qquad Q_A^a = \textstyle\int d^3x A^{0,a}(x). \end{aligned} \tag{1.17}$$

If we particularize for the singlet vector current ($V^{\mu,0} = \bar{q}\gamma^\mu q$) , namely $a = 0$, we find that it is a conserved current in the standard model ($\partial_\mu V^{\mu,0} = 0$) and the corresponding charge Q_V^0 is the baryon number (properly normalized to 1/3). But this is not the case when we look at the singlet axial current ($A^{\mu,0} = \bar{q}\gamma^\mu\gamma_5 q$), where $\partial_\mu A^{\mu,0} \neq 0$ due to

quantum effects [45]. Consequently, the singlet axial current is not a conserved one.

For the rest of the sixteen currents ($V^{\mu,a}, A^{\mu,a}, a = 1 - 8$), the expressions (1.17) are also convenient for introducing the concept of the spontaneous chiral symmetry breaking (SSB) established by the phenomenology of the hadron spectrum [44], and also corroborated by lattice QCD calculations [46–49]. The key fact is that the QCD ground state or vacuum does not preserve the chiral symmetry of the underlying Lagrangian. There follows an explanation of this issue. If we want to conclude whether a symmetry is realized, one should check whether the ground state is necessarily invariant under the charges associated to the conserved currents of the symmetry. And conversely, a non-vanishing vacuum expectation value of some hermitian operator coming from the dynamics of the underlying theory tells us that there is SSB. Ultimately one has to study what happens to these operators acting over the vacuum: $Q_A^a|0\rangle$ and $Q_V^a|0\rangle$. One should bear in mind that $(Q_A^a|0\rangle, Q_V^a|0\rangle)$ are the variations with respect to the vacuum state when the chiral symmetry transformation is applied to this state. There is no doubt that in the non-degenerate state, with a single ground state, one finds $Q_A^a|0\rangle = Q_V^a|0\rangle = 0$, because there are no other states which are accessible, with the same energy, via the vector and the axial charges. Consequently, if this were the case, the symmetry would be satisfied leaving the unique vacuum state invariant. This way of realizing the symmetry is known as Wigner-Weyl mode. Otherwise, the ground state can consist of a finite number of distinct degenerate states. The $|\phi_A^a\rangle$ ($|\phi_A^a\rangle = Q_A^a|0\rangle$) and the $|\phi_V^a\rangle$ ($|\phi_V^a\rangle = Q_V^a|0\rangle$) states together with the ground state $|0\rangle$ are the constituents of this degenerate set of states which have associated the same energy whose value can be obtained from $H|0\rangle = E_0|0\rangle = 0|0\rangle = 0$. To check that this energy requirement is also fulfilled by the rest of the degenerate members of the set, one can make use of the conservation of the currents ($\partial_\mu A^{\mu,a} = 0, \partial_\mu V^{\mu,a} = 0$) and

their subsequent commutation of charges with the QCD Hamiltonian $\left[Q^a_{A,V}, H\right] = 0$.

$$\begin{aligned} H|\phi^a_A\rangle = HQ^a_A|0\rangle = Q^a_A H|0\rangle = Q^a_A E_0|0\rangle = 0 \\ H|\phi^a_V\rangle = HQ^a_V|0\rangle = Q^a_V H|0\rangle = Q^a_V E_0|0\rangle = 0 \end{aligned} \tag{1.18}$$

Actually, if this last possibility, which considers a degenerate ground state, is realized, then the hadron spectrum should reflect the existence of positive and negative parity degenerate excited states. The reason to this is justified because of the different parity assignments for the charges Q^a_A and Q^a_V that can be appreciated just by

$$\begin{aligned} P : |\phi^a_A\rangle = Q^a_A|0\rangle \quad &\rightarrow \quad PQ^a_A P^{-1} P|0\rangle = -Q^a_A p_{gs}|0\rangle = -p_{gs}|\phi^a_A\rangle \\ P : |\phi^a_V\rangle = Q^a_V|0\rangle \quad &\rightarrow \quad PQ^a_V P^{-1} P|0\rangle = Q^a_V p_{gs}|0\rangle = p_{gs}|\phi^a_V\rangle \end{aligned} \tag{1.19}$$

where P is the parity operator, p_{gs} is the intrinsic parity of the $|0\rangle$ state and where the negative sign obtained from the parity transformation of the axial charge operator is because it contains a γ_5 operator while the vector charge does not. But, as it is widely known, there are no such parity doublets in the hadron spectrum. For instance, the light pseudoscalar $J^\pi = 0^-$ mesons have no $J^\pi = 0^+$ partners, as the scalar mesons with these associated quantum numbers have much higher masses. Then we can conclude that this symmetry is spontaneously broken.

Apart from this heuristic argument, in 1984 Vafa and Witten, via their theorem [50], state that the flavour vector subgroup remains unbroken ($SU(3)_R \times SU(3)_L \rightarrow SU(3)_V$) which is corroborated by the observation of hadronic multiplets and implies $Q^a_V|0\rangle = 0$. This is not the case for the axial charge, whose value must be $Q^a_A|0\rangle \neq 0$ just for compatibility with the observed spectra. The Goldstone's theorem ensures the

existence of as many massless bosons ($H|\phi_A^a\rangle = 0$), the so-called Nambu-Goldstone (NG) bosons, as generators of the symmetry group which does not annihilate the vacuum. Therefore, resulting from the SSB, eight NG massless bosons are expected. This is in conflict with what is mentioned in the introduction, where these bosons were identified with the pseudoscalar mesons, which are massive particles as is widely known. This feature is one of the implications of the non zero masses of the three light quarks.

At the beginning of this section, we ignored the masses of the u-, d- and s-quarks because they are much smaller than the renormalization scale Λ_{ChPT}. This fact leads us to neglect the quark mass term in the QCD Lagrangian (1.1). But when this contribution is restored, the charge operators are in general no longer time independent which is the consequence of having an explicitly broken symmetry. To see this, we can rewrite the total QCD Lagrangian as

$$\mathcal{L}_{QCD} = \mathcal{L}^0_{QCD} + \mathcal{L}^M_{QCD} = \bar{q} i\gamma^\mu D_\mu q - \frac{1}{4} G^a_{\mu\nu} G^{\mu\nu}_a - \bar{q} M q \tag{1.20}$$

where M is defined as a diagonal matrix containing the different light quark masses

$$M = \begin{pmatrix} m_u & 0 & 0 \\ 0 & m_d & 0 \\ 0 & 0 & m_s \end{pmatrix}. \tag{1.21}$$

If we focus on this quark mass term, after expressing it in terms of the chiral fields, we clearly realize that the quark mass term breaks down into two pieces, each of which

mixes the left- and right-hand fields, thereby breaking chiral symmetry explicitly.

$$\mathcal{L}^{M}_{QCD} = -\bar{q}Mq = -\bar{q}_R M q_L + \bar{q}_L M q_R \tag{1.22}$$

1.2 Chiral Effective Field Theory

As it is mentioned in the introduction, QCD cannot be treated perturbatively at low energies due to the colour confinement where hadrons take the place of the asymptotic degrees of freedom instead of quarks and gluons. Our goal is to construct an effective field theory with hadronic degrees of freedom, preserving the symmetries of the underlying theory. The way to proceed in order to construct an EFT was established by S. Weinberg [43] which literally reads: " ... if one writes down the most general possible lagrangian, including all terms consistent with the assumed symmetry principles, and then calculates matrix elements with this lagrangian to any given order of perturbation theory, the result will simply be the most general possible S-matrix consistent with the analyticity, perturbative unitarity, cluster decomposition and the assumed principles...".

1.2.1 Chiral Perturbation Theory for Mesons

In the absence of baryons, this theory must be the most general one that describes the dynamics of the Goldstone bosons associated with the spontaneous breakdown in QCD. This means that our lagrangian should be invariant under a compact group $G = SU(3)_L \times SU(3)_R = \{(L,R)|L\,\epsilon\,SU(3)_L, R\,\epsilon\,SU(3)_R\}$ as well as under $U(1)_V$. But, by virtue of the spontaneous symmetry breaking which give rise to the Goldstone

bosons, the degenerated ground state should only be invariant to the subgroup H of G, $H = \{(V, V)|V \epsilon SU(3)\}$, and $U(1)_V$. Therefore, for the sake of the the invariance of the lagrangian under the $g \epsilon G$ transformations, an isomorphic mapping between the quotient group G/H and the NG bosons fields is needed. The Goldstone bosons octet can be collected in the matrix form as

$$\phi = \begin{pmatrix} \frac{1}{\sqrt{2}}\pi^0 + \frac{1}{\sqrt{6}}\eta & \pi^+ & K^+ \\ \pi^- & -\frac{1}{\sqrt{2}}\pi^0 + \frac{1}{\sqrt{6}}\eta & K^0 \\ K^- & \bar{K}^0 & -\frac{2}{\sqrt{6}}\eta \end{pmatrix}, \tag{1.23}$$

which consists of independent fields that are continuous functions on a four-dimensional Minkowski space.

The chiral fields which guarantee the chiral symmetry of the lagrangian, coming from the isomorphic mapping, are defined as

$$U(\phi) = u^2(\phi) = \exp\left(\sqrt{2}i\frac{\phi}{f}\right), \tag{1.24}$$

where f is the normalization constant of the NG boson and corresponds to the pseudoscalar decay constant in the chiral limit at tree level. This matrix transforms under the chiral right and left-handed rotations in the following way:

$$U \to RUL^\dagger. \tag{1.25}$$

Since we want to construct a low-energy effective theory, firstly only for mesons, an expansion in terms of powers of momentum should be developed. The chiral counting rule is introduced by considering the momentum of the meson, which appears after

every derivative of the chiral field, as a small quantity in comparison with the chiral symmetry breaking scale $4\pi f \approx 1$ GeV. Such a theory is valid in a region where the only relevant degrees of freedom are the NG bosons. Consequently, our main building blocks in order to write our lagrangian density must be the U matrix and its successive derivatives $(U, U^\dagger, \partial_\mu U, \partial_\mu U^\dagger, \dots)$ which are invariant under $SU(3)_L \times SU(3)_R$ as we have said above. But this is not the only symmetry requirement, for instance, the lagrangian must satisfy the Lorentz invariance which constrains the structure of the terms in a way that only even powers of derivatives can be present. Thus, our lagrangian can be expressed as:

$$\mathcal{L} = \mathcal{L}^{(0)} + \mathcal{L}^{(2)} + \mathcal{L}^{(4)} + \dots \tag{1.26}$$

here, the number in brackets points to the number of powers in each term.

Given that U is a quantity of order $O(p^0)$, the first term of this lagrangian ($\mathcal{L}^{(0)}$) is of the form $UU^\dagger$ which preserves the requested symmetries. This term due to the unitarity of the chiral field gives as a result a constant. Therefore, the leading term is $\mathcal{L}^{(2)}$ which involves derivatives of U. In this way one can express the most general effective lagrangian density with the minimal number of derivatives as

$$\mathcal{L}^{(2)} = \frac{f^2}{4}\langle \partial_\mu U \partial^\mu U^\dagger \rangle \tag{1.27}$$

and the symbol $\langle \dots \rangle$ stands for the trace. At this point, one should prove that this leading term of the lagrangian is invariant under the global $SU(3)_L \times SU(3)_R$ transfor-

mation. Aiming for this, let us first see how the derivative of the chiral field transforms

$$\begin{aligned} U &\rightarrow RUL^\dagger \\ \partial_\mu U &\rightarrow \partial_\mu(RUL^\dagger) = \partial_\mu RUL^\dagger + R\partial_\mu UL^\dagger + RU\partial_\mu L^\dagger = R\partial_\mu UL^\dagger \end{aligned} \tag{1.28}$$

where we have taken into account that $\partial_\mu R = \partial_\mu L^\dagger = 0$ because of the global nature of these transformations. In a similar manner, one finds that

$$\begin{aligned} U^\dagger &\rightarrow LU^\dagger R^\dagger \\ \partial^\mu U^\dagger &\rightarrow L\partial^\mu U^\dagger R^\dagger. \end{aligned} \tag{1.29}$$

With the previous considerations, we can see whether the leading term of the lagrangian remains invariant under these global transformations. Before proceeding to the demonstration, we should bear in mind the properties of the trace, in particular $\langle AB\rangle = \langle BA\rangle$, and the unitarity of R and L.

$$\mathcal{L}^{(2)} = \frac{f^2}{4}\langle\partial_\mu U\partial^\mu U^\dagger\rangle \rightarrow \mathcal{L}'^{(2)} = \frac{f^2}{4}\langle R\partial_\mu UL^\dagger L\partial^\mu U^\dagger R^\dagger\rangle = \mathcal{L}^{(2)} \tag{1.30}$$

This is a good example to illustrate the way to proceed in order to ensure that this term satisfies the rest of the symmetries imposed by QCD. We are going to avoid involving ourselves in this matter, suffice to say that this piece of lagrangian preserves the other symmetries.

Regarding the physical meaning of $\mathcal{L}^{(2)}$, one can expand the exponential $U = 1 + i\phi/f + \ldots$, then $\partial_\mu U = i\partial_\mu\phi/f + \ldots$, and rewriting the lagrangian in these terms the

standard form of the kinetic term is recovered.

$$\mathcal{L}^{(2)} = \frac{f^2}{4}\langle i\partial_\mu\phi/f(-i\partial^\mu\phi/f)\rangle + \cdots = \frac{1}{4}\partial_\mu\phi_a\partial^\mu\phi_b\langle\lambda_a\lambda_b\rangle + \cdots = \frac{1}{2}\partial_\mu\phi_a\partial^\mu\phi_a + \ldots \quad (1.31)$$

To reach the shown result one makes use of the fact that $\langle\lambda_a\lambda_b\rangle = 2\delta_{ab}$ where the indexes a, b account for the eight massless particles. The dots represent the rest of the terms which consist of four or more Goldston fields. Furthermore, we now clearly see the purpose of the multiplicative $f^2/4$ constant.

It seems logical to consider any other possible arrangement, compatible with the symmetries of QCD, or combinations of fields which introduce two derivatives such as the product of two invariant traces $\langle\partial_\mu UU^\dagger\rangle$ or terms of the type $\langle\partial_\mu\partial^\mu UU^\dagger\rangle$. But all possibilities are excluded because they are either zero or they are proportional to eq. (1.27).

So far, we have seen that $\mathcal{L}^{(2)}$ is invariant under $SU(3)_L \times SU(3)_R$ transformations and, obviously then by Noether's theorem, we can associate one current to each accomplished symmetry. See [6] for a detailed calculation of the left and the right currents which read

$$\begin{aligned} J_L^{\mu,a} &= i\frac{f^2}{4}\langle\lambda_a\partial_\mu U^\dagger U\rangle \\ J_R^{\mu,a} &= -i\frac{f^2}{4}\langle\lambda_a U\partial_\mu U^\dagger\rangle. \end{aligned} \quad (1.32)$$

For convenience, as it was done in eq. (1.17), we can define the vector and the axial

current

$$\begin{aligned} V_a^\mu &= -i\frac{f^2}{4}\langle\lambda_a[U,\partial_\mu U^\dagger]\rangle \\ A_a^\mu &= -i\frac{f^2}{4}\langle\lambda_a\{U,\partial_\mu U^\dagger\}\rangle. \end{aligned} \tag{1.33}$$

Given the previous expressions, the axial current can be expanded in powers of ϕ ($A_a^\mu = -f\partial^\mu\phi_a + O(\phi^3)$) to calculate the matrix element between the vacuum and one-boson state (in the chiral limit).

$$\begin{aligned} \langle 0|A_a^\mu|\phi_b(p)\rangle &\approx \langle 0|-f\partial^\mu\phi_a(x)|\phi_b(p)\rangle = -f\partial^\mu exp(-ipx)\delta_{ab} \\ &= ip^\mu f exp(-ipx)\delta_{ab}. \end{aligned} \tag{1.34}$$

The connection of the vacuum with the pion via the axial current is indeed their decay process with decay constant f, in the chiral limit, which is measured by $\pi^+ \to l^+ + \nu_l$ decay process giving $f \approx f_\pi = 92.4$ MeV. This is the value we gave in advance when introducing the chiral fields in eq. (1.24).

Returning to the discussion of the lagrangian at order $O(p^2)$, we have neglected the contribution of any mass term assuming a perfect chiral symmetry. The inclusion of such a term, apart from introducing the explicit chiral symmetry breaking (see the discussion at the end of Sec. (1.1)), leads to the finite mass of the NG bosons. If we want to take into account this fact, we can focus on the mass term in the QCD lagrangian eq. (1.22). The only way to preserve the invariance under chiral transformations is to constrain the transformation of the constant M matrix according to

$$M \to M' = LMR^\dagger. \tag{1.35}$$

By analogy, for the effective chiral lagrangian, the most general mass contribution at this order ($\mathcal{L}_M^{(2)}(U,M)$) compatible with (1.25) and (1.35) transformations reads

$$\mathcal{L}_M^{(2)} = \frac{f^2 B_0}{2}\langle MU^\dagger + UM^\dagger\rangle, \tag{1.36}$$

from which, expanding once more in powers of ϕ and paying attention only to the second order in the fields, we recover the Gell-Mann-Oakes-Renner (GOR) relation. Considering the isospin-symmetric limit $m_u = m_d = m$, the GOR relations are explicitly given by

$$\begin{aligned} M_\pi^2 &= 2B_0 m \\ M_K^2 &= B_0(m + m_s) \\ M_\eta^2 &= \frac{2}{3}B_0(m + 2m_s), \end{aligned} \tag{1.37}$$

which properly combined with one another give the Gell-Mann-Oakes relation ($4M_K^2 = 3M_\eta^2 + M_\pi^2$). The most obvious effect of the presence of the real B_0 factor in the GOR relations is the impossibility of the direct determination of the quark masses from the pseudoscalar meson masses. Concerning this factor, see [6] for a detailed explanation, we can find a relation between this and the chiral quark condensate at lowest order via the expression

$$3f^2 B_0 = -\langle \bar{q}q\rangle. \tag{1.38}$$

Before continuing with the inclusion of higher order terms in the effective lagrangian, one can first consider the incorporation of external fields. As in the case of gauge theories, the way to couple them to the lagrangian is rather straightforward, the ordinary derivative has to be replaced by the covariant one. Being v_μ and a_μ, the external vector

and and the axial vector currents, the covariant derivative is given by

$$\partial_\mu U \to D_\mu U = \partial_\mu U - i\,[v_\mu, U] - i\{a_\mu, U\}. \tag{1.39}$$

In principle, since the effective lagrangian consist of an expansion in powers of momentum and mass terms, it could contain an infinite number of them. Nevertheless, one should wonder if the effort of including higher orders in the lagrangian is worth. Since we are performing an expansion where the higher orders introduce small corrections to the leading term, it seems logical to believe that they would be determining only for calculations which require a high precision level. Furthermore, we should never lose sight of the fact that we are developing a calculation in the quantum mechanics framework where the loop contributions are expected. These reasons are encouraging enough to go beyond the $O(p^2)$ order.

First of all we need to provide a mechanism through which the higher order contributions should be systematically added to the lagrangian by order of relevance. The corresponding Feynnman diagrams are built from terms which come from an even number of derivatives as well as from quark mass terms which are counted as $O(p^2)$ as it was justified by the GOR relations (1.37) in addition with the on-shell condition $p^2 = M^2$. Thus, one might extract information in order to stablish a hierarchy for the different contributions by analysing the behaviour of each diagram under a linear rescaling of the external momenta, $p_i \to tp_i$, and a quadratic one of the light quark masses, $m_q \to t^2 m_q$ (or equivalently $M^2 \to t^2 M^2$). That is to say, one studies the degree of homogeneity, known as chiral dimension, of the amplitude $M(p_i, m_q)$ tied to

the corresponding diagram,

$$M(tp_i, t^2 m_q) = t^D M(p_i, m_q),$$

with D being the chiral dimension , which was formulated for the first time by Weinberg [43], and is given by the expression

$$D = 2 + \sum_{n=1}^{\infty} 2(n-1)N_{2n} + 2N_L, \tag{1.40}$$

where N_{2n} is the number of vertices originating from the lagrangian $\mathcal{L}_{2n}$ whose n-index accounts for the $2n$ order of the expansion and N_L denotes the number of independent loops of the diagram under study. One should take the Weinberg's power counting scheme based on a rescaling study as an overall mathematical tool.

Another interesting aspect of the inclusion of higher order contributions is the increasing number of low energy constants related to each term. This issue might be illustrated by taking as example the case of chiral $SU(3)$, if we examine $\mathcal{L}^{(2)}$ one finds 2 constants, 10 constants for $\mathcal{L}^{(4)}$, 90 for $\mathcal{L}^{(6)}$, ... For completeness, $\mathcal{L}^{(4)}$ is displayed below [51]. In order to construct such a term, one should consider all those building blocks which are consistent with the symmetries cited throughout the text that contribute as

$O(p^4)$ order terms.

$$\begin{aligned}
\mathcal{L}^{(4)} &= L_1\langle D_\mu U^\dagger D^\mu U\rangle^2 + L_2\langle D_\mu U^\dagger D_\nu U\rangle\langle D^\mu U^\dagger D^\nu U\rangle \\
&+ L_3\langle D_\mu U^\dagger D^\mu U D_\nu U^\dagger D^\nu U\rangle + L_4\langle D_\mu U^\dagger D^\mu U\rangle\langle \chi^\dagger U + \chi U^\dagger\rangle \\
&+ L_5\langle D_\mu U^\dagger D^\mu U(\chi^\dagger U + \chi U^\dagger)\rangle + L_6\langle \chi^\dagger U + \chi U^\dagger\rangle^2 + L_7\langle \chi^\dagger U - \chi U^\dagger\rangle^2 \\
&+ L_8\langle \chi^\dagger U\chi^\dagger U + \chi U^\dagger\chi U^\dagger\rangle - iL_9\langle F_R^{\mu\nu} D_\mu U D_\nu U^\dagger + F_L^{\mu\nu} D_\mu U^\dagger D_\nu U\rangle \\
&+ L_{10}\langle U^\dagger F_R^{\mu\nu} U F_{L\mu\nu}\rangle, \qquad (1.41)
\end{aligned}$$

where $\chi = 2B_0(s + ip)$ collects (pseudo)scalar source terms, s contains the quark mass matrix ($s = M + \dots$); vector and axial currents are combined as $r_\mu = v_\mu + a_\mu$, $l_\mu = v_\mu - a_\mu$, from which the strength tensors are formed: $F_R^{\mu\nu} = \partial^\mu r^\nu - \partial^\nu r^\mu - [r^\mu, r^\nu]$, $F_L^{\mu\nu} = \partial^\mu l^\nu - \partial^\nu l^\mu - [l^\mu, l^\nu]$. From the expression, it can be noticed that the low energy constants L_{1-3} multiply structures containing four derivatives, $L_{4,5}$ go with two derivatives and one quark mass terms; the L_{6-8} are assigned to the quark masses squared and, finally, $L_{9,10}$ only contribute to observables with external vector and axial vector sources.

1.2.2 Chiral Perturbation Theory for Baryons

So far, for simplicity, only a pure mesonic effective field theory has been considered in order to exemplify, in the easiest possible way, how to construct a chiral lagrangian consistent with the symmetries of the strong interaction among the Goldstone bosons and with the external fields. Since our study is within the framework of the meson-baryon interaction phenomenology in the $S = -1$ sector, we need to extend ChPT to also describe the dynamics of baryons at low energies. In particular, we will focus on processes

which involve a meson-baryon pair in the initial and final states, meaning that the number of baryons is conserved and there is no baryon-antibaryon creation/annihilation. The most restrictive consideration with the processes which can be described by means of this theory is that the three-momenta of the baryons ought to remain small, being of the order of M_π. This new lagrangian is presented as an expansion arranged in powers of momentum, exactly as one proceeds for the pure mesonic case.

To address the incorporation of baryons, we should view them as matter fields coupled to mesons and to external sources. These matter fields require a representation with a transformation law under $SU(3)_L \times SU(3)_R$ such that leaves the new lagrangian invariant. As a matter of fact, the Goldstone boson fields and their transformation laws also should be conveniently redefined. Previously these fields were specified by the chiral field U, eq. (1.24), now it is convenient to introduce the field u instead. These two fields are directly related, being u the square root of U ($u^2 = U$). Thus, bearing in mind that U transforms as was shown in eq. (1.25), u does it in the following way

$$u \longmapsto \sqrt{LUR^\dagger} = LuK^\dagger(L,R,U) = K(L,R,U)uR^\dagger, \tag{1.42}$$

where $K(L,R,U)\ \epsilon\ SU(3)$ depends on L, R and U non trivially. Therefore this transformation is local since U is defined as an exponential of a matrix which collects continuous functions in a Minkowski space ($U = U(x)$). This is in contrast to what happens to U where its transformation under $SU(3)_L \times SU(3)_R$ is global. This local character of the transformation makes mandatory the introduction of a covariant derivative, $D^\mu = \partial^\mu + \Gamma^\mu$, which transforms in the same way as the baryon fields. Hence, firstly, we introduce the baryon field and then we can see its transformation law which is a shared feature with the covariant derivative. The $\frac{1}{2}^+$ baryon octet is collected in a

traceless 3×3 matrix B where each member of the octet is represented by a Dirac spinor field:

$$B = \begin{pmatrix} \frac{1}{\sqrt{2}}\Sigma^0 + \frac{1}{\sqrt{6}}\Lambda & \Sigma^+ & p \\ \Sigma^- & -\frac{1}{\sqrt{2}}\Sigma^0 + \frac{1}{\sqrt{6}}\Lambda & n \\ \Xi^- & \Xi^0 & -\frac{2}{\sqrt{6}}\Lambda \end{pmatrix}, \tag{1.43}$$

transforming under $SU(3)_L \times SU(3)_R$ as $B \longmapsto KBK^\dagger$. Hence, turning to the covariant derivative, D^μ acting on B, $D^\mu B = \partial^\mu B + [\Gamma^\mu, B]$, should transform as $D^\mu B \longmapsto KD^\mu B$. Indeed, this is a usual property that could not take place unless the chiral connection (Γ^μ) were defined as

$$\Gamma^\mu = \frac{1}{2}\left(u^\dagger(\partial^\mu - ir^\mu)u + u(\partial^\mu - il^\mu)u^\dagger\right) \tag{1.44}$$

which transforms as $\Gamma^\mu \longmapsto K\Gamma^\mu K^\dagger - (\partial^\mu K)K^\dagger$. A part from Γ^μ, there is another $O(p)$ building block, known as chiral vielbein which can be written as

$$u^\mu = i\left(u^\dagger(\partial^\mu - ir^\mu)u - u(\partial^\mu - il^\mu)u^\dagger\right) \tag{1.45}$$

and that, also, it fulfils the transformation law $u^\mu \longmapsto Ku^\mu K^\dagger$. As last ingredient, it remains to be seen how the (pseudo)scalar source term ($\chi = 2B_0(s+ip) = 2B_0M + \dots$) is rewritten. Finally, this quark mass term is expressed by

$$\chi_+ = u^\dagger \chi u^\dagger + u\chi^\dagger u, \tag{1.46}$$

with the expected transformation $\chi_+ \longmapsto K\chi_+K^\dagger$. Once the fundamental building blocks of the meson-baryon effective chiral lagrangian are available, one should study

the power counting of momenta of each piece or block in order to arrange them in the expansion by order of relevance. This could be summarized as:

$$\bar{B}, B : O(1), \qquad u_\mu, \Gamma_\mu, (i\gamma_\mu D^\mu - M_0)B : O(p), \qquad \chi_+ : O(p^2),$$

being M_0 the common baryon octet mass in the chiral limit. Now, we are able to proceed to introduce the most general effective lagrangian for meson-baryon system

$$\mathcal{L}_{eff}(B,U) = \sum_{n=1}^{\infty} \mathcal{L}_{\phi B}^{(n)} = \mathcal{L}_{\phi B}^{(1)} + \mathcal{L}_{\phi B}^{(2)} + \mathcal{L}_{\phi B}^{(3)} + \mathcal{L}_{\phi B}^{(4)} + \ldots, \tag{1.47}$$

from this expression one appreciates that this lagrangian comes not only in even powers of momenta, such as in meson ChPT, but also odd powers are possible due to Dirac structures. Each $\mathcal{L}_{\phi B}^{(n)}$ term consist of bilinears of the B field with the chiral order $O(p^n)$. At LO ($O(p)$), one finds

$$\mathcal{L}_{\phi B}^{(1)} = \langle \bar{B}(i\gamma_\mu D^\mu - M_0)B\rangle + \frac{1}{2}D\langle \bar{B}\gamma_\mu\gamma_5\{u^\mu, B\}\rangle + \frac{1}{2}F\langle \bar{B}\gamma_\mu\gamma_5[u^\mu, B]\rangle \ , \tag{1.48}$$

where the low energy constants D and F are the $SU(3)$ axial vector constants subject to the constraint $g_A = D + F = 1.26$.

The contributions which are considered to be relevant for the present study are the s-wave ones, at NLO, these are :

$$\begin{aligned}\mathcal{L}_{\phi B}^{(2)} &= b_D\langle \bar{B}\{\chi_+, B\}\rangle + b_F\langle \bar{B}[\chi_+, B]\rangle + b_0\langle \bar{B}B\rangle\langle \chi_+\rangle + d_1\langle \bar{B}\{u_\mu, [u^\mu, B]\}\rangle \\ &\quad + d_2\langle \bar{B}[u_\mu, [u^\mu, B]]\rangle + d_3\langle \bar{B}u_\mu\rangle\langle u^\mu B\rangle + d_4\langle \bar{B}B\rangle\langle u^\mu u_\mu\rangle \ .\end{aligned} \tag{1.49}$$

The parameters preceding each term are the corresponding low energy constants at

NLO, they are the main characters of this study. As it has been said, in general, these constants are not fixed by the symmetries of the underlying theory, but need to be determined from experiment. A clear example of this are the low energy constants present at LO (f, D, F) which are subject to rather strong constraints coming from the semileptonic pion and hyperon decays. Actually, the parameters accompanying the first three terms of the eq. (1.49), which are chiral symmetry breaking terms and linear in the quark masses, can be determined. Specifically, b_D and b_F can be extracted from the mass splitting in the baryon octet

$$\begin{aligned} M_\Sigma - M_\Lambda &= \frac{16}{3} b_D (m_K^2 - m_\pi^2) \\ M_\Xi - M_N &= 8 b_F (m_\pi^2 - m_K^2) \\ M_\Sigma - M_N &= 4(b_D - b_F)(m_K^2 - m_\pi^2). \end{aligned} \tag{1.50}$$

This overdefined system can be solved because is a compatible system, then performing the calculation for an isospin averaged baryon and meson masses one obtains $b_D = 0.066\ \text{GeV}^{-1}$ and $b_F = -0.213\ \text{GeV}^{-1}$. The b_0-term shifts the whole baryon octet by the same amount, hence further information is needed to fix the b_0 parameter. This could well be the pion-nucleon sigma term, which empirical value is $\sigma_{\pi N} = 45 \pm 8$ MeV [52],

$$\sigma_{\pi N} = \langle N | \frac{m_u + m_d}{2} (\bar{u}u + \bar{d}d) | N \rangle = -2 m_\pi^2 (2 b_0 + b_D + b_F). \tag{1.51}$$

Another source of information in order to constraint b_0 is the strangeness content of the proton. In principle, the simplest quark model pictures of the nucleon would suggest that it has no strange quark content. Therefore the expectation value of the scalar density $\bar{s}s$ in the proton would be zero. But this is not the case in $SU(3)$ chiral

dynamics. Taking suitable combinations of the b_0, b_D and b_F one gets

$$y = \frac{2\langle p|\bar{s}s|p\rangle}{\langle p|\bar{u}u + \bar{d}d|p\rangle} = \frac{2(b_0 + b_D - b_F)}{2b_0 + b_D + b_F}, \tag{1.52}$$

whose empirical value is taken from [52] ($y = 0.2 \pm 0.2$). If one remains at linear order in the quark masses and tries to satisfy these two pieces of information (y and $\sigma_{\pi N}$), then one realizes that there is not a unique value of b_0 capable of achieving this simultaneously. Instead of a unique value, a region of validity can be established for b_0 ranging between $[-0.52, -0.28]$ GeV^{-1} where the bounds are set by the experimental values of y and $\sigma_{\pi N}$. But the b_i coefficients are not the only ones which appear in eq. (1.49). The rest of the low energy constants, namely $d_i, i = 1-4$, can be constrained using data coming from the meson-baryon octet such as the isospin even πN s-wave scattering length and the isospin zero kaon-nucleon s-wave scattering length which experimental values are $a^+_{\pi N} = (-0.012 \pm 0.06) fm$ [53] and $a^0_{KN} = (-0.1 \pm 0.1) fm$ [54] respectively. The reader can find more details on this issue in [55] and the references therein.

It is important to mention that if one considers further corrections in the lagrangian, new contributions should be absorbed by the NLO coefficients making these constraints on them barely applicable. We will return to this issue later on.

1.2.3 Low energy meson-baryon interaction up to NLO

At this point, at low energy, the s-wave meson-baryon interaction kernel up to the order $O(p^2)$ in momentum space can be derived from eqs.(1.48) and (1.49). The elements of the interaction matrix, here written as $\hat{V}_{ij} = \langle i|\hat{V}|j\rangle$, couple several meson-baryon

channels arranged in sectors with given quantum numbers among those included within the wider $SU(3)$ flavour sector. The indices (i, j) cover all the initial and final channels, which, in the case of strangeness $S = -1$ and charge $Q = 0$ explored here, amount to ten: K^-p, $\bar{K}^0n$, $\pi^0\Lambda$, $\pi^0\Sigma^0$, $\pi^-\Sigma^+$, $\pi^+\Sigma^-$, $\eta\Lambda$, $\eta\Sigma^0$, $K^+\Xi^-$ and $K^0\Xi^0$. The interaction $\hat{V}_{ij}$ depends on the total energy of the meson-baryon system in the center-of-mass frame $\sqrt{s}$, on the solid angle of the scattering Ω, and on the $\sigma_{i,j}$ spin degrees of freedom of the baryons in channels (i, j). Since the interaction with which we are dealing consist of the scattering of a NG boson with a spin $\frac{1}{2}$ baryon target, the projection of $\hat{V}_{ij}(\sqrt{s}, \Omega, \sigma_i, \sigma_j)$ onto s-wave gives a contribution which depends only on $\sqrt{s}$:

$$V_{ij}(\sqrt{s}) = \frac{1}{8\pi} \sum_{\sigma} \int d\Omega \; \hat{V}_{ij}(\sqrt{s}, \Omega, \sigma_i, \sigma_j). \tag{1.53}$$

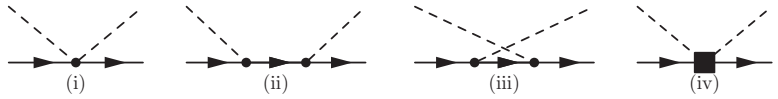

Figure 1.2: Feynman diagrams for the meson-baryon interaction: Weinberg-Tomozawa term (i), direct and crossed Born terms (ii) and (iii), and NLO terms (iv). Dashed (solid) lines represent the pseudoscalar octet mesons (octet baryons).

The relevant contributions to the interaction kernel are diagrammatically represented in Fig. 1.2. The first three contributions appearing in the figure, namely (i), (ii) and (iii), are calculated using the Lagrangian at lowest order, while the NLO contribution to the meson-baryon scattering are shown by diagram (iv).

The so-called Weinberg-Tomozawa (WT) contribution corresponds to the contact diagram (i) in Fig. 1.2; this comes from the term with the covariant derivative $[D_\mu, B]$

in eq. (1.48):

$$\mathcal{L}_{\phi B}^{WT} = i\langle \bar{B}\gamma_\mu [D^\mu, B]\rangle,$$

where the symbol $\langle \dots \rangle$ stands for the trace in flavour space.

To contextualize the reader and to avoid a constant look back to past expressions, we recall the main expressions to develop the necessary calculations in order to obtain the interaction kernels. First, we defined the covariant derivative as

$$[D_\mu, B] = \partial_\mu B + [\Gamma_\mu, B] \ ,$$

where the chiral connection Γ_μ is given by (alternatively to eq. (1.44))

$$\Gamma_\mu = \tfrac{1}{2}[u^\dagger, \partial_\mu u].$$

Here one should remember that u is related to the chiral meson field by

$$U(\phi) = u^2(\phi) = \exp\left(\sqrt{2}i\frac{\phi}{f}\right), \tag{1.54}$$

with ϕ defined in eq. (1.23). The quantity U enters the Lagrangian in the combinations $u_\mu = iu^\dagger \partial_\mu U u^\dagger$. In addition, the octet baryon fields are collected in the 3×3 matrix (1.43) where each entry corresponds to a Dirac spinor field.

Once all inputs are well define, we can expand u in terms of ϕ getting

$$u = 1 + \frac{i\phi}{\sqrt{2}f} - \frac{\phi^2}{4f^2} + \dots; \tag{1.55}$$

this way we can stablish the structure of the chiral connection as

$$\Gamma_\mu \approx \frac{1}{4f^2}\left(\phi\partial_\mu\phi - \partial_\mu\phi\phi\right) \tag{1.56}$$

and, consequently, this WT piece of the meson-baryon lagrangian reads

$$\mathcal{L}_{\phi B}^{WT} = \langle \bar{B} i\gamma^\mu \frac{1}{4f^2}\left[(\phi\partial_\mu\phi - \partial_\mu\phi\phi)B - B(\phi\partial_\mu\phi - \partial_\mu\phi\phi)\right]\rangle. \tag{1.57}$$

At this point, only the meson and baryon fields needs to be included; but one should be careful when introducing the degrees of freedom, whether the mesonic or the barionic ones. In the particular case of the barionic degrees of freedom for a given process, the incoming ones should be incorporated in B, while the outgoing baryons should be collected by $\bar{B}$ ($\bar{B} = B^\dagger\gamma^0$). The way to proceed for mesons is trickier, the initial mesons as well as the resulting ones after the interaction should be taken into account in ϕ. To this end, the outgoing degrees of freedom are introduced in the ϕ matrix as antiparticles in the initial state thanks to the equivalence between the destruction of a particle and the creation of its antiparticle. Furthermore, there is no special difficulty in calculating $\partial_\mu\phi$; since this derivative becomes the derivative of the mesonic degrees of freedom present in the initial and final state which are expressed as free-particle plane waves ($\sim e^{-q^\mu x_\mu}$ or $\sim e^{q'^\mu x_\mu}$) respectively. The change of sign in the exponential is due to the fact that the antiparticle moves in the temporal opposite sense. Hence, given the nature of particle/antiparticle of the degrees of freedom present in ϕ depending on the role played in the process, one should pay attention to the sign accompanying the corresponding component of the four-momentum after the corresponding derivative ∂_μ.

Finally, from the Lagrangian $\mathcal{L}_{\phi B}^{WT}$, and keeping in mind the previous remarks, one

can derive the meson-baryon interation kernel at lowest order corresponding to the Weinberg-Tomozawa (WT) term, which reads:

$$V_{ij}^{WT} = -C_{ij}\frac{1}{4f^2}\bar{u}_{B_j}^{s'}(p_j)\gamma^{\mu}u_{B_i}^{s}(p_i)(q_{i\mu}+q_{j\mu}) \ , \tag{1.58}$$

and depends only on one parameter, the pion decay constant f. The indices (i,j) cover all the initial and final channels of the explored sector. The matrix of coefficients C_{ij} are displayed in Table 4.1, Appendix A. The four-momenta $q_{i\mu}$ and $q_{j\mu}$ are those of the incoming and outgoing mesons, respectively, while $u_{B_i}^{s}(p_i)$ denotes the incoming baryon spinor with spin s and momentum p_i, and analogously for the spinor $\bar{u}_{B_j}^{s'}(p_j)$ of the outgoing baryon. And at the end of the day, applying the s-wave projection (1.53), it reads:

$$V_{ij}^{WT} = -C_{ij}\frac{1}{4f^2}\mathcal{N}_i\mathcal{N}_j\left(\sqrt{s}-M_i-M_j\right), \tag{1.59}$$

The normalization factor $\mathcal{N}$ is defined as $\mathcal{N} = \sqrt{(M+E)/(2M)}$, with M and E being, respectively, the mass and energy of the baryon whose sub-indexes denote their incoming and outgoing character. Here $\sqrt{s}$ is the total energy of the meson-baryon system in the center-of-mass frame.

We next consider the contributions of the Born diagrams whose vertices are calculated from lagrangian (1.48), specially, from the pieces:

$$\mathcal{L}_{\phi B}^{Born} = \frac{1}{2}D\langle\bar{B}\gamma_{\mu}\gamma_5\{u^{\mu},B\}\rangle + \frac{1}{2}F\langle\bar{B}\gamma_{\mu}\gamma_5[u^{\mu},B]\rangle \ .$$

Developing each element in the former expression, in a similar fashion as before, one

gets:

$$\begin{aligned} u_\mu &= iu^\dagger \partial_\mu U u^\dagger = i(1 - \frac{i\phi}{\sqrt{2}f} - \frac{\phi^2}{4f^2} + \dots)\partial_\mu(1 + \frac{i\sqrt{2}\phi}{f} - \frac{\phi^2}{f^2} + \dots)(1 - \frac{i\phi}{\sqrt{2}f} - \frac{\phi^2}{4f^2} + \dots) \\ &\approx -\frac{\sqrt{2}}{f}\partial_\mu \phi, \end{aligned}$$

hence, the commutator and anticommutator can be written as

$$\begin{aligned} \{u_\mu, B\} &= -\frac{\sqrt{2}}{f}(\partial_\mu \phi B + B\partial_\mu \phi) \\ [u_\mu, B] &= -\frac{\sqrt{2}}{f}(\partial_\mu \phi B - B\partial_\mu \phi) \end{aligned}$$

to finally express the corresponding terms of the lagrangian in the following way

$$\mathcal{L}_{\phi B}^{Born} = \frac{1}{\sqrt{2}f}\left(D\langle \bar{B}\gamma_5\gamma^\mu(\partial_\mu\phi B + B\partial_\mu\phi)\rangle + F\langle \bar{B}\gamma_5\gamma^\mu(\partial_\mu\phi B - B\partial_\mu\phi)\rangle\right).$$

Now only, following the Feynman rules, the diagrams should be built in order to get the interaction kernel; since the vertices can be obtain just by performing the calculation including degrees of freedom involved in the process we want to study in the meson- and baryon-fields. The interaction kernel corresponding to the direct Born diagram, which corresponds to diagram (ii) in Fig. 1.2, reads

$$V_{ij}^D = C_{\bar{i}i,k}^{(\mathrm{Born})} C_{\bar{j}j,k}^{(\mathrm{Born})} \bar{u}_{B_j}^{s'}(p_j)\gamma_5\gamma^\nu q_{j\nu} \frac{\gamma^\alpha p_{k\alpha} + m_k}{p_k^2 - m_k^2}\gamma_5\gamma^\mu q_{i\mu} u_{B_i}^s(p_i) \tag{1.60}$$

where the k label refers to the intermediate baryon involved in the process whose four-momentum $p_{k\alpha} = (p_{k0}, \vec{0})$ in the center-of-mass frame corresponds to an on shell baryon satisfying the conservation relation $p_k^2 = (p_i + q_i)^2 = s$. The couplings between different

baryon-meson channels to the intermediate baryon are the coefficients $C^{(\mathrm{Born})}_{\bar{i}i,k}$ which are compiled in Appendix A, relations A.1, and which depend on the axial vector constants. After applying the s-wave projection in the way given by eq. (1.53), we obtain

$$V^D_{ij} = -\sum_{k=1}^{8} \frac{C^{(\mathrm{Born})}_{\bar{i}i,k} C^{(\mathrm{Born})}_{\bar{j}j,k}}{12f^2} \mathcal{N}_i \mathcal{N}_j \frac{(\sqrt{s}-M_i)(\sqrt{s}-M_k)(\sqrt{s}-M_j)}{s-M_k^2} \quad , \tag{1.61}$$

the sum over k extends to all possible baryons of the octet. However, in this particular sector ($S=-1, Q=0$) and for this process, only Λ and Σ^0 can act as intermediate baryons compatible with these quantum numbers.

The crossed Born diagram can be formally expressed as in eq. (1.60). But, from diagram (iii) in Fig. 1.2, one realizes that the four-momentum conservation now implies the conservation relation: $p_k^2 = (p_i - q_j)^2 = (p_j - q_i)^2 = u$. Here u is the corresponding Mandelstam variable. Then, once projecting onto s-wave, this diagram gives rise to interaction kernel:

$$\begin{aligned} V^C_{ij} = & \sum_{k=1}^{8} \frac{C^{(\mathrm{Born})}_{\bar{j}k,i} C^{(\mathrm{Born})}_{\bar{i}k,j}}{12f^2} \mathcal{N}_i \mathcal{N}_j \\ & \times \Bigg[\sqrt{s} + M_k - \frac{(M_i+M_k)(M_j+M_k)}{2\,(M_i+E_i)\,(M_j+E_j)} (\sqrt{s} - M_k + M_i + M_j) \\ & + \frac{(M_i+M_k)(M_j+M_k)}{4q_iq_j} \Big\{ \sqrt{s} + M_k - M_i - M_j \\ & - \frac{s + M_k^2 - m_i^2 - m_j^2 - 2E_iE_j}{2\,(M_i+E_i)\,(M_j+E_j)} (\sqrt{s} - M_k + M_i + M_j) \Big\} \\ & \times \ln \frac{s + M_k^2 - m_i^2 - m_j^2 - 2E_iE_j - 2q_iq_j}{s + M_k^2 - m_i^2 - m_j^2 - 2E_iE_j + 2q_iq_j} \Bigg] \quad , \end{aligned} \tag{1.62}$$

where, just to recall the reader, $\vec{q}_i$ and $\vec{q}_j$ are the center-of-mass (CM) three-momenta

in the corresponding i, j channels, and m_i, m_j denote the corresponding meson masses.

Finally, from the lagrangian $\mathcal{L}^{(2)}_{\phi B}$, one can derive the meson-baryon interaction kernel at NLO. If we focus on this lagrangian we can appreciate seven terms, these pieces are the structures from which we depart in order to exemplify how the final expression can be obtained.

First, it would be preferable to introduce χ_+ which is the term responsible of explicit breaking of chiral symmetry:

$$\chi_+ = -\frac{1}{4f^2}\left\{\phi,\{\phi,\chi\}\right\}, \quad \chi = \begin{pmatrix} m_\pi^2 & 0 & 0 \\ 0 & m_\pi^2 & 0 \\ 0 & 0 & m_K^2 - m_\pi^2 \end{pmatrix}. \tag{1.63}$$

The seven main constituents of the lagrangian are displayed as follows:

- $b_D\langle\bar{B}\{\chi_+, B\}\rangle$ term:

$$\begin{aligned} \chi_+ &= -\frac{1}{4f^2}\left(\phi^2\chi + 2\phi\chi\phi + \chi\phi^2\right) \\ b_D\langle\bar{B}\{\chi_+, B\}\rangle &= -\frac{b_D}{4f^2}\langle\bar{B}\left(\phi^2\chi + 2\phi\chi\phi + \chi\phi^2\right)B + \bar{B}B\left(\phi^2\chi + 2\phi\chi\phi + \chi\phi^2\right)\rangle. \end{aligned}$$

- $b_F\langle\bar{B}[\chi_+, B]\rangle$ term:

$$b_F\langle\bar{B}[\chi_+, B]\rangle = -\frac{b_F}{4f^2}\langle\bar{B}\left(\phi^2\chi + 2\phi\chi\phi + \chi\phi^2\right)B - \bar{B}B\left(\phi^2\chi + 2\phi\chi\phi + \chi\phi^2\right)\rangle.$$

- $b_0\langle\bar{B}B\rangle\langle\chi_+\rangle$ term:

$$b_0\langle\bar{B}B\rangle\langle\chi_+\rangle = -\frac{b_0}{4f^2}\langle\bar{B}B\rangle\langle\phi^2\chi + 2\phi\chi\phi + \chi\phi^2\rangle.$$

- $d_1\langle\bar{B}\{u_\mu,[u^\mu,B]\}\rangle$ term:

$$d_1\langle\bar{B}\{u_\mu,[u^\mu,B]\}\rangle = \frac{2d_1}{f^2}\langle\bar{B}\left(\partial_\mu\phi\partial^\mu\phi B - \partial_\mu\phi B\partial^\mu\phi + \partial^\mu\phi B\partial_\mu\phi - B\partial^\mu\phi\partial_\mu\phi\right)\rangle.$$

- $d_2\langle\bar{B}[u_\mu,[u^\mu,B]]\rangle$ term:

$$d_2\langle\bar{B}[u_\mu,[u^\mu,B]]\rangle = \frac{2d_2}{f^2}\langle\bar{B}\left(\partial_\mu\phi\partial^\mu\phi B - \partial_\mu\phi B\partial^\mu\phi - \partial^\mu\phi B\partial_\mu\phi + B\partial^\mu\phi\partial_\mu\phi\right)\rangle.$$

- $d_3\langle\bar{B}u_\mu\rangle\langle u^\mu B\rangle$ term:

$$d_3\langle\bar{B}u_\mu\rangle\langle u^\mu B\rangle = \frac{2d_3}{f^2}\langle\bar{B}\partial_\mu\phi\rangle\langle\partial^\mu\phi B\rangle.$$

- $d_4\langle\bar{B}B\rangle\langle u^\mu u_\mu\rangle$ term:

$$d_4\langle\bar{B}B\rangle\langle u^\mu u_\mu\rangle = \frac{2d_3}{f^2}\langle\bar{B}B\rangle\langle\partial^\mu\phi\partial_\mu\phi\rangle.$$

Now all the ingredients needed to get the corresponding interaction kernel are available, one should proceed with the introduction of the fields and the development of some algebra. The resulting expression for the potential can be written as:

$$V_{ij}^{NLO} = \frac{1}{f^2}\bar{u}^{s'}_{B_j}(p_j)\left(D_{ij} - 2(q_{i\mu}q^{j\mu})L_{ij}\right)u^s_{B_i}(p_i), \tag{1.64}$$

which after employing eq. (1.53), in order to exclude other contributions than s-wave, becomes:

$$V_{ij}^{NLO} = \frac{1}{f^2}\mathcal{N}_i\mathcal{N}_j\left[D_{ij} - 2\left(\omega_i\omega_j + \frac{q_i^2 q_j^2}{3\left(M_i + E_i\right)\left(M_j + E_j\right)}\right)L_{ij}\right], \tag{1.65}$$

where ω_i, ω_j are the meson energies involved in the transition amplitude. The D_{ij} and L_{ij} coefficients depend on the NLO parameters b_0, b_D, b_F, d_1, d_2, d_3 and d_4 and are given in Table 4.2, Appendix A .

To conclude, the total interaction kernel up to NLO is expressed as the sum:

$$V_{ij} = V_{ij}^{WT} + V_{ij}^{D} + V_{ij}^{C} + V_{ij}^{NLO} \tag{1.66}$$

1.3 Unitary extension of ChPT: the Bethe-Salpeter equation

The probability conservation during the time evolution of a system leads to the fact that physical scattering amplitude should satisfy the unitarity condition of the S-matrix. A nonperturbative calculation of the amplitude can ruin the unitarity condition. We can find such a case in ChPT where the amplitude is expanded in energy powers of the NG bosons. Since the amplitude monotonically increases as one goes to higher energies, the unitarity bond can be violated at a certain kinematical scale. This does not present a problem for the behaviour of the amplitude if one remains at low energy. But this way of proceeding can not be maintained, even at low energies, when the interaction between hadrons is strong enough to produce a resonance that can be interpreted as

a bound state below the thresholds of the hadrons involved. Such a situation makes a perturbative calculation of the amplitude not applicable in the vicinity of resonances. Instead, we need to construct the scattering amplitude in a nonperturbative fashion. In this work, we solve the Bethe-Salpetter (BS) equations in coupled-channels. Other techniques can also be applied such as the N/D Method [9, 56]. As a comment, we should make it clear that both methods reach the same final expression for the scattering amplitude. The philosophy behind the unitarization method employed here consists of solving the BS equations for the scattering amplitudes T_{ij} once we get a well-defined potential, i.e. eq. (1.66), as is schematically displayed in Fig. 1.3, which corresponds to the infinite sum

$$T_{ij} = V_{ij} + V_{il}G_lV_{lj} + V_{il}G_lV_{lk}G_kV_{kj} + ... \ , \tag{1.67}$$

where the subscripts $i, j, l, \ldots$ run over all possible channels and the loop function G_i stands for the propagator of the meson-baryon state of channel i. The former equation can also be cast as:

$$T_{ij} = V_{ij} + V_{il}G_lT_{lj} \ . \tag{1.68}$$

In spite of the simplicity of eq. (1.68), obtaining the amplitude T_{ij} is not so straight-

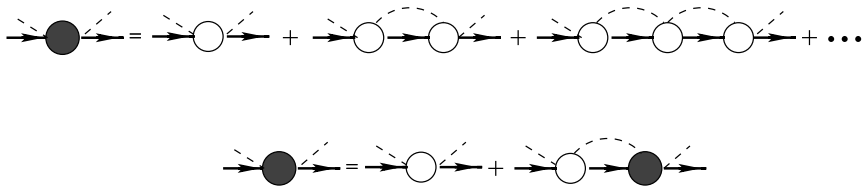

Figure 1.3: Diagrammatic solution of the Bethe-Salpeter equation, where the interaction kernel V is represented by the empty blobs, the scattering matrix T - by the solid blobs, and the loop function G is represented by the intermediate baryon-meson propagators.

forward, because the former is an integral equation which involves an integral over the four-momentum of the intermediate meson-baryon system. Fortunately, it has been shown [20] that the interaction kernel can be conveniently splitted into its on-shell contribution and the corresponding off-shell one. The off-shell part of the interaction kernel gives rise to a tadpole-type diagram, which can be reabsorbed into renormalization of couplings and masses and could, hence, be omitted from the calculation. This procedure permits factorizing V_{il} and T_{lj} out of the integral equation, leaving a simple system of algebraic equations to be solved, which, in matrix form reads:

$$T = (1 - VG)^{-1}V, \tag{1.69}$$

where the loop function G stands for a diagonal matrix with elements:

$$G_l = \mathrm{i}\int \frac{d^4q_l}{(2\pi)^4}\frac{2M_l}{(P-q_l)^2 - M_l^2 + \mathrm{i}\epsilon}\frac{1}{q_l^2 - m_l^2 + \mathrm{i}\epsilon}\ , \tag{1.70}$$

where M_l and m_l are the baryon and meson masses of the "l" channel. The loop function diverges logarithmically and needs to be regularized. We apply dimensional regularization, which gives:

$$\begin{aligned} G_l = \ & \frac{2M_l}{(4\pi)^2}\left\{ a_l(\mu) + \ln\frac{M_l^2}{\mu^2} + \frac{m_l^2 - M_l^2 + s}{2s}\ln\frac{m_l^2}{M_l^2} + \right. \\ & \left. \frac{q_{\mathrm{cm}}}{\sqrt{s}}\ln\left[\frac{(s + 2\sqrt{s}q_{\mathrm{cm}})^2 - (M_l^2 - m_l^2)^2}{(s - 2\sqrt{s}q_{\mathrm{cm}})^2 - (M_l^2 - m_l^2)^2}\right]\right\}. \end{aligned} \tag{1.71}$$

The loop functions G_l depend, for a given dimensional regularization scale μ which is taken to be 1 GeV in our particular case, on the subtraction constants a_l. These are unknown parameters that will be fitted to the experimental data. However, isospin

symmetry arguments are commonly used to reduce the number of independent subtraction constants. The lack of knowledge about the values of the a_l constants does not rule out the possibility of establishing a natural size to these parameters. Indeed, as discussed in [9], a direct comparison between the dimensional regularization method and an approximation to calculate the loop function using a cut off, which was carried out in [8], allow us to establish the following relation:

$$a_l(\mu) = \frac{1}{16\pi^2}\Big[1 - 2\ln\left(1 + \sqrt{1 + \frac{\bar{M}_l^2}{\mu^2}}\right) + \dots\Big], \tag{1.72}$$

where $\bar{M}_l$ is the average mass of the octet of $J^P = \frac{1}{2}^+$ ($\bar{M}_l = 1.15$ GeV), and the ellipses indicates higher order terms in the non-relativistic expansion and also take into account powers of m_l/M_l. Since in our work we take $\mu = 1$ GeV, one should expect values for the subtraction constants around $a_l(\mu = 1\ GeV) \approx -5.38 \cdot 10^{-3}$. But we have to emphasize that the authors of [9] used a different remapping for the subtraction constants. In fact, our definition of a_l constants was chosen to compare with the most recent papers on this topic. In order to recover the original expression for eq. (1.72) in [9], and for a later comparison of the obtained values once the model is fitted to the experimental data, we need the relation between our subtraction constants and the ones from [9]

$$a_l^{OM}(\mu) = 16\pi^2 a_l(\mu) - 1, \tag{1.73}$$

where the OM superscript identifies the set of subtraction constants related to [9]. Then only by introducing the value obtain by means of eq. (1.72) as $a_l(\mu)$ in eq. (1.73), one gets $a_l^{OM}(\mu) = -1.85$ as the natural size with which we can compare our values.

In the presence of the Born terms the above on-shell scheme should be treated

with care since these may lead to conceptual and/or practical difficulties, as described in Ref. [57]. In particular, the u-channel Born graph, Fig. 1(iii), introduces non-physical sub-threshold cuts, generated by the propagator of the intermediate baryon. In principle, it is possible that the subthreshold cuts of some heavy meson-baryon pairs can contribute to physical processes of light meson-baryon channels. This is an artefact of the on-shell scheme and a simple way to deal with it, consisting in matching the u-channel Born term to a constant value below a certain invariant energy, was proposed in Ref. [15]. Fortunately, these non-physical cuts are not encountered in the kinematical regions explored in the present work.

Chapter 2

Meson-Baryon interaction in the $S = -1$ sector

In the previous chapter Unitaritzed Chiral Perturbation Theory (UChPT), which combines chiral dynamics with unitarization techniques in coupled channels, has been introduced as a proper framework to treat the low-energy meson-baryon interaction. This scheme is based on two guiding principles: the inherited symmetries from QCD, particularly the (spontaneously broken) chiral symmetry, and general properties of the scattering amplitude such as unitarity and analiticity. The descriptive power of this tool has been shown not only in reproducing the scattering data but also in generating bound-states and resonances dynamically (see [58] and references therein). Besides the previous advantages, UChPT permits extending the validity of ChPT to higher energies.

A clear example of the success of UChPT is the description of the $\Lambda(1405)$ resonance, located only 27 MeV below the $\bar{K}N$ threshold, that emerges from coupled-channel

meson-baryon re-scattering in the $S = -1$ sector. In [59], the dynamical generation of $\Lambda(1405)$ was formulated, for the first time, in terms of the unitarized chiral meson-baryon interaction in coupled channels almost 40 years after its dynamical origin was pointed out [60]. A lot of activity was awaken by this success in the community, which analysed the effects of including a complete basis of meson-baryon channels, differences in the regularization of the equations, s- and u-channel Born terms in the Lagrangian, next-to-leading (NLO) contributions, etc ... [7–12, 14, 15, 17, 61]. The various developed models could reproduce the $\bar{K}N$ scattering data very satisfactorily and all these efforts culminated in establishing the $\Lambda(1405)$ as a superposition of two poles of the scattering amplitude, generated dynamically from the unitarized meson-baryon interaction in coupled channels [9, 13, 16].

This topic has experienced a renewed interest in the last few years, after the availability of a more precise measurement of the energy shift and width of the $1s$ state in kaonic hydrogen by the SIDDHARTA collaboration [18] at DAΦNE. The CLAS collaboration at JLAB has also recently provided mass distributions of $\Sigma^+\pi^-$, $\Sigma^-\pi^+$, and $\Sigma^0\pi^0$ states in the region of the $\Lambda(1405)$ [62], as well as differential cross sections [63] and a direct determination of the expected spin-parity $J^\pi = 1/2^-$ of the $\Lambda(1405)$ [64]. Invariant $\pi\Sigma$ mass distributions from pp scattering experiments have recently been measured by the COSY collaboration at Jülich [65] and by the HADES collaboration at GSI [66]. In parallel with the increased experimental activity, the theoretical models have been revisited [19–23] and analyses of the new reactions, aiming at better pinning down the properties of the $\Lambda(1405)$, have been performed [24–26]. Aiming for testing models based on UChPT trying to reproduce all these new data, several studies of the meson-baryon interaction in s-wave approximation were performed [19, 21–23] . Once again, UChPT showed to be an appropriate tool to describe this sector.

From [8–15, 17, 19, 22, 23], it can be concluded that the significant term that allows one to get a good agreement with the experimental data is the Weinberg-Tomozawa (WT) one, which is of order $O(p)$, and the addition of other terms such as the direct and crossed Born terms ($O(p)$) as well as the NLO terms ($O(p^2)$) only play a fine-tuning role. At this point, it is important to highlight that the fits carried out to develop these models were accommodated to the two-body cross sections of K^-p scattering into $\pi\Sigma, \bar{K}N, \pi\Lambda$ states, from now on we will refer to them as the classical channels. This was not the case for [21], whose authors performed a fit which included, apart from the classical channels, scattering data from $K^-p \to \eta\Lambda, \pi^0\pi^0\Sigma^0$ and data from two event distribution ($K^-p \to \Sigma^+(1660)\pi^- \to \Sigma^+\pi^-\pi^+\pi^-$ and $K^-p \to \pi^0\pi^0\Sigma^0$). The difference lies on the fact that they obtained a notably improvement of the accuracy when including the NLO contribution.

In this context, given the potential of UChPT, the $S = -1$ sector offers us a good chance to extract information about those parameters which are not well constrained and are present in the model from the expansion of ChPT. Fortunately, all the works we have cited devoted to this topic did not explore beyond the NLO and their authors did not take any other contribution than the s-wave one. Consequently, the number of low-energy constants could amount to a maximum of sixteen: the meson decay constant f, the axial vector couplings D and F, the NLO coefficients $b_0, b_D, b_F, d_1, d_2, d_3, d_4$ and six subtraction constants $a_{\pi\Sigma}, a_{\bar{K}N}, a_{\pi\Lambda}, a_{\eta\Sigma}, a_{\eta\Lambda}, a_{K\Xi}$ (or one cut off instead). In summary, in reference to the low-energy constants in UχPT calculations, we can remark that the f parameter is usually taken to be larger than the experimental value, ranging from $f = 1.15 f_\pi$ to $f = 1.36 f_\pi$, meaning to be a sort of average over the decay constants of the mesons involved in the various coupled channels. Actually, some of the previous authors assigned fixed values to this parameter depending on the meson involved in

the incoming and outgoing channels ($f_\pi = 92.4$ MeV [67], $f_K = 110.0$ MeV [67], $f_\eta = 120.1$ MeV estimated from the result in [68]) for each given meson-baryon process in the $S = -1$ sector. Moreover, the axial vector couplings were normally taken as fixed values ($D = 0.8., F = 0.46$), hence fulfilling the constraint $g_A = F + D = 1.26$. For the rest of the parameters, namely the NLO coefficients, the situation is more diverse. Most of the performed fits have endorsed the fact that the constraint over these parameters (see eqs. (1.50), (1.51) and (1.52) in Sect. 1.2.2) should be relaxed, since their studies went beyond tree level and incorporated higher order terms via the coupled-channel scattering equations. There were exceptions, as for instance in Refs. [7, 21, 61], where the authors did take into account the mentioned constraints on the NLO coefficients while carrying out the fits.

The dissimilarity in the values of the NLO coefficients found by different studies is the seed from which the present study arises. In the next section we disclose how the inclusion of additional processes, specially those which are very sensitive to the NLO contribution, can provide crucial information in order to get more reliable values for these parameters. A clear example of these kind of processes are the $K^- p \to K\Xi$ reactions. Before entering into the subject, it is convenient to point out that the validity of the theoretical framework when going to an energy range above the $K\Xi$ threshold is supported by UChPT. Let me recall the reader that one of the effects of the unitarization is to widen the range of applicability of ChPT, as we have mentioned in the first paragraph of this chapter. In addition, the available kinetic energy is not too large when exploring a region close to the $K\Xi$ threshold.

2.1 The crucial role of the $K^-p \to K\Xi$ reactions

The reproduction of the $K^-p \to K\Xi$ cross section has not been traditionally studied employing models derived from chiral lagrangians. But there is a feature, related to the resulting structure of the WT kernel (see eq. (1.59)), that made us turn our attention to these reactions. In particular, we observe that the Clebsch-Gordan-type coefficients for $K\Xi$ production from K^-p scattering in the WT interaction kernel are $C_{K^-p\to K^+\Xi^-} = C_{K^-p\to K^0\Xi^0} = 0$ (see Table 4.1 in Appendix A), meaning that there is no direct contribution of this term to the scattering amplitude for these reactions. Further, the strength coming from the rescattering terms due to the coupled channels is not sufficient to reproduce properly the experimental scattering data as we will show latter. This fact led us to believe that these reactions could be very sensitive to the next corrections in the hierarchy, this is to say, the direct and cross Born terms and the NLO term. Hence, a new study that includes such an experimental data set would provide more reliable values of low-energy constants. Before proceeding with the calculations and the fitting procedure, we should take into account some considerations.

The Born terms contribute mainly to p-wave, but their s-wave contribution begins to take relevance as the energy increases. Evidence of this can be found in the leading order calculation performed in [9] where the authors pointed out that the contribution of the s and u Born diagrams are almost negligible at energies around 1.3 GeV while their magnitude increases with energy reaching $\approx 20\%$ of the dominant WT contribution at 1.5 GeV. Despite the previous analysis, one finds that the contribution of the cross and direct Born terms is very moderate for studies which were based on lagrangians extended to NLO [15, 23]. In these articles, among other approaches, the authors present two models based on chiral Lagrangians which contain WT and NLO

terms and where the difference between the models was in the inclusion or not of the Born terms. Concretely, "Model c" and "Model s" from [23], and fits "c" and "u" from [15]. Specifically, these works showed therein that the inclusion of the Born terms led to rather small changes in the fitting parameters and did not influence significantly the quality of the fits; although in some cases it helped in producing more natural values of the subtraction constants. A similar behaviour when the Born diagrams are included is observed in [19]. Taking this into consideration and for simplicity, in a first stage of our study, which culminates with [27], the Born contributions were disregarded, leaving the NLO term as the significant correction to the WT term in order to reach good agreement between the theoretical predictions and the experimental data in the $K\Xi$ channels.

In summary, since the null direct contribution of the WT term to the scattering amplitude for $K^- p \to K\Xi$ reactions and the assumed non significant contribution of the Born terms confer a relevant role to the NLO terms, the inclusion of experimental data coming from these reactions in a fitting procedure might allow us to get more reliable values of the NLO coefficients.

2.1.1 Fitting procedure and Data treatment I

With the aim of learning about the importance of the different terms of the chiral Lagrangian and, as a main goal, obtaining a reliable set of low-energy constants we performed four different fits. The first fit corresponds to a unitarized calculation employing the chiral Lagrangian up to the lowest order WT term. This involves the fitting of seven parameters: the pion decay constant f and the six subtraction constants $a_{\bar{K}N}$, $a_{\pi\Lambda}$, $a_{\pi\Sigma}$, $a_{\eta\Lambda}$, $a_{\eta\Sigma}$, and $a_{K\Xi}$. In principle, given that there are ten channels in this

sector, there should be the corresponding ten subtraction constants, but due to the isospin symmetry they become six. The second fit improves upon the first one by using up to the NLO terms of the interaction kernel, thus involving seven additional parameters: the NLO low energy constants b_0, b_D, b_F, d_1, d_2, d_3 and d_4. Similar to previous works, and to compare our results with them, these first and second fits ignore the experimental data corresponding to the $K\Xi$ channels and their results will be denoted by **WT (no $K\Xi$)** and **WT+NLO (no $K\Xi$)**, respectively. From the prediction of the $K\Xi$ cross sections given by these fits, we will demonstrate clearly the important role that the NLO terms have on the $K^-p \to K\Xi$ reactions. This brings up, naturally, the study of the third and fourth fits, denoted by **WT** and **WT+NLO**, respectively, which correspond to the same fitting procedures than the first and second ones but including the $K\Xi$ production cross section data.

The observables employed in the fits need to be defined, all of them requiring the knowledge of the T matrix. As was shown in Sect 1.3, when one has decided which are the contributions to the interaction kernel, the scattering amplitudes is obtained by means of eq. (1.68). Once it is known, one can obtain the unpolarized differential and total cross-section, according to the normalization we use, for the $i \to j$ reaction:

$$\sigma_{ij} = \frac{1}{4\pi}\frac{M_i M_j}{s}\frac{k_j}{k_i} S_{ij} \ , \tag{2.1}$$

where s is the square of the center-of-mass (CM) energy, and we have averaged over the initial baryon spin projections and resummed over the final baryon spin projections:

$$S_{ij} = \frac{1}{2}\sum_{s',s} |T_{ij}(s',s)|^2 \ . \tag{2.2}$$

The K^-p scattering length is obtained from the K^-p scattering amplitude at threshold as:

$$a_{K^-p} = -\frac{1}{4\pi}\frac{M_p}{\sqrt{M_p + M_{\bar{K}}}} T_{K^-p\to K^-p} \ , \tag{2.3}$$

where we have used the following notation

$$T_{ij} = \frac{1}{2}\sum_{s',s} T_{ij}(s',s) \ . \tag{2.4}$$

The scattering length is related to the energy shift and width of the $1s$ state of kaonic hydrogen via the second order corrected Deser-type formula [69] :

$$\Delta E - i\frac{\Gamma}{2} = -2\alpha^3 \mu_r^2 a_{K^-p}\Big[1 + 2a_{K^-p}\,\alpha\,\mu_r\,(1 - \ln\alpha)\Big], \tag{2.5}$$

where α is the fine-structure constant and μ_r the reduced mass of the K^-p system.

From the elastic and inelastic K^-p cross sections evaluated at threshold, one can also obtain the following measured branching ratios of cross section yields:

$$\gamma = \frac{\Gamma(K^-p \to \pi^+\Sigma^-)}{\Gamma(K^-p \to \pi^-\Sigma^+)}, \tag{2.6}$$

$$R_n = \frac{\Gamma(K^-p \to \pi^0\Lambda)}{\Gamma(K^-p \to \text{neutral states})}, \tag{2.7}$$

$$R_c = \frac{\Gamma(K^-p \to \pi^+\Sigma^-, \pi^-\Sigma^+)}{\Gamma(K^-p \to \text{inelastic channels})} \ . \tag{2.8}$$

We considered a large amount of cross section data for K^-p scattering and related channels [70–80]. Some points of these data sets have inconsistencies with the trend of the neighbouring points and have not been employed in the fitting procedure, leaving us with a total of 161 experimental points coming from K^-p scattering. There are three

Observable	Points	Observable	Points
$\sigma_{K^-p\to K^-p}$	23	$\sigma_{K^-p\to \bar{K}^0 n}$	9
$\sigma_{K^-p\to \pi^0\Lambda}$	3	$\sigma_{K^-p\to \pi^0\Sigma^0}$	3
$\sigma_{K^-p\to \pi^-\Sigma^+}$	20	$\sigma_{K^-p\to \pi^+\Sigma^-}$	28
$\sigma_{K^-p\to K^+\Xi^-}$	46	$\sigma_{K^-p\to K^0\Xi^0}$	29
γ	1	ΔE_{1s}	1
R_n	1	Γ_{1s}	1
R_c	1		

Table 2.1: Number of experimental points used in our fits, distributed per observable.

excluded points and, therefore, we cannot give systematic criteria to exclude a point from the the fit. We have excluded the points which produced a much higher χ^2 than the neighbouring ones. The points eliminated will be displayed in red in the figures. We also fit the parameters of our model to the measured branching ratios [81, 82]

$$\begin{aligned} \gamma &= 2.36 \pm 0.04 \ , \\ R_n &= 0.664 \pm 0.011 \ , \\ R_c &= 0.189 \pm 0.015 \ , \end{aligned}$$

and to the recent energy shift and width of the $1s$ state of kaonic hydrogen obtained by the SIDDHARTA Collaboration [18], namely $\Delta E_{1s} = 283 \pm 36$ and $\Gamma_{1s} = 541 \pm 92$. The distribution of points per observable is summarized in Table 2.1.

The standard fitting procedure consists of minimizing $\chi^2_{\text{d.o.f.}}$, defined as:

$$\chi^2_{\text{d.o.f.}} = \frac{1}{\sum_{k=1}^{K} n_k - p} \sum_{k=1,i=1}^{K,n_k} \frac{\left(y^{\text{th}}_{i,k} - y^{\text{exp}}_{i,k}\right)^2}{\sigma^2_{i,k}} \tag{2.9}$$

where $y^{\text{exp}}_{i,k}$, $y^{\text{th}}_{i,k}$ and $\sigma_{i,k}$ represent, respectively, the experimental value, theoretical pre-

diction and error of the i^{th} point of the k^{th} observable, which has a total of n_k points, K is the total number of observables, and p denotes the number of free fitting parameters. This previous definition could suppress the relevance in the fit of observables which have a small number of associated experimental points, in favour of those with a larger set. To circumvent this problem, we adopt the method already used in [12,19,21,22], which takes a normalized χ^2 that assigns equal weight to the different measurements. This is achieved by averaging over the different experiments the corresponding χ^2 per degree of freedom, which is obtained by dividing the contribution of the experiment, χ^2_k, by its own number of experimental points, n_k. More explicitly, the redefined χ^2 per degree of freedom, which we will use in this work, is given by the expression

$$\chi^2_{\text{d.o.f}} = \frac{\sum_{k=1}^{K} n_k}{\left(\sum_{k=1}^{K} n_k - p\right)} \frac{1}{K} \sum_{k=1}^{K} \frac{\chi^2_k}{n_k} \tag{2.10}$$

with

$$\chi^2_k = \sum_{i=1}^{n_k} \frac{\left(y^{\text{th}}_{i,k} - y^{\text{exp}}_{i,k}\right)^2}{\sigma^2_{i,k}} \ .$$

The analysis for the χ^2 function was carried out by means of the minimization techniques embedded in the MINUIT package. MINUIT is a very powerful tool for minimizing a function and for special error analysis. In principle it was thought, more than 25 years ago, as a code to process experimental data recorded at CERN, but its great success in other fields have made MINUIT one of the most popular packages dedicated to these purposes.

	γ	R_n	R_c	$a_p(K^-p \to K^-p)$	ΔE_{1s}	Γ_{1s}
WT (no $K\Xi$)	2.37	0.191	0.665	$-0.76 + \mathrm{i}\,0.79$	316	511
NLO (no $K\Xi$)	2.36	0.188	0.662	$-0.67 + \mathrm{i}\,0.84$	290	559
WT	2.36	0.192	0.667	$-0.76 + \mathrm{i}\,0.84$	318	543
NLO	2.36	0.189	0.664	$-0.73 + \mathrm{i}\,0.85$	310	557
Exp.	2.36	0.189	0.664	$-0.66 + \mathrm{i}\,0.81$	283	541
	± 0.04	± 0.015	± 0.011	$(\pm 0.07) + \mathrm{i}\,(\pm 0.15)$	± 36	± 92

Table 2.2: Threshold observables obtained from the **WT (no $K\Xi$)**, **WT+NLO (no $K\Xi$)**, **WT** and **WT+NLO** fits explained in the text. Experimental data is taken from [18, 81, 82].

2.1.2 Results and discussion I

The results obtained with the four previously discussed fits are shown in this section. These fits consist of models whose interaction kernels are based on a WT contribution with or without the NLO corrections and whether or not we consider the experimental data of the $K\Xi$ channels.

The values for the threshold observables are collected in Table 2.2. A similar degree of accuracy is reached by all the fits in order to reproduce the branching ratios, the K^-p scattering length and the related energy shift and width of the $1s$ state of kaonic hydrogen, which is also shown in the table for completeness. Actually, only the first and third fits, obtained with the lowest order WT kernel, seem to produce a worse value of the real part of a_{K^-p}, past the upper limit of its error band.

At the beginning of this chapter, based on the evidence provided by previous works in the literature, the dominant role of the WT contribution was stressed in order to reproduce the total cross sections of the classical channels ($K^-p \to K^-p$, $\bar{K}^0 n$, $\pi^-\Sigma^+$,

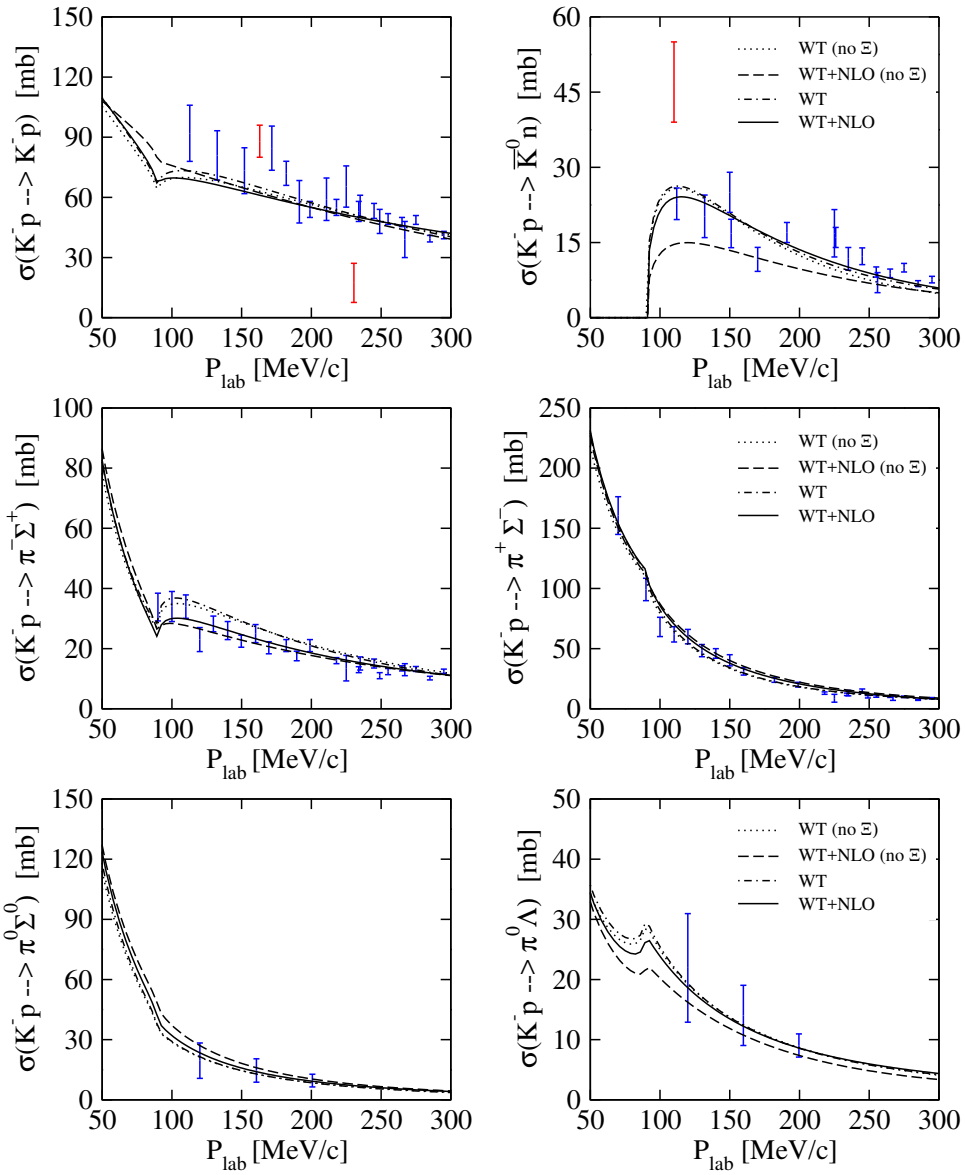

Figure 2.1: Total cross sections for the $K^-p \to K^-p, \bar{K}^0n, \pi^-\Sigma^+, \pi^+\Sigma^-, \pi^0\Sigma^0, \pi^0\Lambda$ reactions obtained from the **WT (no $K\Xi$)** fit (dotted line), the **WT+NLO (no $K\Xi$)** fit (dashed line), the **WT** fit (dot-dashed line) and the **WT+NLO** fit (solid line), where the last two cases take into account the experimental data of the $K\Xi$ channels, see text for more details. Experimental data are from [70–73]. The points in red have not been included in the fitting procedure.

$\pi^+\Sigma^-$, $\pi^0\Sigma^0$, $\pi^0\Lambda$). Since the WT term depends on a single parameter f, one should expect similar values for the four values of f corresponding to the four fitting schemes.

In principle, they look very similar (see Table 2.3) but we should not be misled by these values because there is a high sensitivity of the WT terms to little variations of f. Regarding these variations of f and depending on the fitting scheme, we should not lose sight either of the fact that f should absorb higher order effects, if it corresponds to one of the WT fits, or that f should be some sort of average value between f_π and f_K, weighted by the number of observables involving each meson, in this first stage where only K and π mesons are present in the processes for which we have included experimental data. On the other hand, we must bear in mind that because of the unitarization, each fit/model makes f acquire different values in order to modulate the contribution of the kernel according to the associated set of subtraction constants coming from the dimensional regularization of the loops. In spite of the above facts, we observe a certain stability of the values of f for our different models, which is not present in other recent works [19, 21, 23]. This feature is going to remain, as we will show, for all our future models. The variations of f work in a very characteristic way in our case: when we add corrections to a WT model, the value of f tends to decrease at most by 1.3%, taking values between 110.30 and 111.79 MeV. Even so, as we will also see, when we include data coming from processes with η mesons in the fits, where one could expect higher values for f, this parameter remains within the previous range.

The f value combined with the rest of the parameters appearing in the different models (Table 2.3) produces, for all of them, a satisfactory reproduction of the total cross sections for the classical reactions as can be seen in Fig. 2.1. However, substantial differences appear in the description of the $K^0\Xi^0$, $K^+\Xi^-$ production channels, displayed in Fig. 2.2. The results of the **WT (no $K\Xi$)** fit, represented by dotted lines, do not agree with size of the cross section in any of these reactions. The predicted cross sections amount to less than 0.015 mb, i.e. one order of magnitude smaller than the measured

ones. This is not a surprising result, because there is no direct contribution from the reactions $K^-p \to K^0\Xi^0, K^+\Xi^-$ at lowest order, since the coefficient C_{ij} in Eq. (1.59) is 0 in both cases (see Table 4.1 in Appendix A). Consequently, the only contribution to the scattering amplitude of these channels comes from the effect of the rescattering terms generated by the coupled channels unitarization, which is not sufficient to reproduce the strength of these cross sections. The inclusion of the NLO correction in the interaction kernel (**WT+NLO (no $K\Xi$)** fit) confirms their determining role in acquiring enough strength to describe the scattering data of the $K^-p \to K^0\Xi^0, K^+\Xi^-$ reactions. Even if the experimental data for these reactions has not been employed in this fit, the **WT+NLO (no $K\Xi$)** result gives a larger amount of strength for these channels, especially in the case of the $K^+\Xi^-$ production reaction, where the prediction even overshoots the data considerably as can be appreciated from the dashed lines in Fig. 2.2. We observe that, contrary to what happens to the contributions from the reactions $K^-p \to K^0\Xi^0, K^+\Xi^-$ at lowest order, the non vanishing contribution of NLO terms is guaranteed since the $L_{K^-p\to K\Xi}$ coefficients of the potential of Eq. (1.65) have non-zero values (see Table 4.2 in Appendix A). The obvious next step is to include the $K\Xi$ data in the fitting procedure and, naturally, the **WT+NLO** results, represented by the solid lines, reproduce quite satisfactorily the $K^-p \to K^0\Xi^0, K^+\Xi^-$ cross sections. For completeness, we also attempted to reproduce these reactions employing only the lowest order Lagrangian. The corresponding **WT** results, represented by the dot-dashed lines, improve considerably over those of the WT (no $K\Xi$) fit, but the fact that the lowest order Lagrangian can only affect these channels through unitarization, gives rise to quite unphysical values for the fitted subtraction constants, as commented below.

One can find the values of the parameters of the four fits discussed in this section displayed in Table 2.3, together with the obtained value of $\chi^2_{\text{d.o.f.}}$. We should com-

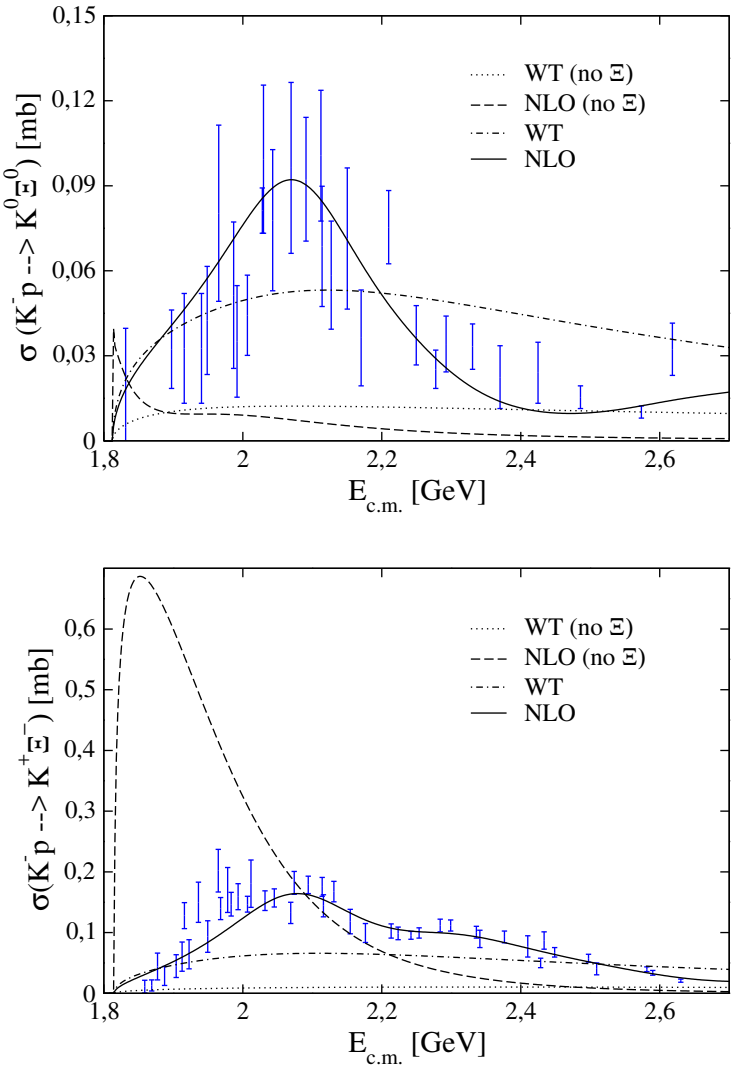

Figure 2.2: The total cross sections of the $K^-p \to K^0\Xi^0, K^+\Xi^-$ reactions obtained from the **WT (no $K\Xi$)** fit (dotted line), the **WT+NLO (no $K\Xi$)** fit (dashed line), the **WT** fit (dot-dashed line) and the **WT+NLO** fit (solid line). Experimental data are from [74–80].

ment that the larger value of $\chi^2_{\text{d.o.f.}}$ in the **WT+NLO** fit with respect to that of the **WT+NLO (no $K\Xi$)** one is precisely due to the contribution of the set of $K\Xi$ data, with more disperse experimental points, rather than to a loss of accuracy in reproducing the measurements. The reduction of the $\chi^2_{\text{d.o.f.}}$ values when including the NLO

	WT (no $K\Xi$)	NLO (no $K\Xi$)	WT	NLO
$a_{\bar{K}N}$ (10^{-3})	-1.681 ± 0.738	5.151 ± 0.736	-1.986 ± 2.153	6.550 ± 0.625
$a_{\pi\Lambda}$ (10^{-3})	33.63 ± 11.11	21.61 ± 10.00	-248.6 ± 122.0	54.84 ± 7.51
$a_{\pi\Sigma}$ (10^{-3})	0.048 ± 1.925	3.078 ± 2.101	0.382 ± 2.711	-2.291 ± 1.894
$a_{\eta\Lambda}$ (10^{-3})	1.589 ± 1.160	-10.460 ± 0.432	1.696 ± 2.451	-14.16 ± 12.69
$a_{\eta\Sigma}$ (10^{-3})	-45.87 ± 14.06	-8.577 ± 0.353	277.8 ± 139.1	-5.166 ± 0.068
$a_{K\Xi}$ (10^{-3})	-78.49 ± 47.92	4.10 ± 12.67	30.85 ± 10.58	27.03 ± 7.83
f/f_π	1.202 ± 0.053	1.186 ± 0.012	1.202 ± 0.119	1.197 ± 0.008
b_0 (GeV^{-1})	-	-0.861 ± 0.014	-	-1.214 ± 0.014
b_D (GeV^{-1})	-	0.202 ± 0.011	-	0.052 ± 0.040
b_F (GeV^{-1})	-	0.020 ± 0.057	-	0.264 ± 0.146
d_1 (GeV^{-1})	-	0.089 ± 0.096	-	-0.105 ± 0.056
d_2 (GeV^{-1})	-	0.598 ± 0.062	-	0.647 ± 0.019
d_3 (GeV^{-1})	-	0.473 ± 0.026	-	2.847 ± 0.042
d_4 (GeV^{-1})	-	-0.913 ± 0.031	-	-2.096 ± 0.024
$\chi^2_{\text{d.o.f.}}$	0.62	0.39	2.57	0.65

Table 2.3: Values of the parameters and the corresponding $\chi^2_{\text{d.o.f.}}$, defined as in eq. (2.10), for the different fits described in the text. The value of the pion decay constant is $f_\pi = 93$ MeV and the subtraction constants are taken at a regularization scale $\mu = 1$ GeV.

terms in the Lagrangian is clearly observed by comparing with the corresponding WT fits at lowest order, especially when the $K\Xi$ data has been included.

Another interesting feature reflected in Table 2.3 that also demonstrates the need of taking into account the NLO terms when the additional $K\Xi$ data is included are the large values assigned to the subtraction constants by the WT fits. Particularly, these fits, forced to accommodate the reproduction of the $K\Xi$ scattering data, produce subtraction constants in the isospin $I = 1$ channel, $a_{\pi\Lambda}$ and $a_{\eta\Sigma}$, which are one order of magnitude larger than what qualifies as being of "natural" size (see the detailed discussion at the end of Chapter 1). Conversely, the parameters obtained in the other

fits presented in Table 2.3 are of reasonable size. It is found that, within about 2σ of their errors, the values of the subtraction constants obtained in the **NLO (no $K\Xi$)** and **NLO** fits are quite similar. However, the values of the low energy constants of the NLO Lagrangian (b_0, b_D, b_F and d_i) obtained by the two fits show stronger differences. This means that these parameters are really sensitive to the data of the $K\Xi$ production reactions which should then be used to constrain their values, as was done in our work. This is supported, not only by the results presented in Table 2.2 and Fig. 2.1, where we find a slight improvement in reproducing the threshold observables and the $K^-p \to K^-p$, $\bar{K}^0n, \pi^-\Sigma^+, \pi^+\Sigma^-, \pi^0\Sigma^0, \pi^0\Lambda$ cross sections, but also, and more especially, in the total cross section of the $K\Xi$ channels, which cannot be reproduced if the NLO terms are omitted. Hence, based on the previous evidence, we can conclude that the $K^-p \to K\Xi$ cross sections are crucial to constrain more precisely the low energy constants of the NLO Lagrangian.

2.2 Influence of the Born terms

Until this point, we studied the meson-baryon interaction in the $S = -1, Q = 0$ sector, by means of a chiral $SU(3)$ Lagrangian up to next-to-leading order and implementing unitarization in coupled channels, aiming for a better comprehension of the relevance and the role played by the terms next in hierarchy after the WT one. The parameters of the Lagrangian were fitted to a large set of experimental scattering data in different two-body channels, to γ, R_n and R_c branching ratios, and to the precise SIDDHARTA value of the energy shift and width of kaonic hydrogen. In contrast to all previous works, a special attention was paid to the $K\Xi$ production reactions because they do not

receive direct lowest order contributions from the WT term and the rescattering terms are insufficient to reproduce the experimental data properly. By comparing different fitting procedures, it was indeed found that the NLO terms were crucial to obtain a good reproduction of the $\bar{K}N \to K^+\Xi^-, K^0\Xi^0$ cross sections. Once the sensitivity of the NLO Lagrangian to the $K^-p \to K\Xi$ reactions was established, the values of the low energy constants of the NLO chiral Lagrangian obtained, by implementing the cross section data for $K\Xi$ production in the fitting procedure, not only were accurate but they were more reliable.

The previous study was carried out under the assumption that, at lowest order, the contribution of the s and u-channel diagrams involving the coupling of the meson-baryon channel to an intermediate baryon state would be very moderate. But one should wonder whether the inclusion of the Born terms in the interaction kernel when the $K\Xi$ production reactions are taken into account in the fits is, as we supposed, a mere correction or, on the contrary, it reveals as a significant contribution. And, whatever the case, what effects they might have on the values of the NLO coefficients. To check this, we performed a new study [28] whose interaction kernel took into account the Born diagrams. The results and implications of this study are explained in the following subsections.

2.2.1 Fitting procedure and Data treatment II

A fit was performed in an attempt to clarify the importance of the different terms of the chiral Lagrangian. This fit, called **WT+NLO+Born**, corresponds to a unitarized calculation employing the chiral Lagrangian at NLO, that is, an interaction kernel which incorporates the contribution of the WT, the Born and the NLO terms. Tech-

nically speaking, it involves the fitting of sixteen parameters: the pion decay constant f, the six subtraction constants $a_{\bar{K}N}$, $a_{\pi\Lambda}$, $a_{\pi\Sigma}$, $a_{\eta\Lambda}$, $a_{\eta\Sigma}$, and $a_{K\Xi}$, the axial vector couplings of the baryons to the mesons D, F and the NLO low energy constants b_0, b_D, b_F, d_1, d_2, d_3 and d_4. In principle, the axial vector couplings undergo the constraint $g_A = D + F = 1.26$, but we decided to relax their values by allowing them to be within 12.5% of their canonical value, $D = 0.8$ And $F = 0.46$ [83], in order to accomodate the dispersion of the values seen in the literature.

Regarding the observables to which the model was fitted by means of the minimization of the same $\chi^2_{\text{d.o.f}}$ employed in Sect. 2.1.1, these are the same ones displayed in Table 2.1 in Sect. 2.1.1. For consistency, the same three points, which are represented in red in the figures, were disregarded. As we will appreciate there these points fell completely outside of our error bands. In summary, 166 points are included in the fit.

The error bands were also estimated for the $K^- p$ scattering cross sections into different final meson-baryon channels for the previous fit. We followed the method employed in Ref. [21] for our definition of χ^2, eq. (2.10), which is proposed in an earlier study [84]. First of all, we calculated the *correlated* error bars for our model parameters, by generating new parameter configurations by randomly varying all the free parameters around their central values through a Monte Carlo generator, and rejecting those configurations for which the corresponding value of χ^2 (total) satisfies

$$\chi^2 > \chi^2_0 + \chi^2(p, 1\sigma)\,, \tag{2.11}$$

where χ^2_0 corresponds to the minimum found by MINUIT and $\chi^2(p, 1\sigma)$ is the value of a chi-squared distribution with a number p of d.o.f. at a confidence level of one

sigma. In the next step, we generated 16.000 of new parameter configurations by randomly varying all the free parameters within the obtained correlated error bars, and the $K^- p$ scattering cross sections obtained for these configurations determine their corresponding error bands. Similarly, we can also associate error bars to the threshold observables from the values obtained with these new configurations.

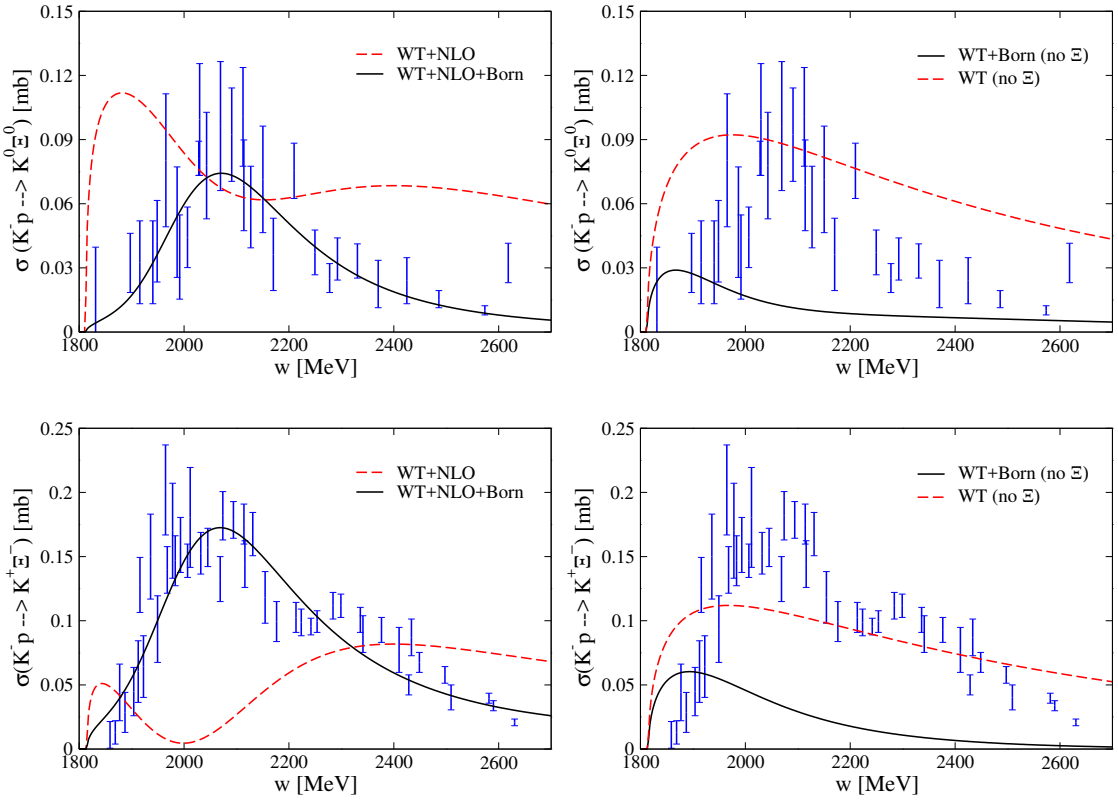

Figure 2.3: *Left column:* Total cross sections for the $K^- p \to K^0\Xi^0, K^+\Xi^-$ reactions obtained from the **WT+NLO+Born** fit (solid line), and the similar result neglecting the contributions from the Born terms (dashed line), see text for more details. Experimental data are from [74–80]. *Right column:* The same as the left column, but the solid line corresponds to WT+Born fit, where the presented $K^- p \to K^0\Xi^0, K^+\Xi^-$ were not taken into account, see text for more details. The dashed line shows the similar result neglecting the contributions from the Born terms.

2.2.2 Results and discussion II

In our first approach, we disregarded the Born terms from the interaction kernel assuming that they contribute marginally in the reproduction of the experimental data. As we have mentioned, this idea was reinforced by the authors of [15,19,23] where these terms have little influence in the goodness of the fits. As pointed out in the beginning of this chapter, the only significant difference of our model with respect to the previous studies is the inclusion of the $\bar{K}N \to K\Xi$ data. Thus, to settle how important the Born terms are, an analysis of their effects on these reactions should be enough.

For this purpose, we display in Fig. 2.3 (left column) our results of the fit called **WT+NLO+Born** (solid line), together with the results of the same fit but setting the contributions from the Born diagrams in Eq. (1.66) to zero (dashed line). As one can see, accounting or not for the Born terms leads to substantial changes in the $K\Xi$ production cross sections, meaning that these terms contribute at the same order of the other terms in the Lagrangian with which they can interfere strongly. The above statement is reconfirmed by the right column in Fig. 2.3, where we presented the **WT+Born(no Ξ)** fit (solid line), together with the results of the same fit but omitting the contributions from the Born diagrams. This fit, which is based on an interaction kernel that takes into account the WT and the Born terms, has only been performed here to help in the understanding of this point. A further study of this model makes no sense since, as can be observed from this same figure, it is far from accommodating to the experimental data and, what is even more important, the NLO contribution, which is the crucial ingredient, is not taken into account in the interaction kernel. These plots clearly show that the importance of the Born terms for the $K\Xi$ production reactions is not related to the inclusion of the NLO terms. In other words, for these particular

channels the strength coming from WT term, Born terms and NLO terms are of the same order, and should all be taken into account.

The relevance of the Born diagrams of the chiral model in the $\bar{K}N \to K^+\Xi^-, K^0\Xi^0$ cross sections may not come as a surprise if one considers that a recent work, studying these reactions from a phenomenological resonance model [85], also finds substantial contributions coming from the exchange of the ground state $1/2^+$ hyperons in s- and u-channel exchange configurations.

We next present all the results of our fit when the Born terms are included as described in the previous section. The model parameters obtained in this fit and the final $\chi^2_{\rm d.o.f}$ are summarized in Table 2.4, where the same outputs from other models have been included for comparison. The results for the observables are shown in Table 2.5 and Fig. 2.4, and, as in the previous case, results from other models are included. In particular, these additional results come from the **WT+NLO** fit described in Sect. 2.1.1 and **WT+NLO+Born (η chan)** which is going to be introduced in the next section. In Fig. 2.4, we also present our estimation of the error bands of the K^-p scattering cross sections into different final channels for **WT+NLO+Born** fit that gives $\chi^2_0 = 0.73\left(\sum_{k=1}^{K} n_k - p\right)$. In our particular case we have $\sum_{k=1}^{K} n_k = 166$, $p = 16$, $\chi^2(16, 1\sigma) = 18.07$, and thus the rejection condition, Eq. (2.11), leads to $\chi^2_{\rm d.o.f} > 0.85$. As one can appreciate, the overall agreement with the experimental data is very good.

From the results of the threshold observables in Table 2.5, comparing the **WT+NLO** and **WT+NLO+Born** fits, we note that the inclusion of the Born terms favours very slightly the agreement with the corresponding experimental data. This is not the case if we turn to Table 2.4 where the goodness of our **WT+NLO+Born** fit, signalled by the $\chi^2_{\rm d.o.f.}$ value, is almost the same as that of the corresponding **WT+NLO** fit,

	WT+NLO Results I	WT+NLO+Born Results II	WT+NLO+Born (η chan) Results III
$a_{\bar{K}N}$ (10^{-3})	6.55 ± 0.63	1.77 ± 2.38	1.27 ± 0.12
$a_{\pi\Lambda}$ (10^{-3})	54.8 ± 7.5	55.2 ± 13.5	-6.1 ± 12.9
$a_{\pi\Sigma}$ (10^{-3})	-2.29 ± 1.89	2.33 ± 3.17	0.68 ± 1.43
$a_{\eta\Lambda}$ (10^{-3})	-14.2 ± 12.7	8.00 ± 5.04	-0.67 ± 1.06
$a_{\eta\Sigma}$ (10^{-3})	-5.17 ± 0.07	6.5 ± 20.6	8.00 ± 3.26
$a_{K\Xi}$ (10^{-3})	27.0 ± 7.8	-9.04 ± 3.63	-2.51 ± 0.99
f/f_π	1.20 ± 0.01	1.21 ± 0.03	1.20 ± 0.03
b_0 (GeV^{-1})	-1.21 ± 0.01	-0.70 ± 0.23	0.13 ± 0.04
b_D (GeV^{-1})	0.05 ± 0.04	0.31 ± 0.20	0.12 ± 0.01
b_F (GeV^{-1})	0.26 ± 0.15	0.65 ± 0.41	0.21 ± 0.02
d_1 (GeV^{-1})	-0.11 ± 0.06	0.17 ± 0.26	0.15 ± 0.03
d_2 (GeV^{-1})	0.65 ± 0.02	0.17 ± 0.11	0.13 ± 0.03
d_3 (GeV^{-1})	2.85 ± 0.04	0.37 ± 0.16	0.30 ± 0.02
d_4 (GeV^{-1})	-2.10 ± 0.02	0.01 ± 0.09	0.25 ± 0.03
D	-	0.90 ± 0.10	0.70 ± 0.16
F	-	0.40 ± 0.08	0.51 ± 0.11
$\chi^2_{\text{d.o.f.}}$	0.65	0.73	1.14*

Table 2.4: Values of the parameters and the corresponding $\chi^2_{\text{d.o.f.}}$, defined in eq. (2.10), for the different fits described in the text. The subtraction constants are taken at a regularization scale $\mu = 1$ GeV. The error bars of the parameters are those given by the MINUIT minimization procedure. * The higher value of the $\chi^2_{\text{d.o.f.}}$ could mislead the reader, but one should keep in mind that 58 additional experimental points from the η channels had been included in the fitting procedure.

even a little bit worse. The fact that the Born terms do not help obtaining smaller values of the χ^2 is not a novelty, as we mentioned it was one of the effects induced by the Born terms that had been seen in [15, 19, 23]. In those studies, as in the present one, the values of the subtraction constants corresponding to **WT+NLO+Born** are much closer to the 'natural size' compared to the ones in **WT+NLO**, in spite of the substantial associated errors. As a comment with respect to the axial vector couplings,

	γ	R_n	R_c	$a_p(K^-p \to K^-p)$	ΔE_{1s}	Γ_{1s}
WT+NLO	2.36	0.189	0.664	$-0.73 + \mathrm{i}\,0.85$	310	557
WT+NLO+Born	2.36	0.191	0.664	$-0.67 + \mathrm{i}\,0.84$	291	558
WT+NLO+Born (η chan)	2.36	0.188	0.659	$-0.65 + \mathrm{i}\,0.88$	288	588
Exp.	2.36 ± 0.04	0.189 ± 0.015	0.664 ± 0.011	$(\pm 0.07) + \mathrm{i}\,(\pm 0.15)$	283 ± 36	541 ± 92

Table 2.5: Threshold observables obtained from the fits explained in the text. Experimental data is taken from [18, 81, 82].

one can appreciate that the D and F parameters of the Born contributions reached the edges of their allowed range, but in a way that their sum stays rather close to its nominal value $g_A = D + F = 1.26$ [83].

The most striking feature revealed in Table 2.4 is the very different sets of NLO parameters acquired by means of the **WT+NLO+Born** and **WT+NLO** fits. In principle, we expected a similar behaviour for the NLO coefficents to the one exhibited by the models studied in [15,23]. In these works, after obtaining a parametrization for a model consisting of an interaction kernel which considers WT and NLO contributions, the further impact of the systematic inclusion of the Born terms was discussed. In [23], the authors obtained, apart from the b_D parameter, very similar parametrizations for "Model c" and "Model s", and the same occurred with models "Model c", "Model s" and "Model u" in [15] differing notably only in b_F. Again, since [15, 23] only employed the classical channels in the fitting procedure, the different parameters we obtain when the Born terms are considered is a clear signal of the significant role played by the Born contributions once the $K\Xi$ channels are included in the fits.

The $K^-p \to K^-p$, $\bar{K}^0n$, $\pi^-\Sigma^+$, $\pi^+\Sigma^-$, $\pi^0\Sigma^0$, $\pi^0\Lambda$, $K^0\Xi^0$, $K^+\Xi^-$ total cross sec-

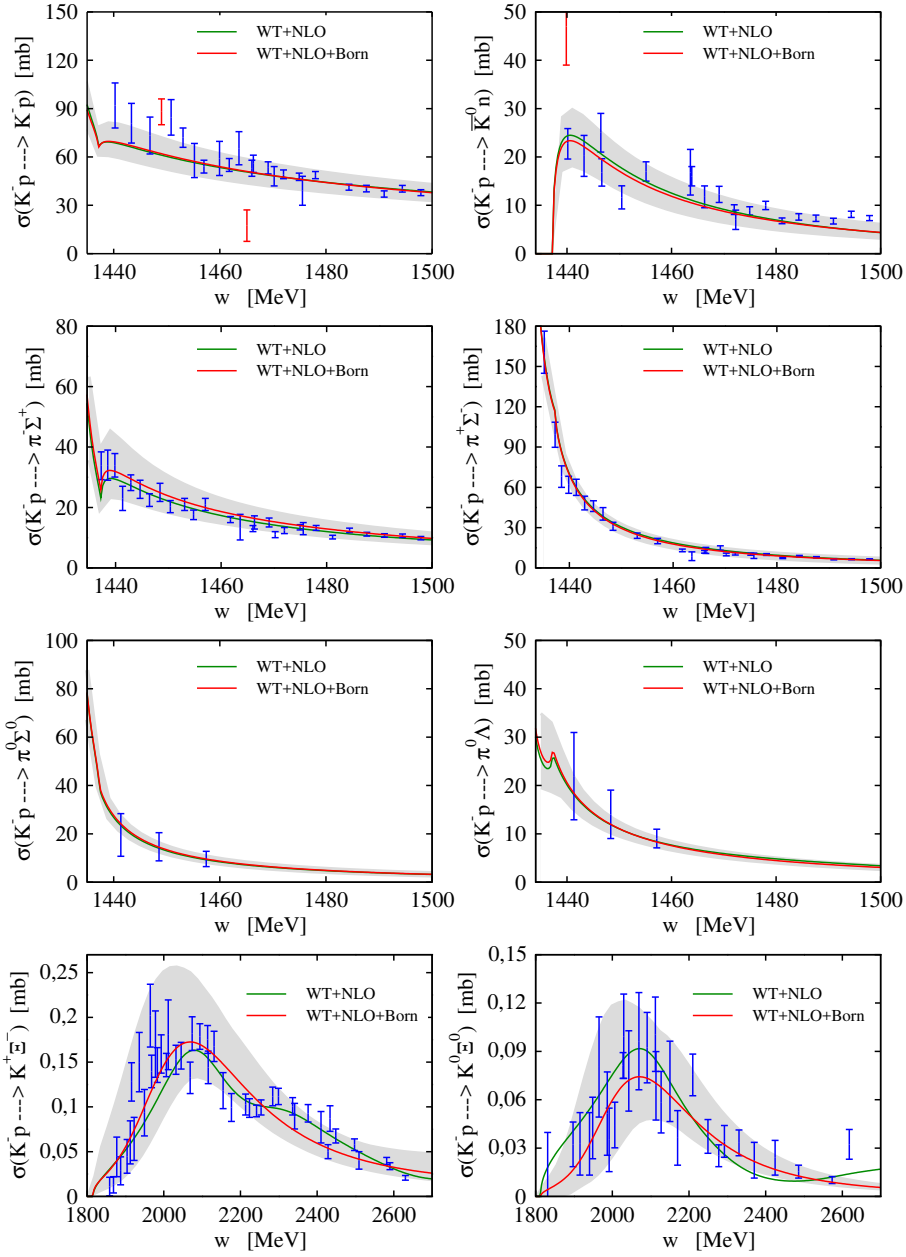

Figure 2.4: Total cross sections for the $K^-p \to K^-p$, $\bar{K}^0n$, $\pi^-\Sigma^+$, $\pi^+\Sigma^-$, $\pi^0\Sigma^0$, $\pi^0\Lambda$, $K^0\Xi^0$, $K^+\Xi^-$ reactions obtained for **WT+NLO** fit (green line) and **WT+NLO+Born** fit (red line), with our estimation of the corresponding error bars (grey area), see text for more details. Experimental data are from [70–80]. The points in red have not been included in the fitting procedure.

tions obtained from the **WT+NLO** fit (green line) and **WT+NLO+Born** fit (red line) are compiled in Fig. 2.4. As can be appreciated from the six upper panels, there are not any substantial differences between the models when reproducing the classical channels, although both models present notable differences, such as the corresponding parametrizations for the NLO constants and the inclusion or not of the Born terms. These results can be explained by considering the similar f values for the two models combined with the well-known dominant role played by the WT term for the classical channels. Concerning the $K^-p \to K^0\Xi^0$ cross section, one could say that the experimental data on the lower and higher energy tails are best described by the **WT+NLO+Born** fit; while one observes that the **WT+NLO** one is able to better describe the details of the structure shown by the experimental points of the $K^-p \to K^+\Xi^-$ cross section. The interesting point here, despite both models peaking at the same energy for the two cross sections probably forced by the fitting procedure, is the opposite behaviour in the size of their maxima. In the case of the $K^-p \to K^0\Xi^0$ reaction, the **WT+NLO+Born** model gives more strength than the **WT+NLO** one and, conversely, for the $K^-p \to K^+\Xi^-$ reaction the total **WT+NLO** cross section is slightly larger than the **WT+NLO+Born** one. This is clear evidence that these models have a different distribution for their isospin components which, obviously, is tied to the different parametrization and the nature of both models.

The scattering amplitude related to the $K^-p \to K\Xi$ processes can be expressed in terms of their isospin components according to:

$$\begin{aligned} \langle K^-p \mid T \mid K^+\Xi^-\rangle &= \frac{1}{2}\left[\langle \bar{K}N \mid T^{I=1} \mid K\Xi\rangle - \langle \bar{K}N \mid T^{I=0} \mid K\Xi\rangle\right] \\ \langle K^-p \mid T \mid K^0\Xi^0\rangle &= -\frac{1}{2}\left[\langle \bar{K}N \mid T^{I=1} \mid K\Xi\rangle + \langle \bar{K}N \mid T^{I=0} \mid K\Xi\rangle\right] . \end{aligned} \quad (2.12)$$

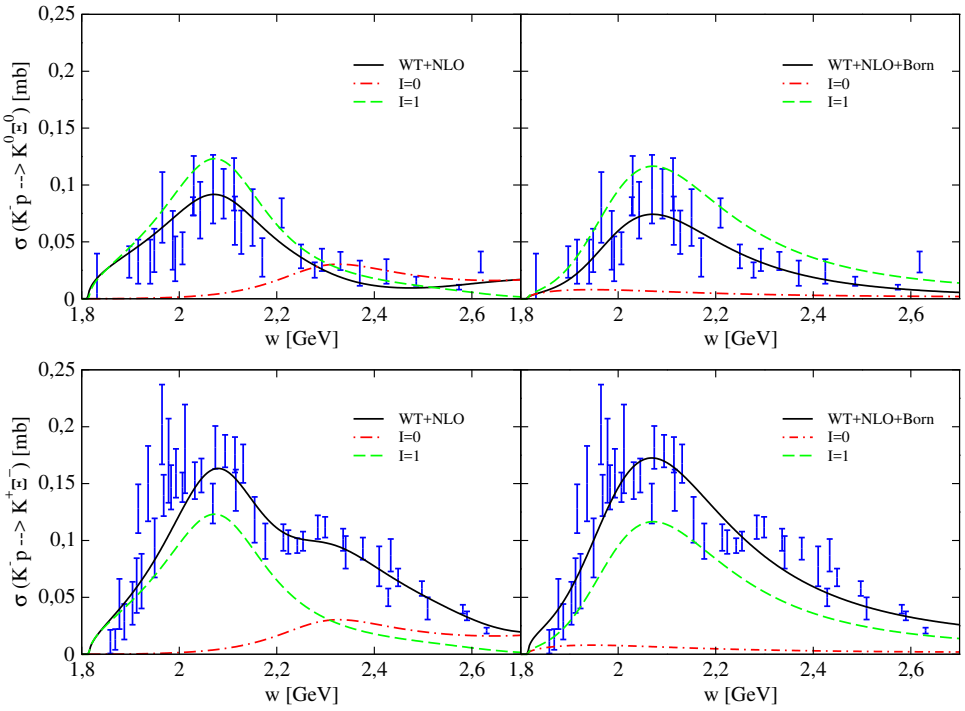

Figure 2.5: The total cross section data of the $K^-p \to K^0\Xi^0$ reaction is represented in the top panels, where the left figure corresponds to the **WT+NLO** model and the right one corresponds to the **WT+NLO+Born** model. The same distribution for the bottom panels where the $K^-p \to K^+\Xi^-$ cross section data is represented. The figure shows the complete results by means of solid lines, the results where only isospin $I = 1$ component (green dashed lines) or $I = 0$ one (red dot-dashed line) have been retained.

A better understanding of the physics embedded in each of these two parametrizations emerges when splitting the $K^-p \to K\Xi$ cross-section into the isospin basis ($I = 0$ and $I = 1$ components). This fact is illustrated in Fig. 2.5, where it is shown that the $I = 0$ components of these two models (red dot-dashed lines) are in opposition with each other. Being more precise, the $I = 0$ component of the **WT+NLO** model is concentrated at higher energies reaching its maximum at around 2300 MeV, while the corresponding $I = 0$ component for the **WT+NLO+Born** model presents a much lower strength and is located towards substantially smaller energies, peaking at around 1900 MeV. Regarding the $I = 1$ components (green dashed line), one can see that the

components for both models are almost coincident, peaking at around 2050 MeV, although the strength corresponding to **WT+NLO+Born** is a little larger in the whole range, being specially prominent at higher energies.

Such differences in the isospin components points towards the need to identify reactions that proceed through either $I = 0$ or $I = 1$, thereby acting as isospin selectors from which one can extract valuable information to constrain the parameters of the meson-baryon lagrangian better. Actually, since we have been studying the meson-baryon interaction in the $S = -1$ sector, the most natural filtering processes are the $K^- p \to \eta\Lambda, \eta\Sigma^0$ reactions, which are of pure isospin 0 and 1 respectively. Since the experimental data is already available [86–89], we could address these new incorporations in our approach. Actually, this is the topic discussed in the next section.

Another example of these filtering processes that we would also like to mention is the weak Λ_b decay into a J/Ψ and a meson-baryon pair, a reaction that filters the $I = 0$ component in the final meson-baryon state, as it was shown in [33, 90]. These decays are presently analysed by the CDF [91] and LHCb [40, 92, 93] collaborations. In particular, the $\Lambda_b \to J/\Psi\ K^-\ p$ decay has been employed very recently in [40] to claim the presence of an exotic pentaquark charmonium state in the $J/\Psi\, p$ channel. We devote the fourth chapter to this topic.

2.3 Isospin filtering processes I: $K^-p \to \eta\Lambda, \eta\Sigma^0$ reactions

In the previous section we concluded by appealing to processes which are able to filter isospin components to provide deeper constraints on our fitting parameters. In the present chapter, we study the effects of the inclusion of scattering data from the $K^-p \to \eta\Lambda, \eta\Sigma^0$ reactions, which are processes with single-isospin outgoing channels (0 and 1 respectively), in our most complete fit. Therefore, the new performed fit consists of an interaction kernel which takes into account the WT, the Born and NLO terms and considers scattering data from these new reactions [86–89] in addition to the data displayed in Table 2.1.

The parameters of this last fit, which is called **WT+NLO+Born (η chan)**, are displayed in the third column of Table 2.4. One can appreciate an overall improvement of the fitting parameters in terms of accuracy. Another remarkable result is that we obtained more natural sized values for all the subtraction constants compared with those of the other models shown in the same Table. But the most significant feature is the homogeneity achieved by the NLO coefficients. This leads us to believe that the inclusion of more experimental data from isospin filtering processes could favour the collection of more reliable values for the low energy constants.

Even though the models of Table 2.4 can not be compared directly in terms of $\chi^2_{\text{d.o.f.}}$, because we have included 58 additional experimental points, one can check the goodness of the new fit by looking at the agreement between experimental scattering data and the theoretical results present in Fig. 2.6, Fig. 2.7 and Table 2.5.

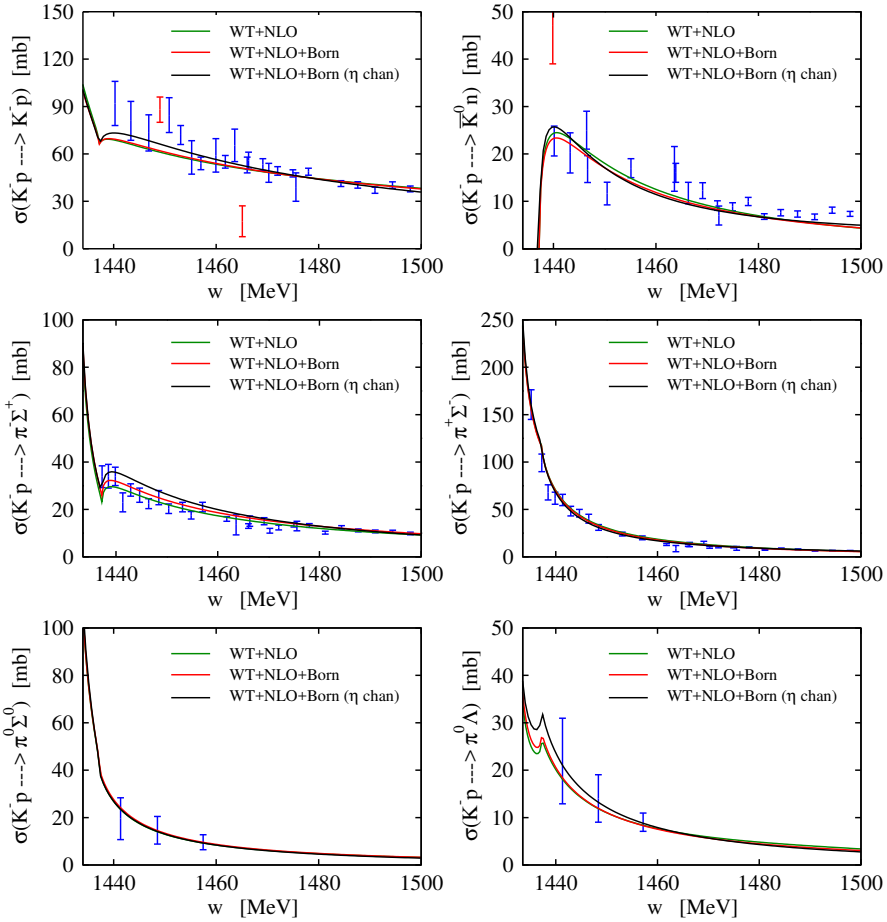

Figure 2.6: Total cross sections for the $K^-p \to K^-p, \bar{K}^0n, \pi^-\Sigma^+, \pi^+\Sigma^-, \pi^0\Sigma^0, \pi^0\Lambda$ reactions obtained from the **WT+NLO** fit (green line), the **WT+NLO+Born** fit (red line) and the **WT+NLO+Born (η chan)** fit (black line), see text for more details. Experimental data are from [70–73]. The points in red have not been included in the fitting procedure.

The total cross sections of the classical processes obtained by the **WT+NLO**, **WT+NLO+Born** and **WT+NLO+Born (η chan)** fits are represented in Fig. 2.6, all of them showing a rather good reproduction of the experimental data. This agreement is consequently reflected on the threshold observables, Table 2.5, which take values very close to the experimental data within the error range. The similarity of the three models, in the reproduction of these scattering data can be attributed to their

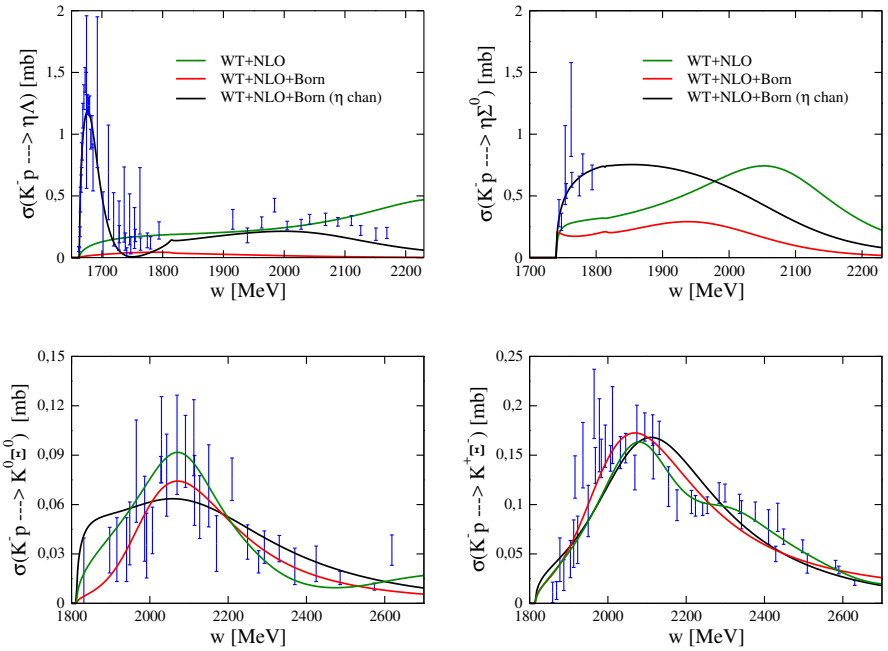

Figure 2.7: Total cross sections for the $K^-p \to \eta\Lambda, \eta\Sigma^0, K^0\Xi^0, K^+\Xi^-$ reactions obtained from the **WT+NLO** fit (green line), the **WT+NLO+Born** fit (red line) and the **WT+NLO+Born (η chan)** fit (black line), see text for more details. Experimental data are from [74–80, 86–89].

similar values of f parameter, since the dominant term for these channels is the WT one.

The novelty comes when inspecting the $K^-p \to \eta\Lambda, \eta\Sigma^0, K^0\Xi^0, K^+\Xi^-$ total cross sections, see Fig. 2.7. We observe that the cross sections of the η channels (top pannels in Fig. 2.7) can only be properly reproduced with the new fit performed **WT+NLO+Born (η chan)**, which dynamically generates the $\Lambda(1670)$ resonant structure seen in the $K^-p \to \eta\Lambda$ reaction. Concerning the $K\Xi$ channels (bottom pannels in Fig. 2.7), the three models give a similar good reproduction for the $K^-p \to K^+\Xi^-$ cross section, although the peak corresponding to the **WT+NLO+Born (η chan)** fit is shifted 50 MeV towards higher energy with respect to the other two coincident peaks. We also see that the older models (**WT+NLO** and **WT+NLO+Born**)

clearly offer a better agreement with the experiment than the new one for the $K^-p \to K^0\Xi^0$ cross section. In this last case, the inclusion of resonant terms similarly to what is done in [27] (and discussed in the third chapter of this thesis) could be very helpful to accommodate the theoretical cross section to the experimental data. An explicit inclusion of the $\Lambda(1890)$ could be a good strategy since it is located in this energy region and it is an isospin 0 resonance.

Let us note that the dynamical generation of the $\Lambda(1670)$ resonance, by means of an unitarized coupled-channels method using the lowest order (WT) chiral lagrangian with the N/D method, was studied in [94]. It was found that this resonance couples strongly to $K\Xi$, with the squared value of the corresponding coupling $|g_{\Lambda^* K\Xi}|^2 = 11$, being one or two orders of magnitude larger than the ones to other isospin 0 channels in the $S = -1$ sector. Despite higher order terms in the lagrangian, where not taken, the authors examined the role of this resonance, and hence of the rescattering terms that generate it, on the $K^-p \to K\Xi$ reactions. Actually, they checked the contribution of the tail of the $\Lambda(1670)$ resonance on the $K^-p \to K\Xi$ cross sections for a single laboratory K^- momentum of 1.6 GeV/c which corresponds to an energy more than 230 MeV above the $K\Xi$ threshold. The total cross section for this momentum calculated by their model reproduced the experimental value for the $K^-p \to K^+\Xi^-$ reaction, and they obtained three times the experimental value of the $K^-p \to K^0\Xi^0$ cross section. Note that our equivalent **WT (no Ξ)** model, presented in Sect. 2.1.1 gave much smaller results than the experimental cross sections (see Fig. 2.2). One can therefore think that there is a correlation between the ability of a model in reproducing the $\Lambda(1670)$ resonance and the simultaneous accommodation of the $K\Xi$ production cross sections.

Another interesting point of the study of Refs. [94] is the fact that the position

of the pole related to the $\Lambda(1670)$ is quite sensitive to the $a_{K\Xi}$ subtraction constant. Consequently, in order to better reproduce the position of the resonance found by experiment, while maintaining the agreement of the model with the low energy experimental data, they varied the value of this subtraction constant until fixing it to $a_{K\Xi} = -2.52$ which, in our mapping, is translated as $a_{K\Xi} = -3.77 \cdot 10^{-3}$. Interestingly, this last value differs by less than the associated error from the value given by the **WT+NLO+Born (η chan)** fit in Table 2.4.

2.4 Isospin filtering processes II: $K_L^0 p \to K^+ \Xi^0$ reaction

As we have seen in the previous section, processes which filter isospin can be helpful in order to constrain our models and, hence, allow one to get more realistic values of the corresponding low energy constants. The recent proposal [29] of creating a secondary K_L^0 beam at Jlab offers a great opportunity for measuring the $K_L^0 p \to K^+ \Xi^0$ reaction. Since $K_L^0 = (K^0 - \bar{K}^0)/\sqrt{2}$, the former reaction would proceed through the $\bar{K}^0$ component of the K_L^0, and, thus, would be of pure $I = 1$ character. Indeed, this is a reaction that involves channels of the $S = -1$ and $Q = +1$ sector, but taking advantage of the symmetry under the third component of isospin we can rewrite the amplitude of the previous reaction in terms of the $I = 1$ amplitudes built from the channels of our sector. To see this, we can start by writing the following isospin states

($|I\, I_3\rangle$):

$$\begin{aligned} |\bar{K}^0\rangle = |\frac{1}{2}\,\frac{1}{2}\rangle,\ |p\rangle = |\frac{1}{2}\,\frac{1}{2}\rangle \rightarrow \quad & |\bar{K}^0 p\rangle = |1\,1\rangle \\ |K^+\rangle = |\frac{1}{2}\,\frac{1}{2}\rangle,\ |\Xi^0\rangle = |\frac{1}{2}\,\frac{1}{2}\rangle \rightarrow \quad & |K^+\Xi^0\rangle = |1\,1\rangle. \end{aligned} \tag{2.13}$$

Next, knowing that $|K^0_L p\rangle$ initial state is expressed as $|K^0_L p\rangle = \frac{1}{\sqrt{2}}\left[|K^0 p\rangle - |\bar{K}^0 p\rangle\right]$, we can obtain the scattering amplitude for the $K^0_L p \rightarrow K^+\Xi^0$ reaction:

$$\begin{aligned} \langle K^+\Xi^0|T|K^0_L p\rangle &= \frac{1}{\sqrt{2}}\left[\langle K^+\Xi^0|T|K^0 p\rangle - \langle K^+\Xi^0|T|\bar{K}^0 p\rangle\right] \\ &= -\frac{1}{\sqrt{2}}\langle K^+\Xi^0|T|\bar{K}^0 p\rangle. \end{aligned} \tag{2.14}$$

In the last step, we have used that $\langle K^+\Xi^0|T|K^0 p\rangle = 0$. This is due to the fact that $|K^+\Xi^0\rangle$ is a $S = -1$ state and $|K^0 p\rangle$ is a $S = +1$ state and the strong interaction cannot couple states with different strangeness because it would violate the flavour symmetry. Note that the $\langle K^+\Xi^0|T|\bar{K}^0 p\rangle$ amplitude is of pure isospin $I = 1$ as can be seen from eqs. (2.13).

Involving the invariance of the strong interaction under I_3 rotations, this amplitude can be expressed in terms of states with $I_3 = 0$, which are the ones employed in our studies. Therefore, knowing that

$$\begin{aligned} |\bar{K}N\rangle_{I=1,I_3=0} &= \frac{1}{\sqrt{2}}\left[|\bar{K}^0 n\rangle - |K^- p\rangle\right] \\ |K\Xi\rangle_{I=1,I_3=0} &= \frac{1}{\sqrt{2}}\left[|K^0\Xi^0\rangle - |K^+\Xi^-\rangle\right], \end{aligned} \tag{2.15}$$

we can write:

$$\langle K^+\Xi^0|T|K_L^0 p\rangle = -\frac{1}{2\sqrt{2}}\big[\langle K^0\Xi^0|T|\bar{K}^0 n\rangle - \langle K^0\Xi^0|T|K^- p\rangle \\ -\langle K^+\Xi^-|T|\bar{K}^0 n\rangle + \langle K^+\Xi^-|T|K^- p\rangle\big]. \tag{2.16}$$

Since there are no experimental data for this reaction, we can only make predictions employing our different models with the aim of comparing with the results of the future JLab experiment, when they become available. However, one already has information on the $\bar{K}N \to K\Xi$ reactions in $I = 1$. There are two data points for the $K^- n \to K^0\Xi^-$ cross section, obtained indirectly from the K^- deuteron reactions on bubble chamber experiments [95, 96]. Again, we can establish the relationship between the $K^- n \to K^0\Xi^-$ and $K_L^0 p \to K^+\Xi^0$ reactions. Departing from the isospin states ($|I\, I_3\rangle$) of the hadrons involved in this reaction:

$$|K^-\rangle = -|\frac{1}{2}\ -\frac{1}{2}\rangle,\ |n\rangle = |\frac{1}{2}\ -\frac{1}{2}\rangle \to \ \ |K^- n\rangle = -|1\ -1\rangle \\ |K^0\rangle = |\frac{1}{2}\ -\frac{1}{2}\rangle,\ |\Xi^-\rangle = |\frac{1}{2}\ -\frac{1}{2}\rangle \to \ \ |K^0\Xi^-\rangle = |1\ -1\rangle, \tag{2.17}$$

and, considering the invariance of the strong interaction under I_3 rotations, the $K^- n \to K^0\Xi^-$ scattering amplitude can be related to those in the $|I = 1,\ I_3 = 0\rangle$ sector (see eqs. (2.15)), as

$$\langle K^0\Xi^-|T|K^- n\rangle = -\frac{1}{2}\big[\langle K^0\Xi^0|T|\bar{K}^0 n\rangle - \langle K^0\Xi^0|T|K^- p\rangle \\ -\langle K^+\Xi^-|T|\bar{K}^0 n\rangle + \langle K^+\Xi^-|T|K^- p\rangle\big] = \sqrt{2}\langle K^+\Xi^0|T|K_L^0 p\rangle, \tag{2.18}$$

we have used eq. (2.16) in the last step to finally stablish the relationship between the

total cross sections:

$$\begin{aligned} \sigma_{K^- n \to K^0 \Xi^-} &\propto |\langle K^0 \Xi^- | T | K^- n \rangle|^2 = 2 |\langle K^+ \Xi^0 | T | K^0_L p \rangle|^2 \\ \sigma_{K^0_L p \to K^+ \Xi^0} &= \frac{1}{2} \sigma_{K^- n \to K^0 \Xi^-}. \end{aligned} \tag{2.19}$$

Our predictions of this reaction for the **WT+NLO**, **WT+NLO+Born (η chan)** and **WT+NLO+Born** models are shown in Fig. 2.8, together with the experimental points of the pure $I = 1$ $K^- n \to K^0 \Xi^-$ reaction, which have been divided by 2 to properly account for the size of the strangeness $S = -1$ component of the K^0_L (see eq. (2.19)). We would like to remind the reader that these two data points have not been used in none of the performed fitting procedure.

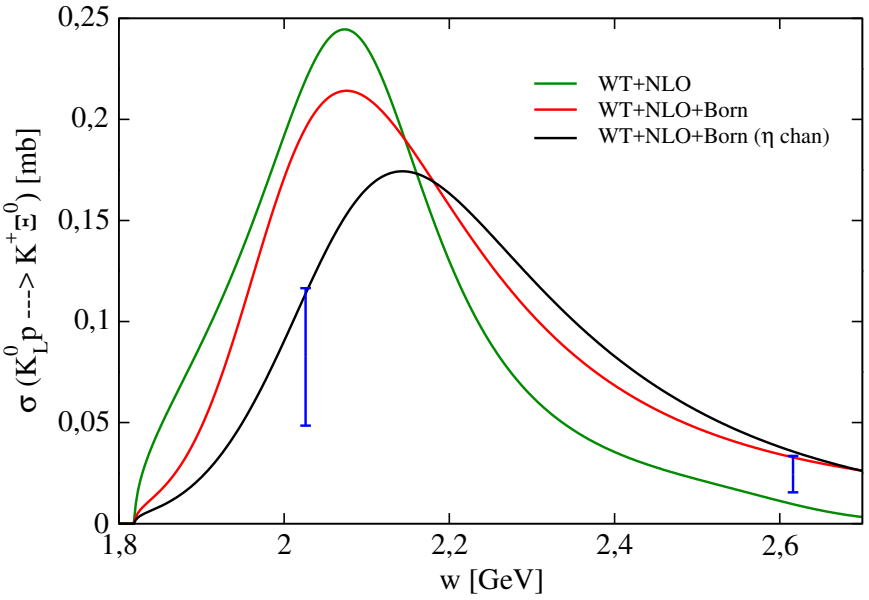

Figure 2.8: Total cross sections of the $K^0_L p \to K^+ \Xi^0$ reactions for the for the **WT+NLO** fit (green line), the **WT+NLO+Born** fit (red line) and the **WT+NLO+Born (η chan)** fit (black line), and the experimental points of the $I = 1$ $K^- n \to K^0 \Xi^-$ reaction, taken from [95, 96] and divided by two, see text for more details.

As one can see from Fig. 2.8, the **WT+NLO+Born (η chan)** fit (black line) and the **WT+NLO+Born** one (red line) do a good job at higher energy, while **WT+NLO** fit (green line) takes less than half the value of the experimental point located there. This is not the case for the point around 2 GeV where the models **WT+NLO** and **WT+NLO+Born** overshoot the corresponding value of the cross section by a factor of 2. But, on the other hand, **WT+NLO+Born (η chan)** reaches its maximum 50 MeV above the energy where the other two models do and, hence, favouring the agreement with the experimental point located at 2 GeV.

The general interpretation we can give to these predictions is that as more contributions in its interaction kernel are taken into account and more data is included in the fit, especially data from isospin filtering processes, the results from the theoretical models get closer and closer to the two available experimental points. Given these results, everything seems to indicate that having more data from the proposed secondary K_L^0 beam at Jlab would be very helpful to constrain the theoretical models.

Chapter 3

The inclusion of resonances

In Sect 2.3, we suggest the possibility to improve the description of data by implementing, in the $K\Xi$ channels, the contribution of the $\Lambda(1890)$ resonance, since the **WT+NLO+Born (η chan)** model does not properly reproduce the scattering data at low energies for the $K^-p \to K^0\Xi^0$ reaction (see Fig. 2.7). This could also be extended to the $K^-p \to \eta\Lambda$ process and, therefore, we could gain the strength needed to accommodate the theoretical cross section to the experimental data at energies close to this resonance. But, apart from this phenomenological reason, another important motivation to incorporate resonances, particularly into the $K\Xi$ channels, is that they allow us to study the accuracy and stability of the NLO coefficients. It is worthwhile to remind the reader that the sensitivity of the $K^-p \to K\Xi$ to the NLO terms has been proved along the present study, as well as that the authors of [21] also observed a sensibility to the NLO terms in the $K^-p \to \eta\Lambda$ process. Moreover, the inclusion of these resonant terms implicitly simulates higher angular momentum contributions involving low lying meson-baryon states of the coupled channel problem. In princi-

ple, it is expected that the more relevant the higher-angular-momenta terms are, the further the low energy constants will be from their "effective nominal values"[1] in the absence of such contributions. This is due to the fact that the low energy constants absorb these contributions in order to reproduce the experimental data at the expense of taking realistic values. Thus, the resonant contributions permit the parameters of the model to get relaxed, avoiding a possible overestimation of their values.

3.1 $\Sigma(2030)$ and $\Sigma(2250)$ resonances

Before proceeding to the incorporation of resonances to a model which is based on an interaction kernel that takes into account the WT, Born and NLO terms , we would like to discuss first the insights we found in our pioneering work on this issue [27], from which we gained expertise and from which the positive effects of the inclusion of resonances were seen. In this work we studied the phenomenological inclusion of high spin and high mass resonances into a model whose interaction kernel consist of WT and NLO contributions.

To put the reader in context, we should focus on the cross sections of Fig. 2.2 from which we observe that the discrepancies between the **WT+NLO** model (solid line) and the data are larger in the vicinity of 2 GeV and around 2.2 GeV. Therefore, an extra contribution to the cross section would be very welcome. The inclusion of the resonant terms was motivated by previous phenomenological models studying Ξ production [30–32,97,98], which indicate the need to take into consideration the $\bar{K}N \to Y \to K\Xi$ transition amplitudes, where Y stands for some high spin resonance coupling

[1] We employ the terminology "effective nominal values" because we should bear in mind that we are unitarizing the amplitudes. For more details, see discussion at the end of Sect. 1.2.2.

Resonance	I (J^P)	Mass (MeV)	Γ (MeV)	$\Gamma_{K\Xi}/\Gamma$
$\Lambda(1890)$	$0\left(\frac{3}{2}^+\right)$	1850 - 1910	60 - 200	
$\Lambda(2100)$	$0\left(\frac{7}{2}^-\right)$	2090 - 2110	100 - 250	$< 3\%$
$\Lambda(2110)$	$0\left(\frac{5}{2}^+\right)$	2090 - 2140	150 - 250	
$\Lambda(2350)$	$0\left(\frac{9}{2}^+\right)$	2340 - 2370	100 - 250	
$\Sigma(1915)$	$1\left(\frac{5}{2}^+\right)$	1900 - 1935	80 - 160	
$\Sigma(1940)$	$1\left(\frac{3}{2}^-\right)$	1900 - 1950	150 - 300	
$\Sigma(2030)$	$1\left(\frac{7}{2}^+\right)$	2025 - 2040	150 - 200	$< 2\%$
$\Sigma(2250)$	$1\left(?^?\right)$	2210 - 2280	60 - 150	

Table 3.1: Properties of the three- and four-star hyperon resonances in the mass range $1.89 < M < 2.35$ GeV taken from the results of the PDG review [99].

significantly to the $\bar{K}N$, $K\Xi$ channels.

In the energy range of interest, the PDG compilation [99] gives eight resonances with three- and four-star status with masses lying in the range $1.89 < M < 2.35$ GeV, see Table 3.1. Unfortunately, explicit branching ratios to $K\Xi$ decay have not been determined and only upper limits are given for two of these resonances: $< 3\%$ for the $\Lambda(2100)$ and $< 2\%$ for $\Sigma(2030)$. Thus, it is interesting to investigate the role of these above-threshold resonances. Note that most of these resonances have high spins, and therefore require a special treatment, analogous to that performed in [30–32].

Inspecting the resonance properties shown in Table 3.1 and the results of the NLO fit presented in Fig. 2.2, the $\Sigma(2030)$ and $\Sigma(2250)$ resonances seem to be good candidates to be implemented in our model. The two selected candidates also coincide with the findings of Ref [32], where it was concluded that these two resonances gave the best account of data, after various combinations of several resonances from the eight known

ones that were examined. The spin and parity $J^\pi = 7/2^+$ of the $\Sigma(2030)$ are well established. Those of the $\Sigma(2250)$ are not known, but the most probable assignments are $5/2^-$ or $9/2^-$ [99]. We choose $J^\pi = 5/2^-$ to simplify the calculations, noting also that the $9/2^-$ choice does not change the results drastically as has been shown in [32]. In this first stage, we also explored the possibility of including the $\Lambda(1890)$ resonance in our model which did not offer a better data reproduction and we gained nothing in terms of the NLO-coefficients accuracy. This is in contrast with the study performed in [85] where this last resonance came out to be relevant for the description of the existing Ξ production data.

Before continuing, I would like to give a brief explanation of the models employed in the two works, [32,85] , which I shall quote from now on during the chapter. In [32], the authors use a phenomenological model of s- and u-channel diagrams exchanging, below the $K\Xi$ threshold, Λ and Σ ground states, $\Sigma(1385)$ and $\Lambda(1520)$ resonances. Above the $K\Xi$ threshold, only the s-channel diagram was considered, exchanging the high-spin and high-mass $\Sigma(2030)$ and $\Sigma(2250)$ hyperonic resonances. There was demonstrated that the feasibility of such a model for describing the $\bar{K}N \to K\Xi$ reactions considering just the subthreshold exchanged particles is limited, and a good quantitative agreement with experimental data needs the mentioned extension to hyperonic resonances above threshold.

On the other hand, the authors of [85] studied the same reactions through an effective lagrangian approach that includes, in a similar fashion as [32], the hyperonic s- and u-channels as well as a phenomenological amplitude which accounts for the rescattering term in the scattering equation, and the possible short-range dynamics was not included explicitly in the model. We stress the point that the u-

channel is employed above and below threshold and that a slightly different resonance set was found as the relevant one to reproduce the experimental data, consisting of: $\Lambda, \Sigma, \Sigma(1385), \Lambda(1890), \Sigma(2030), \Sigma(2250)(J^\pi = 5/2^-)$. Another relevant difference between [32] and [85] is the employed form factors, an exponential form in [32] and a lorentzian form in [85], which leave the corresponding cutoff parameters differing by a factor 2, namely 440 MeV and 900 MeV respectively.

3.1.1 Formalism

The $\bar{K}N \to K^+\Xi^-$, $K^0\Xi^0$ reaction cross sections are obtained adding to the corresponding chiral unitary model amplitude $T(s', s)$ described in the previous chapter, the contributions from the $\bar{K}N \to \Sigma(2030) \to K\Xi$ and $\bar{K}N \to \Sigma(2250) \to K\Xi$ transitions, denoted by $T^{7/2^+}(s', s)$ and $T^{5/2^-}(s', s)$ respectively, which are built as described below.

Adopting the Rarita-Schwinger method, as in [31], the spin-5/2 and 7/2 baryon fields are described by a rank-2 tensor $Y^{\mu\nu}_{5/2}$ and a rank-3 tensor $Y^{\mu\nu\alpha}_{7/2}$, respectively. For future convenience we also include the corresponding method for the spin-3/2 which comes as a rank-1 tensor, and which allows one to implement the $\bar{K}N \to \Lambda(1890) \to K\Xi$ transition with a related $T^{3/2^-}(s', s)$ resonant amplitude. The lagrangians are

$$\mathcal{L}^{3/2^\pm}_{BYK}(q) = \mathrm{i}\frac{g_{BY_{3/2}K}}{m_K}\bar{B}\Gamma^{(\pm)}Y^{\mu}_{3/2}\partial_\mu K + H.c.\ , \tag{3.1}$$

for the spin-3/2 resonance,

$$\mathcal{L}^{5/2^\pm}_{BYK}(q) = \mathrm{i}\frac{g_{BY_{5/2}K}}{m_K^2}\bar{B}\Gamma^{(\pm)}Y^{\mu\nu}_{5/2}\partial_\mu\partial_\nu K + H.c.\ , \tag{3.2}$$

for the spin-5/2 resonance and

$$\mathcal{L}^{7/2^{\pm}}_{BYK}(q) = -\frac{g_{BY_{7/2}K}}{m_K^3}\bar{B}\Gamma^{(\mp)}Y^{\mu\nu\alpha}_{7/2}\partial_\mu\partial_\nu\partial_\alpha K + H.c.\ , \tag{3.3}$$

for the spin-7/2 one, where $\Gamma^{(\pm)} = \begin{pmatrix}\gamma_5\\ 1\end{pmatrix}$ depending on the parity of the resonance being studied, and g_{BY_JK} stands for the baryon-kaon-Y_J coupling. Then the corresponding propagators are given by [31]:

$$S_{3/2}(q) = \frac{\mathrm{i}}{\not{q} - M_{Y_{3/2}} + \mathrm{i}\Gamma_{3/2}/2}\Delta^{\beta_1\beta_2}, \tag{3.4}$$

$$S_{5/2}(q) = \frac{\mathrm{i}}{\not{q} - M_{Y_{5/2}} + \mathrm{i}\Gamma_{5/2}/2}\Delta^{\beta_1\beta_2}_{\alpha_1\alpha_2}, \tag{3.5}$$

$$S_{7/2}(q) = \frac{\mathrm{i}}{\not{q} - M_{Y_{7/2}} + \mathrm{i}\Gamma_{7/2}/2}\Delta^{\beta_1\beta_2\beta_3}_{\alpha_1\alpha_2\alpha_3}, \tag{3.6}$$

where we have included the mass M_J and the decay width, Γ_J, of the corresponding resonance. The tensors Δ are defined as:

$$\Delta^{\beta_1\beta_2}\left(\frac{3}{2}\right) = -g^{\beta_1\beta_2} + \frac{1}{3}\gamma^{\beta_2}\gamma^{\beta_2} + \frac{2p^{\beta_1}p^{\beta_2}}{3M^2_{\frac{3}{2}}} + \frac{\gamma^{\beta_1}p^{\beta_2} - p^{\beta_1}\gamma^{\beta_2}}{3M_{\frac{3}{2}}}, \tag{3.7}$$

$$\begin{aligned}\Delta^{\beta_1\beta_2}_{\alpha_1\alpha_2}\left(\frac{5}{2}\right) &= \frac{1}{2}\left(\theta^{\beta_1}_{\alpha_1}\theta^{\beta_2}_{\alpha_2} + \theta^{\beta_2}_{\alpha_1}\theta^{\beta_1}_{\alpha_2}\right) - \frac{1}{5}\theta_{\alpha_1\alpha_2}\theta^{\beta_1\beta_2}\\ &+ \frac{1}{10}\Big(\bar{\gamma}_{\alpha_1}\bar{\gamma}^{\beta_1}\theta^{\beta_2}_{\alpha_2} + \bar{\gamma}_{\alpha_1}\bar{\gamma}^{\beta_2}\theta^{\beta_1}_{\alpha_2}\\ &+ \bar{\gamma}_{\alpha_2}\bar{\gamma}^{\beta_1}\theta^{\beta_2}_{\alpha_1} + \bar{\gamma}_{\alpha_2}\bar{\gamma}^{\beta_2}\theta^{\beta_1}_{\alpha_1}\Big),\end{aligned} \tag{3.8}$$

$$\begin{aligned}\Delta^{\beta_1\beta_2\beta_3}_{\alpha_1\alpha_2\alpha_3}\left(\frac{7}{2}\right) &= \frac{1}{36}\sum_{P(\alpha)P(\beta)}\Big(\theta^{\beta_1}_{\alpha_1}\theta^{\beta_2}_{\alpha_2}\theta^{\beta_3}_{\alpha_3} \\ &- \frac{3}{7}\,\theta^{\beta_1}_{\alpha_1}\theta_{\alpha_2\alpha_3}\theta^{\beta_2\beta_3} \\ &- \frac{3}{7}\,\bar{\gamma}_{\alpha_1}\bar{\gamma}^{\beta_1}\theta^{\beta_2}_{\alpha_2}\theta^{\beta_3}_{\alpha_3} \\ &+ \frac{3}{35}\,\bar{\gamma}_{\alpha_1}\bar{\gamma}^{\beta_1}\theta_{\alpha_2\alpha_3}\theta^{\beta_2\beta_3}\Big),\end{aligned} \tag{3.9}$$

being $\theta^{\nu}_{\mu} = g^{\nu}_{\mu} - q_\mu q^\nu/M_Y^2$ and $\bar{\gamma}_\mu = \gamma_\mu - q_\mu \not{q}/M_Y^2$. The tensor Δ for the spin-7/2 field, given in Eq. (3.9), contains a summation over all possible permutations of Dirac indexes $\{\alpha_1\alpha_2\alpha_3\}$ and $\{\beta_1\beta_2\beta_3\}$.

From the Lagrangians of Eqs. (3.1), (3.2) and (3.3) one derives the baryon-kaon-Y_J vertices:

$$v^{3/2^\pm}_{BYK} = -\mathrm{i}\frac{g_{BY_{3/2}K}}{m_K}k_\mu\Gamma^{(\pm)}, \tag{3.10}$$

$$v^{5/2^\pm}_{BYK} = \mathrm{i}\frac{g_{BY_{5/2}K}}{m_K^2}k_\mu k_\nu\Gamma^{(\pm)}, \tag{3.11}$$

$$v^{7/2^\pm}_{BYK} = -\frac{g_{BY_{7/2}K}}{m_K^3}k_\mu k_\nu k_\sigma\Gamma^{(\mp)}. \tag{3.12}$$

The resonant contributions to the $\bar{K}N \to K\Xi$ scattering amplitudes can then be obtained straightforwardly as:

$$T^{3/2^+}_{\bar{K}N\to K\Xi}(s',s) = F_{3/2}(k,k')\,\bar{u}^{s'}_{\Xi}(p')\gamma_5 k'_{\beta_1}S_{3/2}(q)k_{\beta_2}\gamma_5 u^s_N(p)\ , \tag{3.13}$$

$$T^{5/2^-}_{\bar{K}N\to K\Xi}(s',s) = F_{5/2}(k,k')\,\bar{u}^{s'}_{\Xi}(p')k'_{\beta_1}k'_{\beta_2}S_{5/2}(q)k^{\alpha_1}k^{\alpha_2}u^s_N(p)\ , \tag{3.14}$$

and

$$T^{7/2^+}_{\bar{K}N\to K\Xi}(s',s) = F_{7/2}(k,k')\,\bar{u}^{s'}_{\Xi}(p')k'_{\beta_1}k'_{\beta_2}k'_{\beta_2}S_{7/2}(q)k^{\alpha_1}k^{\alpha_2}k^{\alpha_3}u^s_N(p)\ , \tag{3.15}$$

here u_X^s stands for the spinor structure of a baryon with spin s and where we have included a form factor:

$$F_J(k,k') = \frac{g_{\Xi Y_J K}\, g_{N Y_J \bar{K}}}{m_K^{2J-1}} \exp\left(-\vec{k}^2/\Lambda_J^2\right) \exp\left(-\vec{k'}^2/\Lambda_J^2\right) \ , \tag{3.16}$$

which inserts a phenomenological exponential function, $\exp\left(-\vec{q}^{\,2}/\Lambda_J^2\right)$, in each vertex to suppress high powers of the meson momentum from the vertex contributions, as it was done in [32]. Strictly speaking the exponential factors in Eq. (3.16) are not genuine form factors, since these should depend on the off-shell momentum of the off-shell particle and should be normalized to 1 at the on-shell point. The "form factor" in eq. (3.16) is just an ad-hoc function introduced to modify the energy dependence of the resonance contribution. This prescription, however, is used in the resonance based model of [32], which inspired us to complement our study with the inclusion of resonances. So, we have decided to employ it for a more direct comparison with the above cited paper. Furthermore, in Ref. [32] the authors have studied different forms of form factor, and they claim that the $\exp\left(-\vec{q}^{\,2}/\Lambda_J^2\right)$ form gives the best $\chi^2_{\text{d.o.f.}}$ result. In order to verify this statement we have also tried form factors depending on the four momentum squared of the off-shell resonance, either in the form $\exp\{-(k^2 - M_{Y_J}^2)/\Lambda_J^2\}$, which has the same asymptotic behaviour at high values of the meson tri-momentum $\vec{q}$, or via the function $\Lambda_J^4/[\Lambda_J^4 + (k^2 - M_{Y_J}^2)^2]$, employed in the more recent work of [85]. In the results sections we will discuss the consequences of the choice of form factor on the data fitting.

Finally, for the initial $K^- p$, $\bar{K}^0 n$ channels and final $K^+\Xi^-$, $K^0\Xi^0$ ones we use the

following prescription

$$\sqrt{4M_pM_\Xi}T_{ij}^{\rm tot}(s',s) = \sqrt{4M_pM_\Xi}T_{ij}(s',s)$$

$$+ T_{ij}^{5/2^-}(s',s) + T_{ij}^{7/2^+}(s',s) \ , \tag{3.17}$$

where the amplitudes $T_{ij}^R(s',s)$ contain the appropiate Clebsh-Gordan coefficients projecting the states i and j states into the isospin 1 of the $5/2^-$ and $7/2^+$ resonances included here. One can then proceed to derive the observables, following eqs. (2.2)-(2.8). We should remind the reader that at this stage we disregard the contribution of $\Lambda(1890)$ resonance since it barely contributes to a better data description for this model which is based on a WT+NLO interaction kernel, as we will see latter.

The chiral unitary model of the previous chapter is limited to s-wave interactions and, therefore, gives rise to flat differential cross sections. On the contrary, the high spin resonance mechanisms described in this section introduce an angular dependence in the amplitudes of the $K\Xi$ production channels, permitting a study of the differential cross sections for these channels, which are given by

$$\frac{d\sigma_{ij}}{d\Omega} = \frac{1}{64\pi^2}\frac{4M_iM_j}{s}\frac{k_j}{k_i}S_{ij}, \tag{3.18}$$

where S_{ij} is obtained from eq. (2.2), but employing the $T_{ij}^{\rm tot}$ instead of T_{ij} amplitude of eq. (3.17).

3.1.2 Fitting procedure and Data treatment III

Since the new high spin resonant terms produce angular dependent scattering amplitudes, we will consider, in addition to the total cross sections and threshold observables listed in Table 2.1, the differential cross sections of the $K^- p \to K\Xi$ reactions taken from the same sources [74–80]. More specifically, the fits in this section will include 2 new observables: the 235 differential cross section points from the $K^+\Xi^-$ production reaction and 76 differential cross section points from the $K^0\Xi^0$ one. Thus, we increase the total number of experimental points to 477 instead of the 166 employed in the fits of Sect. 2.1.2. With the aim of preserving the same weight for each observable, the same definition of the $\chi^2_{\rm d.o.f.}$, eq. (2.10), is employed. However, in the new fit the overall weight of the $K\Xi$ channels is larger, since there are two new observables related to these.

It must be also mentioned that large amount of new points, more dispersed, could rise the contribution to $\chi^2_{\rm d.o.f.}$, but, as we will see, we gain in having a better overall description of the $K^- p \to K\Xi$ reactions while fully respecting an acceptable accuracy for the other observables.

We will present results for three different fits:

i) A fit denoted by **NLO***, which employs the NLO interaction kernel without any additional resonance contribution. Thus, this fit is completely analogous to the **WT+NLO** fit from the previous chapter, and correspondingly the resulting curves for the **NLO*** differential cross sections of the $K^- p \to K\Xi$ reactions will be flat, without any angular dependence. However taking into account the new experimental points of the differential cross sections we give a larger weight to the $K\Xi$ channels, as discussed

above, therefore we expect a slight modification of the model parameters with respect to the **WT+NLO** fit from the previous section. We would like to remind that there are 14 free parameters involved in the **NLO*** fit: the pion decay constant f, the six subtraction constants, and the seven low energy constants of the NLO Lagrangian.

ii) Another fit, denoted by **WT+RES**, which employs the lowest order kernel of the chiral Lagrangian and adds the resonant terms described in this section. This fit has 15 free parameters: the same seven parameters as those for the lowest order fits of the previous chapter (f and the 6 subtraction constants) plus eight new parameters associated to the resonant terms, namely masses and widths of the resonances ($M_{Y_{5/2}}$, $M_{Y_{7/2}}$, $\Gamma_{5/2}$ and $\Gamma_{7/2}$), the product of couplings ($g_{\Xi Y_{5/2}K} \cdot g_{NY_{5/2}\bar{K}}$ and $g_{\Xi Y_{7/2}K} \cdot g_{NY_{7/2}\bar{K}}$) and the cut-off in the form factors ($\Lambda_{5/2}$ and $\Lambda_{7/2}$). This fit aims at exploring whether the background terms could be accounted only through the lowest order chiral Lagrangian, while the $K\Xi$ channels can be covered by the resonant terms.

iii) Finally, a fit denoted by **NLO+RES**, which incorporates the NLO interaction kernel together with the high spin resonance contributions in the $K^- p \to K^+\Xi^-$, $K^0\Xi^0$ channels. This fit determines 22 free parameters: the same fourteen as in the **NLO*** fit and the new eight parameters associated to the resonant terms. This is the most complete calculation that, upon comparison with the results of the previous **WT+RES** fit, will assess the actual role of the NLO terms in the chiral Lagrangian and will determine the value of their low energy constants.

We note that not all parameters are fully free. We constrain masses and widths of the resonances to lie within the ranges given in the PDG compilation [99] (see table 3.1) and the form-factor cut-off values are constrained in the range 500 MeV$< \Lambda_J <$ 1000 MeV.

3.1.3 Results and discussion III

	γ	R_n	R_c	$a_p(K^-p \to K^-p)$	ΔE_{1s}	Γ_{1s}
NLO*	2.37	0.189	0.664	$-0.69 + \mathrm{i}\,0.86$	300	570
WT+RES	2.37	0.193	0.667	$-0.73 + \mathrm{i}\,0.81$	307	528
NLO+RES	2.39	0.187	0.668	$-0.66 + \mathrm{i}\,0.84$	286	562
Exp.	2.36	0.189	0.664	$-0.66 + \mathrm{i}\,0.81$	283	541
	± 0.04	± 0.015	± 0.011	$(\pm 0.07) + \mathrm{i}\,(\pm 0.15)$	± 36	± 92

Table 3.2: Threshold observables obtained from the NLO*, WT+RES and NLO+RES fits explained in the text. Experimental data is taken from [18, 81, 82].

In this section we discuss the results of the fits described above which have also included the differential $K^-p \to K\Xi$ cross sections in the fitting procedure. The results for the threshold observables shown in Table 3.2 indicate that, even if the fits now adjust new data at higher energies and may contain the additional effect of resonant terms, as in the case of **WT+RES** and **NLO+RES**, the low energy data keeps being very well described. A similar situation is found when inspecting the cross sections obtained from the three fits for the $K^-p \to K^-p$, $\bar{K}^0 n, \pi^-\Sigma^+, \pi^+\Sigma^-, \pi^0\Sigma^0, \pi^0\Lambda$ reactions shown in Fig. 3.1.

Obviously, the differences between these fits are more evident in the total and differential cross sections of the $K\Xi$ production channels shown in Figs. 3.2, 3.4 and 3.3. First we note that the total cross sections for $K\Xi$ production obtained from the **NLO*** fit (dashed lines in Fig. 3.2) are in reasonable agreement with the data, even if the resonant terms are not included. As it was discussed above, this **NLO*** fit is very similar to the **WT+NLO** one of the previous section, but it also tries to accommodate the differential $K\Xi$ production cross section data, which can only be

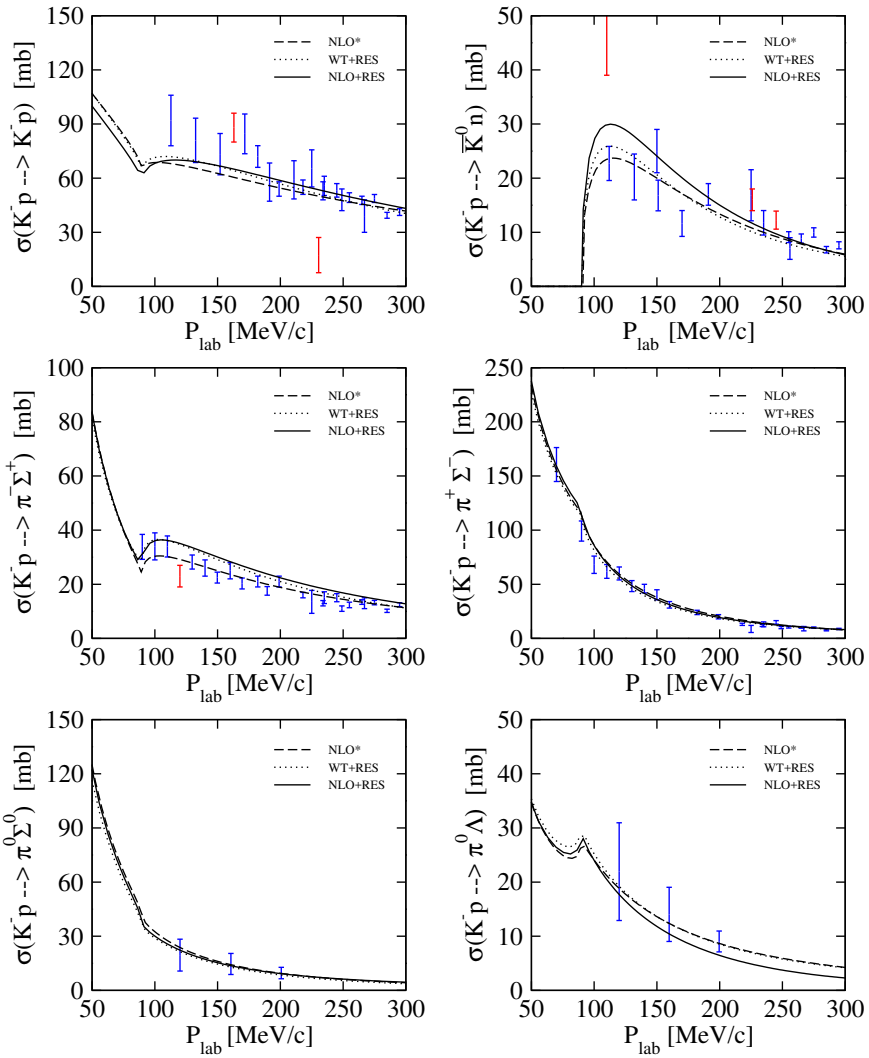

Figure 3.1: Total cross sections of the $K^- p \to K^- p, \bar{K}^0 n, \pi^- \Sigma^+, \pi^+ \Sigma^-, \pi^0 \Sigma^0, \pi^0 \Lambda$ reactions for the **NLO*** fit (dashed line), the **WT+RES** fit (dotted line) and the **NLO+RES** fit (solid line). Experimental data are from [70–73]. The points in red have not been included in the fitting procedure.

adjusted on average, as shown by the dashed lines in Figs. 3.3 and 3.4, because of the flat distribution characteristic of s-wave models.

In order to account for some structure in the differential $K\Xi$ production cross sections we need to implement the resonant terms. When they are added to the unitarized

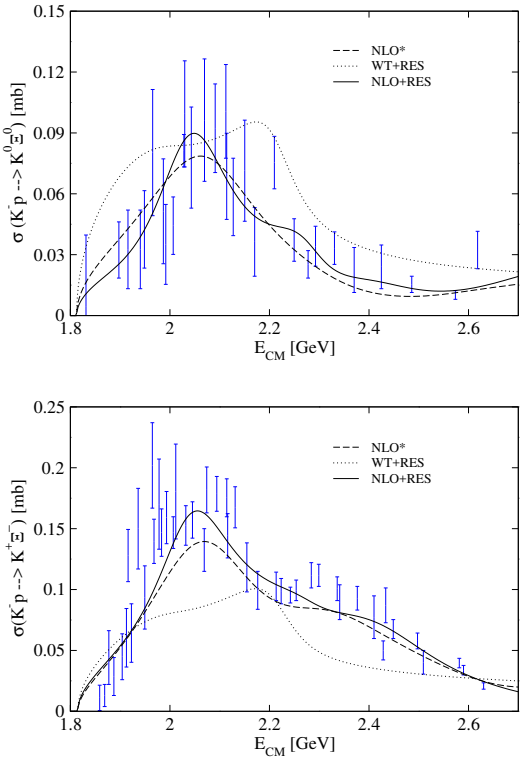

Figure 3.2: Total cross sections of the $K^- p \to K^0\Xi^0, K^+\Xi^-$ reactions for the **NLO*** fit (dashed line), the **WT+RES** fit (dotted line) and the **NLO+RES** fit (solid line), see the text for more details. Experimental data are from [74–80].

amplitudes obtained from the lowest order chiral Lagrangian (only WT term), one finds the results denoted by the dotted lines, i. e. **WT+RES** fit, in Figs. 3.2, 3.3 and 3.4. It is clear that, although some structure is gained in the differential cross sections and, hence, their description improves substantially than in the absence of resonances, the total $K\Xi$ production cross sections are poorly reproduced by the **WT+RES** fit. In other words, the background terms encoded in the lowest order chiral Lagrangian, which only contribute via unitarization, are insufficient to account for the whole set of $K\Xi$ production data satisfactorily. This situation is remedied when the chiral Lagrangian is taken at NLO. In this case, one finds a clear overall improvement in the description of the data. The solid lines in Figs. 3.2, 3.3 and 3.4 clearly demonstrate

that the **NLO+RES** fit reproduces satisfactorily the $K\Xi$ total cross sections, while accounting quite reasonably for the differential ones. Our model fails especially at backward angles for the higher K^- energies. Obviously, including additional hyperon resonances in s- and u-channel configurations could improve these deficiencies.

It is also worth mentioning that the inclusion of the high-spin resonances in the fit is very time consuming: the calculations are prolonged by factor 100, from several hours to several weeks.

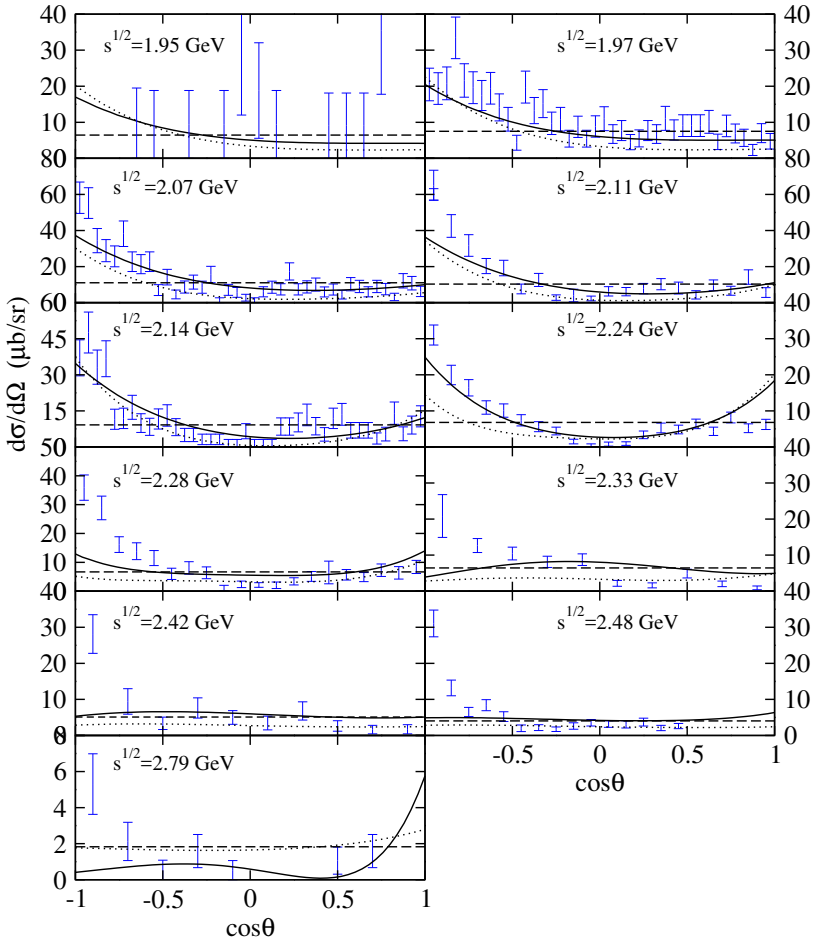

Figure 3.3: Differential cross section of the $K^-p \to K^+\Xi^-$ reaction for the NLO* fit (dashed line), the WT+RES fit (dotted line) and the NLO+RES fit (solid line), see the text for more details. Experimental data are from [74–80].

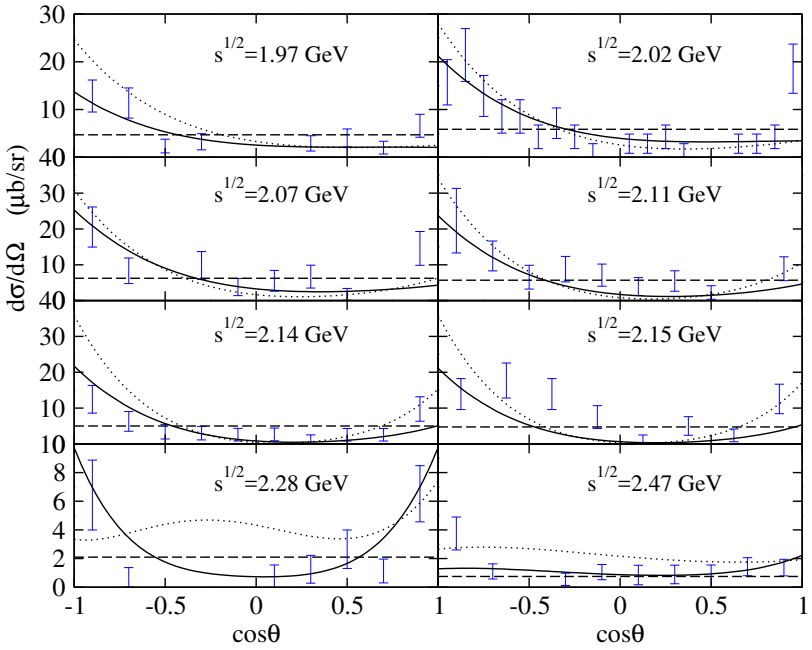

Figure 3.4: Differential cross section of the $K^- p \to K^0 \Xi^0$ reaction for the NLO* fit (dashed line), the WT+RES fit (dotted line) and the NLO+RES fit (solid line), see the text for more details. Experimental data are from [74–80].

One can judge the goodness of the fits discussed in this section by inspecting the obtained $\chi^2_{\text{d.o.f.}}$, shown in Table 3.3 together with the values of the fitted parameters. The first observation that we can make is that, even if the **NLO*** fit shows a similar quality as the **WT+NLO** fit of the previous chapter in reproducing the cross section data, it has twice its $\chi^2_{\text{d.o.f.}}$ value. This is due to the additional differential cross section data employed in the **NLO*** fit, which can only be reproduced on average, leaving the predictions quite far away from the experimental points in some cases. Also we can see that the parameters of these two fits are rather similar.

It is interesting to point out that, although the resonant terms naturally improve the description of the $K\Xi$ differential cross section data, when the chiral Lagrangian is kept up to the lowest order, then the corresponding **WT+RES** $\chi^2_{\text{d.o.f.}}$ value increases

	NLO*	WT+RES	NLO+RES
$a_{\bar{K}N}$ (10^{-3})	6.799 ± 0.701	-1.965 ± 2.219	6.157 ± 0.090
$a_{\pi\Lambda}$ (10^{-3})	50.93 ± 9.18	-188.2 ± 131.7	59.10 ± 3.01
$a_{\pi\Sigma}$ (10^{-3})	-3.167 ± 1.978	0.228 ± 2.949	-1.172 ± 0.296
$a_{\eta\Lambda}$ (10^{-3})	-15.16 ± 12.32	1.608 ± 2.603	-6.987 ± 0.381
$a_{\eta\Sigma}$ (10^{-3})	-5.325 ± 0.111	208.9 ± 151.1	-5.791 ± 0.034
$a_{K\Xi}$ (10^{-3})	31.00 ± 9.441	43.04 ± 25.84	32.60 ± 11.65
f/f_π	1.197 ± 0.011	1.203 ± 0.023	1.193 ± 0.003
b_0 (GeV^{-1})	-1.158 ± 0.021	-	-0.907 ± 0.004
b_D (GeV^{-1})	0.082 ± 0.050	-	-0.151 ± 0.008
b_F (GeV^{-1})	0.294 ± 0.149	-	0.535 ± 0.047
d_1 (GeV^{-1})	-0.071 ± 0.069	-	-0.055 ± 0.055
d_2 (GeV^{-1})	0.634 ± 0.023	-	0.383 ± 0.014
d_3 (GeV^{-1})	2.819 ± 0.058	-	2.180 ± 0.011
d_4 (GeV^{-1})	-2.036 ± 0.035	-	-1.429 ± 0.006
$g_{\Xi Y_{5/2}K} \cdot g_{NY_{5/2}\bar{K}}$	-	-5.42 ± 15.96	8.82 ± 5.72
$g_{\Xi Y_{7/2}K} \cdot g_{NY_{7/2}\bar{K}}$	-	-0.61 ± 14.12	0.06 ± 0.20
$\Lambda_{5/2}$ (MeV)	-	576.7 ± 275.2	522.7 ± 43.8
$\Lambda_{7/2}$ (MeV)	-	623.7 ± 287.5	999.0 ± 288.0
$M_{Y_{5/2}}$ (MeV)	-	2210.0 ± 39.8	2278.8 ± 67.4
$M_{Y_{7/2}}$ (MeV)	-	2025.0 ± 9.4	2040.0 ± 9.4
$\Gamma_{5/2}$ (MeV)	-	150.0 ± 71.3	150.0 ± 54.4
$\Gamma_{7/2}$ (MeV)	-	200.0 ± 44.6	200.0 ± 32.3
$\chi^2_{\mathrm{d.o.f.}}$	1.48	2.26	1.05

Table 3.3: Values of the parameters and the corresponding $\chi^2_{\mathrm{d.o.f.}}$, defined as in eq. (2.10), for the different fits described in the text. The value of the pion decay constant is $f_\pi = 93$ MeV and the subtraction constants are taken at a regularization scale $\mu = 1$ GeV.

in about one unit with respect to the non-resonant **NLO*** fit. This just reflects the inability of the lowest order Lagrangian of producing enough strength, which we recall comes from unitarization, to interfere efficiently with that of the resonant terms. This

gives rise to a poor description of the $K\Xi$ total cross section data and, consequently, to an unreasonably large $\chi^2_{\rm d.o.f.}$ value. As in the previous chapter, the size of some of the subtraction constants of this fit turns out to be unphysically large. We then find again that the NLO terms of the chiral Lagrangian are essential to account for the $K\Xi$ data. This is reflected in a reduction of the corresponding **NLO+RES** $\chi^2_{\rm d.o.f.}$ value, which turns out to be of around one.

We have also performed fits with the two choices of form factor that depend on the off-shell four-momentum of the resonance and are normalized to 1 at the on-shell point, namely $\exp\{-(k^2 - M^2_{Y_J})/\Lambda^2_J\}$ and $\Lambda^4_J/[\Lambda^4_J + (k^2 - M^2_{Y_J})^2]$ (see discussion after Eq. (3.16)). We have found that the $\chi^2_{\rm d.o.f.}$ worsens, giving in both cases a value of 1.25 versus the 1.05 value obtained for the ad-hoc prescription, in complete agreement to the claims made in Ref. [32]. Interestingly, we find the corresponding NLO parameters not to change significantly and they remain quite similar to the **NLO+RES** ones shown in Table 3.3.

The important role of the $K\Xi$ channels in constraining the NLO terms of the chiral Lagrangian has already been shown in the previous chapter, where the corresponding low energy constants, obtained including the $K\Xi$ production total cross section data in the **WT+NLO** fit, changed appreciably with respect to those of the **WT+NLO (no** $K\Xi$**)** fit. In this section, we have seen how the description of data, which now includes the additional $K\Xi$ differential cross sections, is further improved when we supplement the NLO Lagrangian with the resonant terms. We observe that, although there is a slight readjustment of the parameters of the **NLO+RES** fit with respect to those of the **NLO*** fit, they have gained in precision significantly. This is due to the stabilizing role of the resonant terms, which implement an important part of the energy

dependencies, hence relegating the role of the NLO Lagrangian contribution to be a smooth background. This is in line with the contribution of the contact term introduced ad hoc in the resonant model of Ref. [85] to account for the strong Ξ production data. We would like to mention the (unexpected) stability of the pion decay width parameter f which stays around 1.195 in all the fits.

We also comment on the resonance parameters obtained by our **NLO+RES** fit. First of all, we would like to remind the reader that the masses and widths are constrained to lie within the experimentally measured bounds [99]. As we can see in Table 3.3 the product of couplings and the form factors are not very well constrained by the fit.

As mentioned already, we complemented our study with the inclusion of high spin hyperonic resonances being inspired by the work of [32], but we would like to point out that a direct comparion of the resonance parameters of our model with the those of [32] is not straightforward. This is also the case when comparing similar resonance based models. For instance, the resonance parameters obtained in [32] are quite different than those in [85][2], and the high-spin resonance contributions may differ by more than a factor of two in both resonance models. The reason is that the effect of these resonances depends very much on the interference with the background terms. Clearly, different backgrounds will result in rather different coupling sizes and even signs, as it was shown in [85]. However, the big advantage of our approach is that our "background terms" are completely determined by a theoretically supported chiral model.

Still, trying to compare our results with those of [32], where "form factors" of the

[2]For a proper comparison, note that the dimensionless couplings given in [85], as well as those of the present work, are given in units of the kaon mass, while those of [32] use the pion mass.

same type have been used, we observe that, while our value of $g_{\Xi Y_{5/2}K} \cdot g_{NY_{5/2}\bar{K}}$ turns to be comparable, although having an opposite sign, to that obtained in the resonant model of Ref. [32], the product $g_{\Xi Y_{7/2}K} \cdot g_{NY_{7/2}\bar{K}}$ is almost three orders of magnitude smaller. Note, however, that this has also to be viewed together with the effect of the form-factor, which in the present work is more moderate, since the cut-off values turn out to be larger, especially for the $7/2^+$ resonance, than the 440 MeV value employed in [32].

We have also tried to make a fit with 3 resonances, implementing an additional P-wave state in our model, lying close to the $K\Xi$ threshold. This could be for example the $\Lambda(1890)$ $3/2^+$ resonance, also included in [85]. However, we find that a resonance of this type does not improve substantially the quality of the fit, as can be seen from Fig. 3.5. The change of $\chi^2_{\text{d.o.f.}}$ from 1.05 to 1.04, while keeping the NLO parameters rather stable and similar to those quoted in Table 3.3, does not compensate, in our opinion, the increase of complexity of the problem and of the necessary computing time.

This fact can be understood by studying the isospin decomposition of the $K^-p \to K^0\Xi^0, K^+\Xi^-$ total cross section (see eqs. 2.12 in the second chapter) for the **NLO*** model which is represented in the left panels[3] of Fig. 3.6. If one pays attention on the left panels of this figure, which correspond to the isospin decomposition of the total cross section corresponding to $K^-p \to K^0\Xi^0, K^+\Xi^-$ reactions for the **NLO*** model, one observes that the $I = 0$ contribution peaks around 2.3 GeV taking a comparable strength to the $I = 1$ contribution at that energy while at lower energies the $I = 0$ contribution is practically negligible in front of the values taken by the $I = 1$

[3]The right panels will be discussed in the next section.

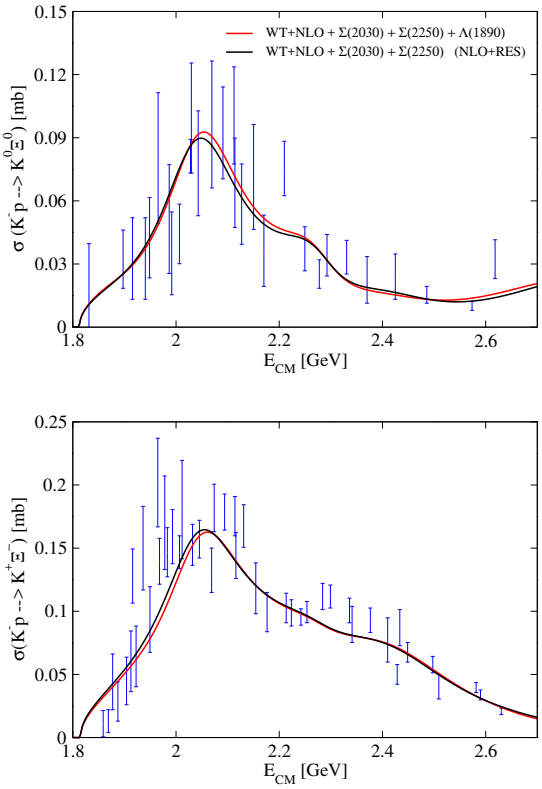

Figure 3.5: Total cross sections of the $K^-p \to K^0\Xi^0, K^+\Xi^-$ reactions for the **NLO+RES** fit (solid black line) and for the same model with the additional inclusion of a resonant $\Lambda(1890)$ contribution (solid red line), see the text for more details. Experimental data are from [74–80].

contribution, which accommodates rather well to the experimental data in this energy regime.

3.2 Full s-wave chiral model up to NLO with resonances

In this section, encouraged by our precedents in incorporating resonant contributions to a pure chiral model, we can address the inclusion of such contributions in our best chiral

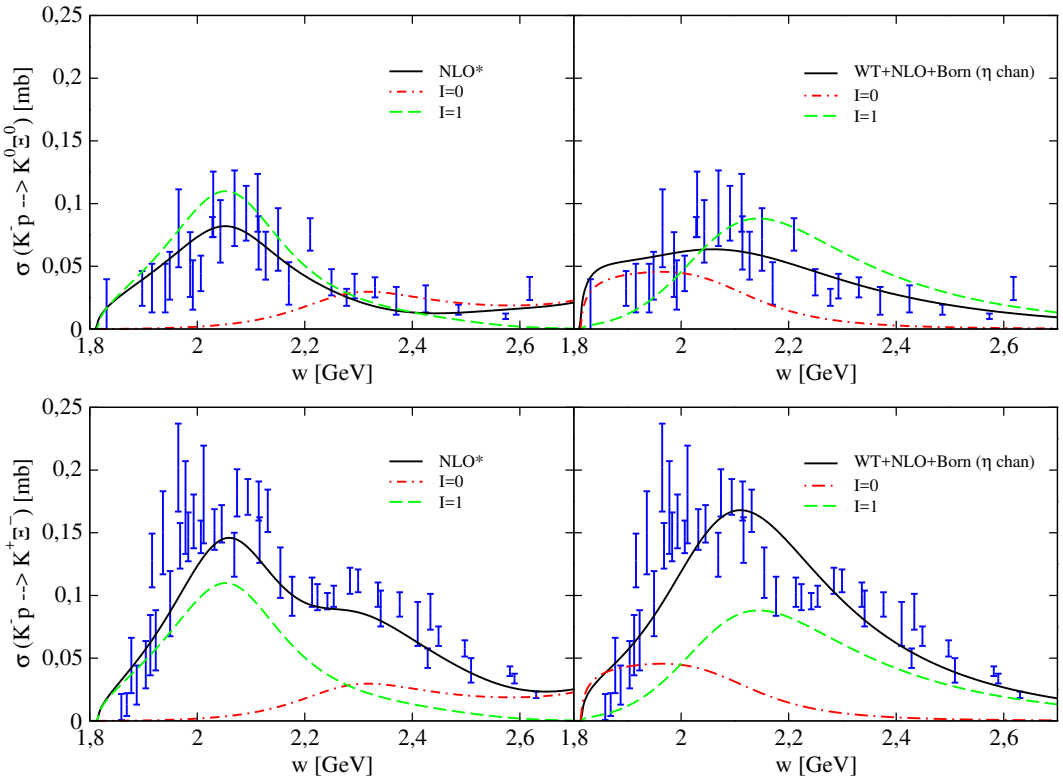

Figure 3.6: The total cross section data of the $K^-p \to K^0\Xi^0$ reaction is represented in the top panels, where the left figure corresponds to the **NLO*** model and the right one corresponds to the **WT+NLO+Born (η chan)** model. The same distribution for the bottom panels where the $K^-p \to K^+\Xi^-$ cross section data are represented. The figure shows the complete results by means of solid lines, the results where only isospin $I = 1$ component (dashed lines) or $I = 0$ one (dot-dashed line) have been retained.

model, namely the **WT+NLO+Born (η chan)** one. This model offers a reasonably good reproduction of the available experimental observables in the $S = -1$ sector, particularly, it is the first model based on a chiral lagrangian (in coupled channels) capable of reproducing the scattering data of K^-p to all possible channels. At the same time, it also provides a more realistic and accurate set of parameters. As it has been mentioned at the beginning of the chapter, the inclusion of the $\Lambda(1890)$ resonance could help in improving the $K^-p \to \eta\Lambda$ and the $K^-p \to K\Xi$ cross sections around 1900 MeV.

The effects of such incorporation for the $K^-p \to K\Xi$ case are expected to be appreciable since the $I = 0$ distribution of the $K^-p \to K\Xi$ cross section for the **WT+NLO+Born (η chan)** model, see right panels of Fig. 3.6, is concentrated very close to $K\Xi$ threshold which is in contrast to what we have seen for the models without the Born term. This distribution shows a plateau around 1900 MeV with a cross section about one third part of the maximum value to decrease later from 2000 MeV.

On the other hand, from right panels of Fig. 3.6, we observe that the distribution of the $I = 1$ component of the $K^-p \to K\Xi$ cross section produces a wide smooth bump which peaks around 2150 MeV. The inclusion of $\Sigma(2030)$ and $\Sigma(2250)$ resonant terms into the amplitude seem quite straightforward given the prominent cross section of the $I = 1$ component at such energies and the successful role of the inclusion of these resonances in our study of [27].

In summary, we are going to implement our chiral model by means of the inclusion of the $K^-p \to Y \to K\Xi$ and $K^-p \to X \to \eta\Lambda$ transition amplitudes where Y stands for the $\Lambda(1890)$, $\Sigma(2030)$ and $\Sigma(2250)$ resonances and X stands for the $\Lambda(1890)$ resonance. To carry out this, we use the same formalism described above, although we should first rewrite the scattering amplitudes with the suggested resonant contributions. Regarding $K^-p \to K^0\Xi^0, K^+\Xi^-$ processes, we need to replace eq. (3.17) with

$$\sqrt{4M_pM_\Xi}T_{ij}^{\rm tot}(s',s) = \sqrt{4M_pM_\Xi}T_{ij}(s',s) \, + \, T_{ij}^{3/2^+}(s',s)$$

$$+ T_{ij}^{5/2^-}(s',s) \, + \, T_{ij}^{7/2^+}(s',s) \; . \tag{3.19}$$

Analogously, for $K^-p \to \eta\Lambda$, we have

$$\sqrt{4M_pM_\Xi}T^{\rm tot}_{K^-p\to\eta\Lambda}(s',s) = \sqrt{4M_pM_\Xi}T_{K^-p\to\eta\Lambda}(s',s) \,+\, T^{3/2^+}_{K^-p\to\eta\Lambda}(s',s) \tag{3.20}$$

where the resonant amplitude is defined as

$$T^{3/2^+}_{K^-p\to\eta\Lambda}(s',s) = F_{3/2}(k,k')\,\bar{u}^{s'}_\Lambda(p')\gamma_5 k'_{\beta_1} S_{3/2}(q) k_{\beta_2}\gamma_5 u^s_N(p)\ . \tag{3.21}$$

3.2.1 Fitting procedure and Data treatment IV

Since we want to compare our new fit directly with **WT+NLO+Born (η chan)** model in order to study the effects of the resonant terms on the low energy constants, we consider the same amount of data that was used to perform this last one. One can find all these data displayed in Table 3.4. One notices that the $K^-p \to K\Xi$ differential cross section data are not taken into account, contrary to the case explored in Sect. 2.1.1. The main reason comes from the fact that, if one compares **WT+NLO** (Sect. 2.1.1) and **NLO*** (Sect. 3.1.2) models whose only difference is the inclusion or not of such points, they essentially give the same parametrization for the minimum. Moreover, the inclusion of these additional 349 points from the $K^-p \to K\Xi$ differential cross section increases considerably the calculation time.

In this section we will present results for the **WT+NLO+Born+RES** fit based on an unitarized calculation employing the chiral Lagrangian at NLO, that is, an interaction kernel which incorporates the contribution of the WT, the Born and the NLO terms, together with the high spin resonance contributions in the $K^-p \to K^+\Xi^-$, $K^0\Xi^0$, $\eta\Lambda$ channels in the way specified in the previous section. Technically speaking,

Observable	Points	Observable	Points
$\sigma_{K^-p\to K^-p}$	23	$\sigma_{K^-p\to\bar{K}^0n}$	9
$\sigma_{K^-p\to\pi^0\Lambda}$	3	$\sigma_{K^-p\to\pi^0\Sigma^0}$	3
$\sigma_{K^-p\to\pi^-\Sigma^+}$	20	$\sigma_{K^-p\to\pi^+\Sigma^-}$	28
$\sigma_{K^-p\to\eta\Sigma^0}$	9	$\sigma_{K^-p\to\eta\Lambda}$	49
$\sigma_{K^-p\to K^+\Xi^-}$	46	$\sigma_{K^-p\to K^0\Xi^0}$	29
γ	1	ΔE_{1s}	1
R_n	1	Γ_{1s}	1
R_c	1		

Table 3.4: Number of experimental points used in our fits, which are extracted from [18, 70–82, 86–89], distributed per observable.

the part coming from the chiral model involves the fitting of sixteen parameters: the pion decay constant f, the six subtraction constants $a_{\bar{K}N}$, $a_{\pi\Lambda}$, $a_{\pi\Sigma}$, $a_{\eta\Lambda}$, $a_{\eta\Sigma}$, and $a_{K\Xi}$, the axial vector couplings of the baryons to the mesons D, F and the NLO low energy constants b_0, b_D, b_F, d_1, d_2, d_3 and d_4. As in our previous models, which incorporate the Born diagrams, we decided to relax the axial vector couplings allowing them to lie in 12.5% of their canonical value, as was already explained in Sect. 2.2.1. With respect to the resonant part, we add 13 new parameters, namely: masses and widths of the resonances ($M_{Y_{3/2}}$, $M_{Y_{5/2}}$, $M_{Y_{7/2}}$, $\Gamma_{3/2}$, $\Gamma_{5/2}$ and $\Gamma_{7/2}$), the product of couplings ($g_{\Lambda Y_{3/2}\eta}\cdot g_{NY_{3/2}\bar{K}}$, $g_{\Xi Y_{3/2}K}\cdot g_{NY_{3/2}\bar{K}}$, $g_{\Xi Y_{5/2}K}\cdot g_{NY_{5/2}\bar{K}}$ and $g_{\Xi Y_{7/2}K}\cdot g_{NY_{7/2}\bar{K}}$) and the cut-off in the form factors ($\Lambda_{3/2}$, $\Lambda_{5/2}$ and $\Lambda_{7/2}$). The fitting parameters amounts to a total of 29, but we would like to remark that not all parameters are fully free. We constrain masses and widths of the resonances to lie within the ranges given in the PDG compilation [99] (see table 3.1) and the form-factor cut-off values are constrained in the range 500 MeV$< \Lambda_J <$ 1000 MeV.

3.2.2 Results and discussion IV

One of the motivations for carrying out this last fit was to study the implications of including resonant terms on the low energy constants. In order to establish a fair comparison, as we have mentioned, we constrained the **WT+NLO+Born+RES** fit to the same amount of experimental data as in the case of the **WT+NLO+Born (η chan)** fit. As has been happening in all our fits, the inclusion of data at higher energies has not affected the quality of the low energy observables. A clear proof of this is the good description of the low energy data which, here, is compiled in Table 3.5 and Fig. 3.7. The inclusion of resonances in the **WT+NLO+Born+RES** model improves slightly the overall agreement of the threshold observables, as we see in Table 3.5.

	γ	R_n	R_c	$a_p(K^-p \to K^-p)$	ΔE_{1s}	Γ_{1s}
WT+NLO+Born (η chan)	2.36	0.188	0.659	$-0.65 + \mathrm{i}\,0.88$	288	588
WT+NLO+Born+RES	2.36	0.189	0.661	$-0.64 + \mathrm{i}\,0.87$	283	587
Exp.	2.36 ± 0.04	0.189 ± 0.015	0.664 ± 0.011	$-0.66 + \mathrm{i}\,0.81$ $(\pm 0.07) + \mathrm{i}\,(\pm 0.15)$	283 ± 36	541 ± 92

Table 3.5: Threshold observables obtained from the fits explained in the text. Experimental data is taken from [18, 81, 82].

In Fig. 3.7 the total $K^-p \to K^-p, \bar{K}^0n, \pi^-\Sigma^+, \pi^+\Sigma^-, \pi^0\Sigma^0, \pi^0\Lambda$ cross sections obtained by **WT+NLO+Born (η chan)** and **WT+NLO+Born+RES** fits are represented. Both models give a very similar description, almost indistinguishable to the naked eye, of these cross sections which accommodate the experimental data very well.

The contribution of resonances provides additional structures to the cross section (obviously much more pronounced in the reactions whose amplitudes contain explic-

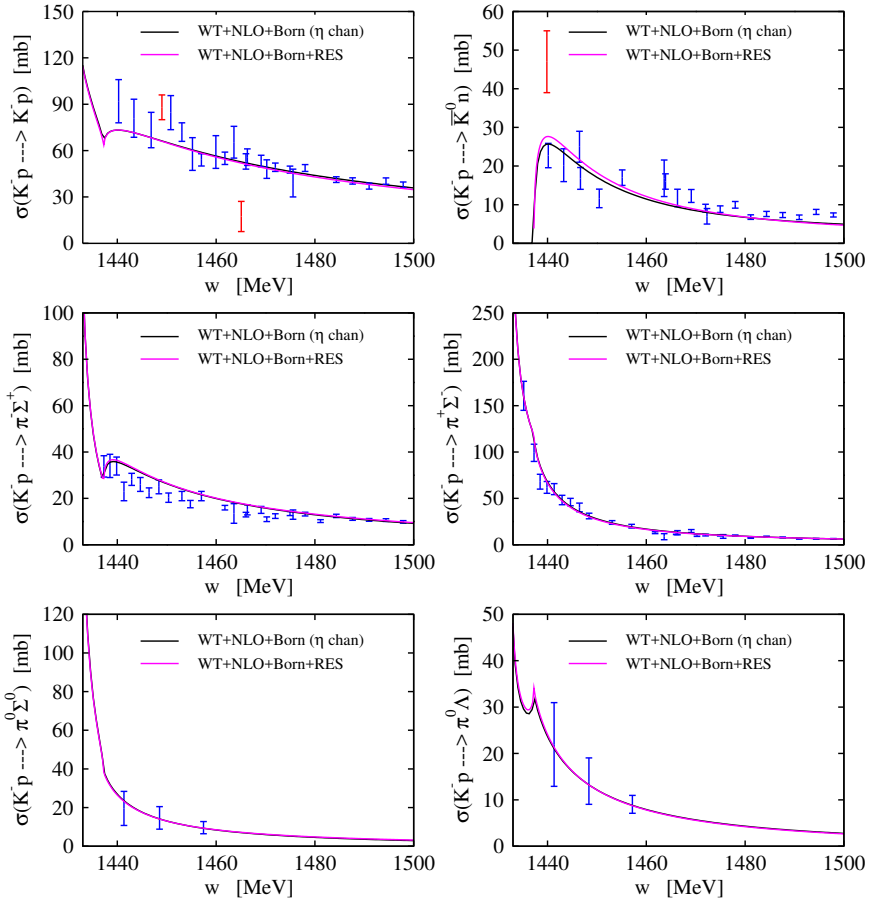

Figure 3.7: Total cross sections for the $K^-p \to K^-p, \bar{K}^0n, \pi^-\Sigma^+, \pi^+\Sigma^-, \pi^0\Sigma^0, \pi^0\Lambda$ reactions obtained from the **WT+NLO+Born+RES** fit (magenta line) and the **WT+NLO+Born (η chan)** fit (black line), see text for more details. Experimental data is from [70–73]. The points in red have not been included in the fitting procedure.

itly such terms, namely $K^-p \to \eta\Lambda, K^0\Xi^0, K^+\Xi^-$ ones). Partly, the choice of these proceses was motivated by the fact related to the loss of agreement between the **WT+NLO+Born (η chan)** model (black line in Fig. 3.8) and the scattering data corresponding to the $K^-p \to K^0\Xi^0$ reaction at low energy and to the $K^-p \to \eta\Lambda$ reaction around 1950 MeV. From them, one appreciates a clear improvement in reproducing the experimental $K^-p \to \eta\Lambda$ cross section in the energies ranging from 1850 to 2200 MeV, and, at the same time, the **WT+NLO+Born+RES** fit (magenta line)

respects the resonant structure from the $\Lambda(1670)$. But, probably, the most notable effect is the one observed in $K^-p \to K^0\Xi^0$ cross section, which reproduces better the experimental data located just above threshold due to the $\Lambda(1890)$ resonance. Moreover, the combined contribution of the $\Sigma(2030)$ and $\Sigma(2250)$ resonances provides a clear bump structure reaching its maximum at around 2100 MeV. A similar behavior for low energies can be noticed in the $K^-p \to K^+\Xi^-$ cross section, while, in the vicinity of the energy where the experimental data shows a maximum, the $\Sigma(2030)$ and $\Sigma(2250)$ resonant contributions produce some structure, together with a slight reduction of strength. With respect to the $K^-p \to \eta\Sigma^0$ cross section, we do not notice any difference in the reproduction of the experimental data, but for energies around 1800 MeV the **WT+NLO+Born+RES** presents a more pronounced slope.

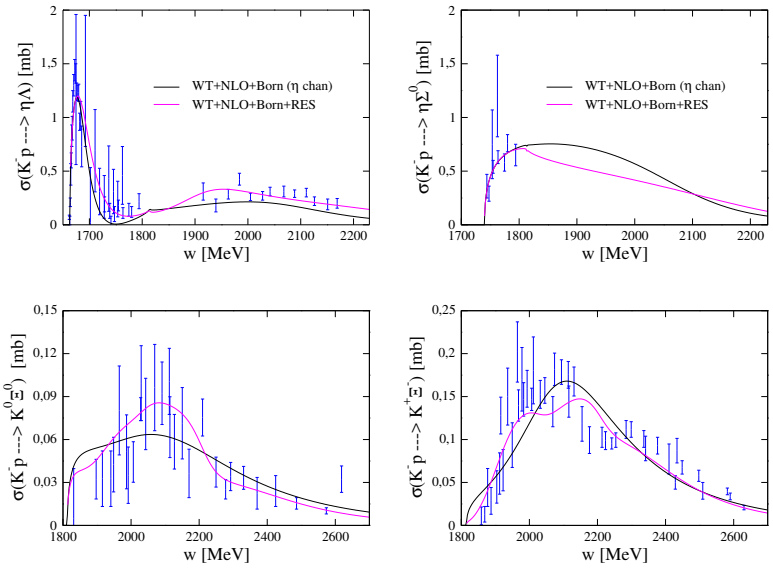

Figure 3.8: Total cross sections for the $K^-p \to \eta\Lambda, \eta\Sigma^0, K^0\Xi^0, K^+\Xi^-$ reactions obtained from the **WT+NLO+Born+RES** fit (magenta line) and the **WT+NLO+Born (η chan)** fit (black line), see text for more details. Experimental data is from [74–80, 86–89].

The most remarkable fact in Table 3.6 is the 16% of improvement in the goodness

of the fit, as is clearly reflected in $\chi^2_{\text{d.o.f.}}$ values. The results of the fitting parameters of both models are also shown in this table. It can be appreciated that the fitting parameters are quite stable, this stability being more marked for the NLO coefficients. The reason stems in the fact that we have employed more observables sensitive to the NLO term, namely the scattering data from the $K^-p \to \eta\Lambda, K^0\Xi^0, K^+\Xi^-$ reactions. We would like to stress the particular case of the d_2 and d_3 coefficients which have been specially stable since we used the full interaction kernel (**WT+NLO+Born+RES**, **WT+NLO+Born (η chan)** and **WT+NLO+Born** models). This is tied to the dependence of Clebsch-Gordan-type coefficients on d_2 and d_3 for the NLO contributions (eq. (1.65)) of the $K^-p \to K^0\Xi^0, K^+\Xi^-$ reactions. As can be seen from Table 4.2 in Appendix A, the NLO terms for these two processes can only proceed via the contribution related to the L_{ij} coefficients which depends on the d_2 and d_3 coefficients since D_{ij} are zero in all cases.

On the other hand, as a consequence of this stability, we still obtain natural sized subtraction constants. Another interesting result shown in Table 3.6 is that the f parameter has decreased after the inclusion of the resonances, which is in contrast to what happens when comparing the f values for the **NLO*** and **NLO+RES** models in Table 3.3 where this parameter remains almost invariable.

Regarding the accuracy, we obtain similar errors associated to the fitting parameters for both models (**WT+NLO+Born (η chan)** and **WT+NLO+Born+RES**) . We can stress the slight improvement for b_0, d_2 while, even with the slight improvement of the absolute error of d_4, the relative error has increased notably.

Finally, for completeness, in Fig. 3.9 we present the prediction of the total cross section of the $K^0_L p \to K^+\Xi^0$ reaction given by **WT+NLO+Born+RES** model (see

Sect. 2.4 for more details). We have also included the predictions of other previous models, already shown in Fig. 2.8 of Sect. 2.4, to see their evolution in describing this observable when more ingredients are taken into acount.

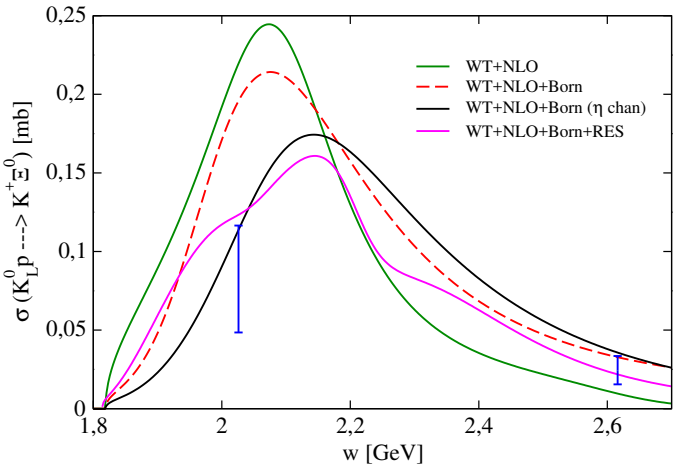

Figure 3.9: Total cross sections of the $K_L^0 p \to K^+\Xi^0$ reactions for the for the **WT+NLO** fit (green line), the **WT+NLO+Born** fit (red dashed line), the **WT+NLO+Born (η chan)** fit (black line) and the **WT+NLO+Born+RES** fit (magenta line), and the experimental points of the $I = 1$ $K^- n \to K^0\Xi^-$ reaction, taken from [95, 96] and divided by two, see Sect. 2.4 for more details.

The **WT+NLO+Born+RES** model gives a similar reproduction of the experimental points to that provided by the **WT+NLO+Born (η chan)** model, but the energy dependence of the cross section shows some structures associated to the included resonances. In view of these results, new experimental data would be crucial to determine which model might offer a more realistic description of this observable.

	WT+NLO+Born (η chan)	WT+NLO+Born+RES
$a_{\bar{K}N}$ (10^{-3})	1.27 ± 0.12	1.52 ± 0.21
$a_{\pi\Lambda}$ (10^{-3})	-6.1 ± 12.9	-2.6 ± 13.9
$a_{\pi\Sigma}$ (10^{-3})	0.68 ± 1.43	2.1 ± 1.2
$a_{\eta\Lambda}$ (10^{-3})	-0.67 ± 1.06	0.76 ± 1.21
$a_{\eta\Sigma}$ (10^{-3})	8.00 ± 3.26	10.1 ± 3.7
$a_{K\Xi}$ (10^{-3})	-2.51 ± 0.99	-2.01 ± 0.74
f/f_π	1.20 ± 0.03	1.18 ± 0.03
b_0 (GeV^{-1})	0.13 ± 0.04	-0.07 ± 0.01
b_D (GeV^{-1})	0.12 ± 0.01	0.13 ± 0.01
b_F (GeV^{-1})	0.21 ± 0.02	0.27 ± 0.02
d_1 (GeV^{-1})	0.15 ± 0.03	0.14 ± 0.03
d_2 (GeV^{-1})	0.13 ± 0.03	0.13 ± 0.01
d_3 (GeV^{-1})	0.30 ± 0.02	0.40 ± 0.02
d_4 (GeV^{-1})	0.25 ± 0.03	0.02 ± 0.02
D	0.70 ± 0.16	0.70 ± 0.15
F	0.51 ± 0.11	0.40 ± 0.11
$g_{\Lambda Y_{3/2}\eta} \cdot g_{NY_{3/2}\bar{K}}$	-	8.9 ± 11.8
$g_{\Xi Y_{3/2}K} \cdot g_{NY_{3/2}\bar{K}}$	-	6.20 ± 8.21
$g_{\Xi Y_{5/2}K} \cdot g_{NY_{5/2}\bar{K}}$	-	-3.88 ± 9.58
$g_{\Xi Y_{7/2}K} \cdot g_{NY_{7/2}\bar{K}}$	-	-14.3 ± 14.4
$\Lambda_{3/2}$ (MeV)	-	839.7 ± 406.7
$\Lambda_{5/2}$ (MeV)	-	541.3 ± 290.0
$\Lambda_{7/2}$ (MeV)	-	500.0 ± 426.8
$M_{Y_{3/2}}$ (MeV)	-	1910.0 ± 44.7
$M_{Y_{5/2}}$ (MeV)	-	2210.0 ± 39.1
$M_{Y_{7/2}}$ (MeV)	-	2040.0 ± 14.88
$\Gamma_{3/2}$ (MeV)	-	200.0 ± 120.3
$\Gamma_{5/2}$ (MeV)	-	150.0 ± 52.4
$\Gamma_{7/2}$ (MeV)	-	150.0 ± 43.1
$\chi^2_{\text{d.o.f.}}$	1.14	0.96

Table 3.6: Values of the parameters and the corresponding $\chi^2_{\text{d.o.f.}}$, defined in eq. (2.10), for the different fits described in the text. The subtraction constants are taken at a regularization scale $\mu = 1$ GeV. The error bars of the parameters are those given by the MINUIT minimization procedure.

Chapter 4

The Λ_b decay

Along this work, we have been studying the introduction of higher order terms of the chiral lagrangians in the kernel of the meson-baryon interaction in the strangeness $S = -1$ sector as a response to the need to extend the approach to higher orders and energies aiming for greater accuracy in data description. This necessarily passes through the determination of the low energy constants, particularly those which are not well established yet, namely the NLO coefficients. With this motivation, we focused on the $K^- p \to K^+ \Xi^-, K^0 \Xi^0$ reactions, since they do not proceed from the WT term of the chiral lagrangian and, hence, they are especially sensitive to the higher order terms. We devoted the second chapter to check which were the effects on the low energy constants of the systematic inclusion of new contributions to the interaction kernel (NLO and Born terms) and more experimental data in the fitting procedures. Most of the data employed in all fits are coming from antikaon proton scattering and therefore contain contributions from both isospin $I = 0$ and $I = 1$ components, exceptions being the $\pi^0\Sigma^0$, $\eta\Lambda$ and $\eta\Sigma^0$ production channels, which select $I = 0$, $I = 0$ and $I = 1$

respectively. As we have seen, the incorporation of data coming from these two last channels gave rise to a successful model (**WT+NLO+Born (η chan)**) with a suitable parametrization in terms of accuracy and homogeneity as well as in fixing reasonable subtraction constants.

These results point out that since the main differences among the models lie on the fact that they present very different distributions of their isospin components for the total cross sections, we could have more reliable values for all the fitting parameters and, therefore, more reliable values for the NLO constants by including additional data coming from isospin filtering processes. One such opportunity arises from the weak decay of the Λ_b into states containing a J/Ψ and meson-baryon pairs, measured by the CDF [91] and LHCb [40, 92, 93] collaborations which, as we will see, filters the $I = 0$ components of the meson-baryon interaction. In this respect, the experimental data of the invariant masses of the Λ_b decay into $J/\psi\ K\Xi$ and $J/\psi\ \eta\Lambda$ would provide valuable information, novel so far, that would enrich our knowledge of the meson-baryon interaction and help us to make progress in our understanding of hadron dynamics. Moreover, the $\Lambda_b \to J/\psi\ \eta\Lambda$ decay not only can provide such a new information but it can be an interesting process to observe a possible strange partner of the hidden charm pentaquark state $P_c(4450)$. Indeed, the measurement of the $\Lambda_b \to J/\Psi\ K^- p$ decay has been employed very recently in [40] to claim the presence of an exotic pentaquark charmonium state in the $J/\Psi\, p$ channel.

4.1 The $\Lambda_b \to J/\psi\ K\Xi,\ J/\psi\ \eta\Lambda$ decay processes

The authors of [90], which is the pioneering theoretical study of processes through which the Λ_b decays into a J/ψ and a $S = -1$ meson-baryon pair, found that this type of reactions do filter the final meson-baryon components in $I = 0$. They particularize this study for the $\Lambda_b \to J/\psi\ K^- p(\pi\Sigma)$ decay predicting the contribution of the tail of the $\Lambda(1405)$ in the $K^- p$ invariant mass distribution before the experimental confirmation [40].

In the present chapter we focus on the study of the $\Lambda_b \to J/\psi\ K\Xi$ and the $\Lambda_b \to J/\psi\ \eta\Lambda$ decay processes, since they are very sensitive to the details of the meson-baryon interaction at high energies, in particular to the higher order terms. The weak decay mechanism in these reactions is the same as that producing J/ψ and $K^- p$ or $\pi\Sigma$, except that different channels are chosen in the final state interaction of the very few meson-baryon states which are allowed to be produced in a primary step by the selection rules. More specifically, the Λ_b decays weakly into J/ψ and three quarks that hadronize to produce the primary meson-baryon components, which turn out to be $\bar{K}N$ and $\eta\Lambda$, as we will see. The final state interaction of these states in coupled channels allows the production of $K\Xi$ in the case of the $\Lambda_b \to J/\psi\ K\Xi$ decay. Thus, not having the $K\Xi$ pair produced in the first step, it comes from rescattering of meson-baryon components and hence this decay process depends strongly on the behaviour of the meson-baryon interaction.

4.1.1 Formalism

In the decay of the Λ_b into J/ψ at the elementary quark level we must bear in mind that the $q \to q'$ transitions at the Wqq' vertices are determined by the Cabibbo-Kobayashi-Maskawa (CKM) matrix elements [100]. The $u \to d$ and $c \to s$ transitions are given by the cosine of the Cabibbo angle, $\cos\theta_C$, thus being Cabibbo favored, the $b \to c$ transition proceeds via $A\sin^2\theta_C$ and is Cabibbo suppressed, while the transition $b \to u$ would be doubly Cabibbo suppressed [101]. At the quark level, the Cabibbo favoured mechanism for J/ψ production is depicted by the first part of the diagram of Fig. 4.1, where we can see the W-exchange weak process transforming the b quark into $c\bar{c}s$. This corresponds to internal emission in the classification of topologies of [100], and is also the dominant mechanism in the related $\bar{B}^0 \to J/\psi\ \pi\ \pi$ decay [102–104]. From the process depicted in the figure, after the weak decay, we obtain a sud state whose u and d quarks has remained as spectators. The reason being that one expects one-body operators in a microscopical evaluation to have larger strength than two- or multi-body operators. According to this assumption, since the Λ_b has isospin $I = 0$, so does the spectator ud pair, which, combined with the s quark after the weak decay, can only form $I = 0$ Λ states. The findings of the experimental analysis of Ref. [40] clearly support this hypothesis.

The next step consists in the hadronization of this final three quark state by introducing a $\bar{q}q$ pair with the quantum numbers of the vacuum, $\bar{u}u + \bar{d}d + \bar{s}s$. The dominant contribution of the hadronization preserves the spectator role of the ud pair, which ends up into the final baryon, and requires the involvement of the s quark, which ends up into the final meson. Any other topology that would bring the u or d quark into the final meson requires a large momentum transfer that suppresses the mecha-

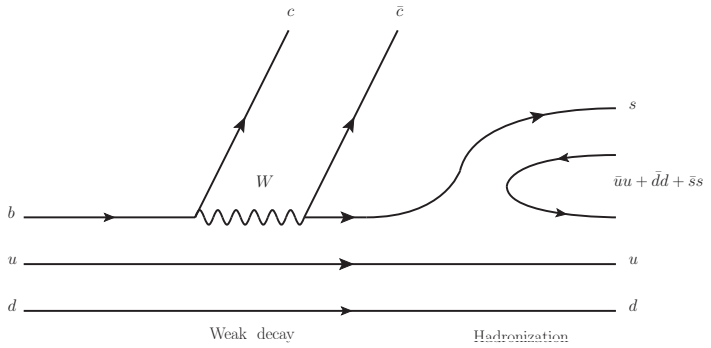

Figure 4.1: Diagram describing the weak decay of the Λ_b into the J/ψ and a meson-baryon pair formed through a hadronization mechanism.

nism. Another observation concerning the hadronization is that, since the *sud* quark state after the weak decay has $J^P = 1/2^-$ and the *ud* quarks have the same quantum numbers as in the original Λ_b state ($J^P = 1/2^+$ each) in an independent quark model used for the argumentation, it is the s quark the one that must carry the minus parity, which would correspond to an $L = 1$ orbit of a potential well. Since in the final K^- or η mesons the s quark is in its ground state with $L = 0$, this also implies that the s quark produced immediately after the weak process must participate actively in the process of hadronization, which proceeds as shown in Fig. 4.1. A further discussion on the reduced size of other alternative mechanisms can be found in [105].

The technical way to implement the hadronization and produce meson-baryon pairs in the final state follows the same steps as in [103, 106, 107] for meson decays and in [33, 90] for the Λ_b decay. The flavour decomposition of the Λ_b state is:

$$|\Lambda_b\rangle = \frac{1}{\sqrt{2}}|b(ud - du)\rangle\ , \tag{4.1}$$

which becomes, after the weak process

$$|H\rangle = \frac{1}{\sqrt{2}}|s(ud-du)\rangle \ , \tag{4.2}$$

or, upon hadronization,

$$|H\rangle = \frac{1}{\sqrt{2}}|s(\bar{u}u+\bar{d}d+\bar{s}s)(ud-du)\rangle \ , \tag{4.3}$$

which can be written in terms of the $q\bar{q}$ matrix P, as

$$|H\rangle = \frac{1}{\sqrt{2}}\sum_{i=1}^{3}|P_{3i}q_i(ud-du)\rangle \ , \tag{4.4}$$

where

$$P = \begin{pmatrix} u\bar{u} & u\bar{d} & u\bar{s} \\ d\bar{u} & d\bar{d} & d\bar{s} \\ s\bar{u} & s\bar{d} & s\bar{s} \end{pmatrix} \quad \text{and} \quad q = \begin{pmatrix} u \\ d \\ s \end{pmatrix} \ . \tag{4.5}$$

Writing the matrix P in terms of the meson states, $P \to \phi$, where the η, η' mixing [**?**] has been assumed,

$$\phi = \begin{pmatrix} \frac{\pi^0}{\sqrt{2}} + \frac{\eta}{\sqrt{3}} + \frac{\eta'}{\sqrt{6}} & \pi^+ & K^+ \\ \pi^- & -\frac{\pi^0}{\sqrt{2}} + \frac{\eta}{\sqrt{3}} + \frac{\eta'}{\sqrt{6}} & K^0 \\ K^- & \bar{K}^0 & -\frac{\eta}{\sqrt{3}} + \frac{2\eta'}{\sqrt{6}} \end{pmatrix} , \tag{4.6}$$

the hadronized state becomes:

$$|H\rangle = \frac{1}{\sqrt{2}}\Big(K^-u(ud-du) + \bar{K}^0d(ud-du) + \frac{1}{\sqrt{3}}\left(-\eta+\sqrt{2}\eta'\right)s(ud-du)\Big). \tag{4.7}$$

By the former equation one obtains the mixed antisymmetric representation of the octet of baryons and taking the results of [108] one finds the final meson-baryon components of $|H\rangle$. As was pointed out in [109], this point requires a careful comparison of the phase conventions of Ref. [108] with those inherent in the baryon matrix (eq. (1.43)) used in the chiral lagrangians. It is found that a change in the phases of Σ^+, Λ, Ξ^0 from [108] is needed to be in agreement with these fields within the chiral lagrangians. Thus, we have

$$|H\rangle = |K^- p\rangle + |\bar{K}^0 n\rangle + \frac{\sqrt{2}}{3}|\eta\Lambda\rangle \tag{4.8}$$

where we have omitted the $|\eta'\Lambda\rangle$ contribution because of the large mass of the η' meson [90]. Thus, the $K^- p$, $K^0 n$ or $\eta\Lambda$ pairs are the primary productions. From this, we can see that a $K\Xi$ pair is not produced in the first step. The $\eta\Sigma$ configurations cannot appear because it has $I = 1$.

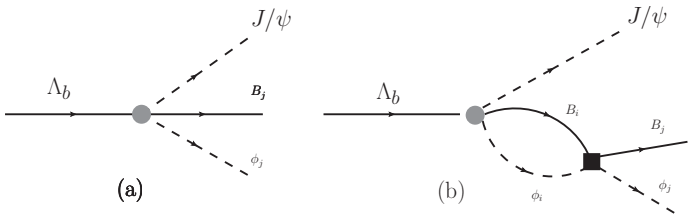

Figure 4.2: Diagrammatic representation of the decay amplitude for $\Lambda_b \to J/\psi\, \phi_j B_j$: (a) tree level and (b) the $\phi_j M_j = \eta\Lambda, K\Xi$ production through the coupled channel interaction of the initially produced $\phi_i M_i = \eta\Lambda, \bar{K}N$ meson-baryon pairs.

The final step consists in taking into account the final state interaction of the meson-baryon pairs. The amplitudes for the $\Lambda_b \to J/\psi\, \eta\Lambda, J/\psi\, K\Xi$ decays will then be built from the diagrams of Fig. 4.2, where we can see the direct tree-level process, depicted by diagram (a), and the final-state interaction contribution of the meson-baryon pair

into $\eta\Lambda, K\Xi$ production (b). The corresponding amplitude can be written as:

$$\mathcal{M}(M_{\phi B}, M_{J/\psi B}) = V_p\Big[h_{\phi B} + \sum_i h_i G_i(M_{\phi B}) t_{i,\phi B}(M_{\phi B})\Big], \tag{4.9}$$

where the weights h_i, obtained from Eq. (4.8), are:

$$h_{\pi^0\Sigma^0} = h_{\pi^+\Sigma^-} = h_{\pi^-\Sigma^+} = 0\,,\ h_{\eta\Lambda} = \tfrac{\sqrt{2}}{3}\,, \tag{4.10}$$

$$h_{K^-p} = h_{\bar{K}^0 n} = 1\,,\ h_{K^+\Xi^-} = h_{K^0\Xi^0} = 0\ , \tag{4.11}$$

and where G_i, with $i = K^-p, \bar{K}^0 n, \eta\Lambda$, denotes the one-meson-one-baryon loop function (eq. (1.71)) and the amplitude $t_{i,\phi B}$ is chosen in accordance with the models employed in this study. Here, ϕB are $\eta\Lambda$ or $K\Xi$. The $M_{\phi B}, M_{J/\psi B}$ stand for the invariant masses of the corresponding meson-baryon pairs.

The factor V_p, which includes the common dynamics of the production of the different pairs, is unknown and we take it as constant. This may in principle look like a very strong assumption since it is well known that the quantitative description of weak decay processes involving hadrons is a very arduous and challenging task. Indeed, semileptonic decay amplitudes are written in terms of the CKM quark-mixing parameter for the $q \to q'$ transition and a hadron matrix element which is parameterized in terms of form factors. These have been obtained from a variety of approaches, such as the non-relativistic constituent quark model [110], the covariant light front model [111], the relativistic quark model [112], or employing light cone sum rules [113]; see a recent comparison of these approaches in Ref. [114]. The situation is even more complicated in the case of non-leptonic decay modes, as the one addressed here, or semileptonic processes with two or more hadrons in the final state. One must first deal with the

hard process that involves the weak transition and the hadronization. This requires the evaluation of transition matrix elements, into two or more hadrons, of an effective Hamiltonian built up from four-quark operators. There is a vast amount of literature on this subject and, typically, one employs the factorization approach at various degrees of sophistication [115–117]. This permits replacing the matrix elements of the four-quark operators by two independent hadronic currents, which are then related to their respective form-factors that can be evaluated e.g. from light-front distribution amplitudes, as done in [118,119]. In addition to the hard process, one must also account for the hadron final state interaction, which has been done using the Omnès representation [120–122], implementing Breit-Wigner or Flatté structures [123] or applying chiral unitary theory [119, 124]. Unlike many of these approaches, our aim is limited: we only deal with the meson-baryon system in s-wave and we are only concerned about a narrow window of invariant masses. All we need to apply our formalism is that the form factors for the primary production of hadrons prior to its final state interactions behave smoothly compared to the changes induced by these interactions. Including all the information of the hard transition part into a constant factor V_p we obtain, up to an arbitrary normalization, invariant mass distributions which carry information on the characteristics of the meson baryon interaction. Our assumption finds support from the work of Ref. [122]. Although calculations of the hard-scale matrix element are difficult, as commented above, there are cases that can be kept under control, like the semileptonic decays with two pseudoscalar mesons in the final state with small recoil, which can be treated in heavy meson chiral perturbative theory. The form factors for these processes have been evaluated explicitly in Ref. [122] and, for large invariant masses of the lepton system, the s-wave one behaves smoothly as a function of the invariant mass of the meson pair. If we now extrapolate these results to the present

problem, replacing the energetic lepton system by the massive J/Ψ particle, we can also assume a moderate dependence of the s-wave hard matrix elements on the invariant mass of the meson-baryon pair. There is also empirical evidence on the smoothness of these primary form factors. In [125] form factors for the decay of B mesons into J/Ψ and a light scalar meson are evaluated, finding $F^{\sigma}_{B^0_s}(m^2_{J/\psi})/F^{f_0}_{B^0_s}(m^2_{J/\psi}) = 1$, where σ, f_0 stand for the $f_0(500), f_0(980)$ mesons. In addition, using current data for B meson decays, Ref. [102] finds a ratio $F^{f_0}_{B^0_s}(m^2_{J/\psi})/F^{\sigma}_{B^0}(m^2_{J/\psi})$ which is also compatible with unity.

In summary, the studies quoted above tell us that, in the processes studied here, there is a broad range of energies, of a few hundreds of MeV, where we can consider the primary form factors associated to the hard process to behave smoothly, so that the energy dependence of $\mathcal{M}(M_{\phi B}, M_{J/\psi B})$ in eq. (4.9) can be associated essentially to the changes of the final state interaction.

The double differential cross-section for the $\Lambda_b \to J/\psi\, \phi B$ decay process reads:

$$\frac{d^2\Gamma}{dM_{\phi B} dM_{J/\psi B}} = \frac{1}{(2\pi)^3} \frac{4M_{\Lambda_b} M_B}{32 M^3_{\Lambda_b}} \overline{\sum} |\mathcal{M}(M_{\phi B}, M_{J/\psi B})|^2 2M_{\phi B} 2M_{J/\psi B} \ , \tag{4.12}$$

where, after performing the sum over final spins and polarizations and the average over initial spins (see appendix in [126]), one has:

$$\overline{\sum} |\mathcal{M}(M_{\phi B}, M_{J/\psi B})|^2 = 3 |\mathcal{M}(M_{\phi B}, M_{J/\psi B})|^2 \ , \tag{4.13}$$

with $\mathcal{M}$ being that of eq. (4.9).

In this section we are interested in presenting the results in terms of the invariant

masses $M_{\eta\Lambda}$ and $M_{K^+\Xi^-}$. We choose the later rather than $M_{K^0\Xi^0}$ because charged particles can be easily measured by detectors. Except the minor effects of the differences associated to the physical masses of the particles, the invariant mass distributions for $K\Xi$ final states are expected to be identical since this decay process involve only the $I = 0$ part of the strong meson-baryon amplitude.

Aiming for this, we fix the invariant mass $M_{\phi B}$ and integrate expression (4.12) over $M_{J/\psi\Lambda}$ in order to obtain $d\Gamma/dM_{\phi B}$. In this case, the integration limits are given by:

$$\left(M^2_{J/\psi B}\right)_{\max} = \left(E^*_B + E^*_{J/\psi}\right)^2 - \left(\sqrt{{E^*_B}^2 - M^2_B} - \sqrt{{E^*_{J/\psi}}^2 - m^2_{J/\psi}}\right)^2, \tag{4.14}$$

$$\left(M^2_{J/\psi B}\right)_{\min} = \left(E^*_B + E^*_{J/\psi}\right)^2 - \left(\sqrt{{E^*_B}^2 - M^2_B} + \sqrt{{E^*_{J/\psi}}^2 - m^2_{J/\psi}}\right)^2, \tag{4.15}$$

where

$$E^*_B = \frac{M^2_{\phi B} - m^2_\phi + M^2_B}{2M_{\phi B}}\ , \tag{4.16}$$

$$E^*_{J/\psi} = \frac{M^2_{\Lambda_b} - M^2_{\phi B} - m^2_{J/\psi}}{2M_{\phi B}}\ . \tag{4.17}$$

4.1.2 Results and discussion

We start this section by presenting in Fig. 4.3 the cross section data of the $K^- p \to K^0\Xi^0$ reaction (top panels) and of the $K^- p \to K^-\Xi^+$ reaction (bottom panels), obtained employing **WT+NLO** model (left panels) or **WT+NLO+Born (η chan)** model (right panels). The figure shows the complete results (solid lines), as well as the results where only the isospin $I = 1$ component (dashed lines) or the $I = 0$ one (dash-dotted lines) have been retained. It is interesting to see that, in both models, the $I = 1$ component

is dominant. The $I = 1$ distribution for **WT+NLO** is a little bit more enhanced along the energy range than the corresponding to **WT+NLO+Born (η chan)** reaching its maximum at around 2050 MeV, while the analogous maximum for **WT+NLO+Born (η chan)** is shifted 100 MeV towards higher energies. The contribution of $I = 0$ in the $K^- p \to K\Xi$ cross section for **WT+NLO** is mainly significant around 2300 MeV which is in contrast to what happens to the $I = 0$ component for **WT+NLO+Born (η chan)** model. The $I = 0$ distribution corresponding to this last model is more evident near the threshold, it grows rapidly reaching a plateau, with strength similar to the previous maximum, to finally decrease with a smooth fall.

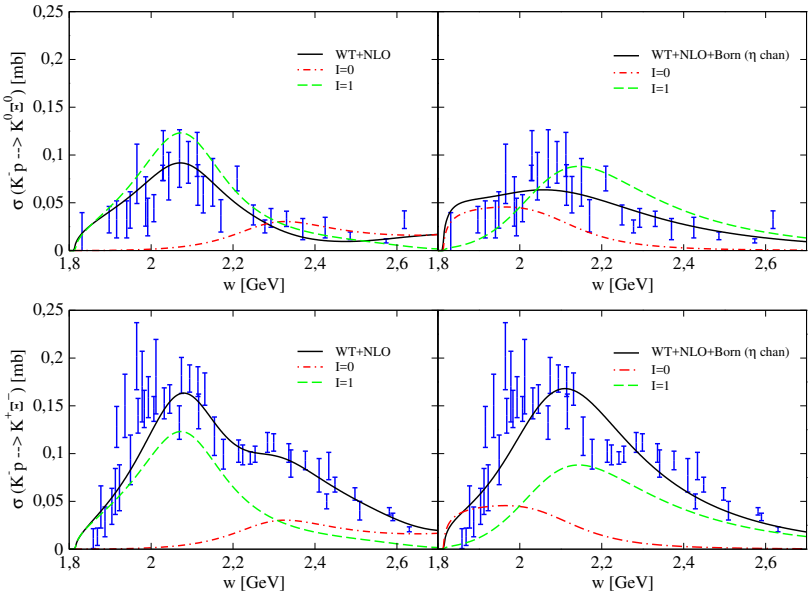

Figure 4.3: The total cross section data of the $K^- p \to K^0\Xi^0$ reaction is represented in the top panels, where the left figure corresponds to the **WT+NLO** model and the right one corresponds to the **WT+NLO+Born (η chan)** model. The same distribution for the bottom panels where the $K^- p \to K^+\Xi^-$ cross section data is represented. The figure shows the complete results by means of solid lines, the results where only isospin $I = 1$ component (dashed lines) or $I = 0$ one (dot-dashed line) have been retained.

Let us remind the reader that the **WT+NLO** model employs the dynamics of the

chiral lagrangian up to NLO, specifically the contributions of the WT term and the NLO ones. The **WT+NLO+Born (η chan)** differs, dynamically speaking, from the first one in the additional inclusion of the Born terms in the lagrangian. Regarding the experimental data to which they are fitted, the second model takes into account, apart from the same amount of experimental data as **WT+NLO** model, scattering data from the $K^- p \to \eta\Lambda, \eta\Sigma$ processes. This fact and the very different distributions of the isospin 0 component of the total $K^- p \to K\Xi$ cross sections given by these two models make them interesting candidates for a comparison. From now on, in order to simplify the notation, the **WT+NLO** and **WT+NLO+Born (η chan)** models will be referred to as **Model 1** and **Model 2**, respectivelly. In [33] we perform an analogous study but employing the models of [27] instead.

In Fig. 4.4, we show the invariant mass distributions of $\pi\Sigma$ and $\bar{K}N$ states, as averaged distributions over the possible different charged states, for the decay reactions $\Lambda_b \to J/\psi\ \bar{K}N$ and $\Lambda_b \to J/\psi\ \pi\Sigma$ employing **Model 1** and **Model 2**. In this way we can compare with the findings in [90].

We can see that the results of both models are very different from each other. On the one hand, the results from **Model 2** are very similar to those found in [90], with the shape of the $\pi\Sigma$ and $\bar{K}N$ distributions lying somewhat in between those of the Bonn and Murcia-Valencia models studied there (a different normalization is used in that work). We note that the $\pi\Sigma$ distribution corresponding to **Model 2** shown in Fig. 4.4 stays below the $\bar{K}N$ one just above the threshold for $\bar{K}N$ states, in agreement with what one observes in the models discussed in [90]. On the other hand, the invariant mass distribution of $\pi\Sigma$ for **Model 1** shows a minimum located essentially where **Model 2** has its maximum. Furthermore, the $\pi\Sigma$ distribution corresponding

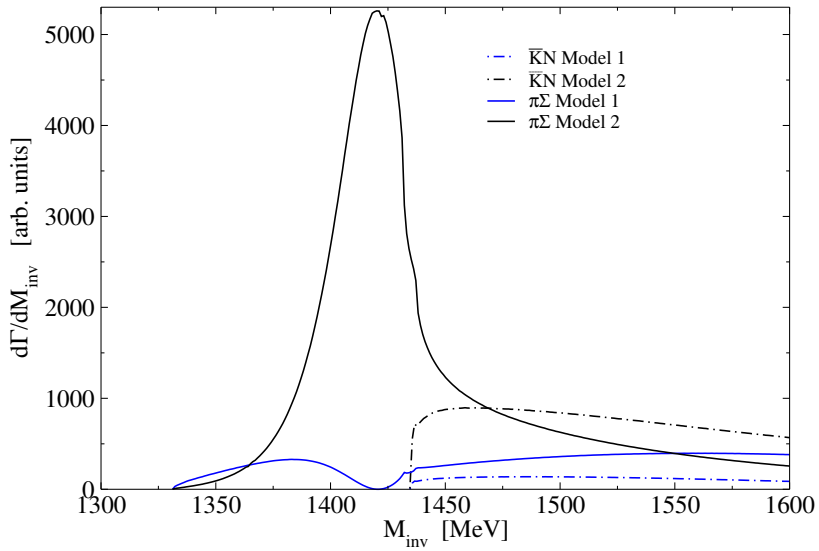

Figure 4.4: Invariant mass distributions of $\pi\Sigma$ and $\bar{K}N$ states in the decay modes $\Lambda_b \to J/\psi\ \pi\ \Sigma$ (solid line) and $\Lambda_b \to J/\psi\ \bar{K}\ N$ (dot-dashed line), for the two models discussed in the text: Model 1 (blue lines) and Model 2 (black lines). The units in the y axis are obtained taking $V_p = 1$.

to **Model 1**, in contrast to **Model 2** and the models in [90], stays over the $\bar{K}N$ one. These two dissimilar results, which are obviously the consequence of different patterns of interferences, reflect the sensitivity of these processes to the models. Actually, as seen from eq. (4.9), the rescattering term of the invariant mass distribution, which is dominant around the energy region of the $\Lambda(1405)$ resonance, depends not only on the strong scattering amplitudes, t_{ij}, but also on the loop functions, G_i. The effect of the rescattering term is more marked in the process leading to a final $J/\psi\ \pi\Sigma$ state because it lacks a tree-level term. Since the fitting procedures consider the parameters of the meson-baryon interaction simultaneously with those of the loop functions, there is some freedom on the values of these loop functions obtained by different strong interaction models that produce equivalent scattering amplitudes. In any case, since the global parameter V_p is unknown to us, the relevant information from this figure is the ratio of the $\pi\Sigma$ to $\bar{K}N$ distributions, at their respective maximum values for instance. The

ratios for **Model 1** and **Model 2** can be established in 2.3 and 5.7, respectively, the former being similar to those found in [90].

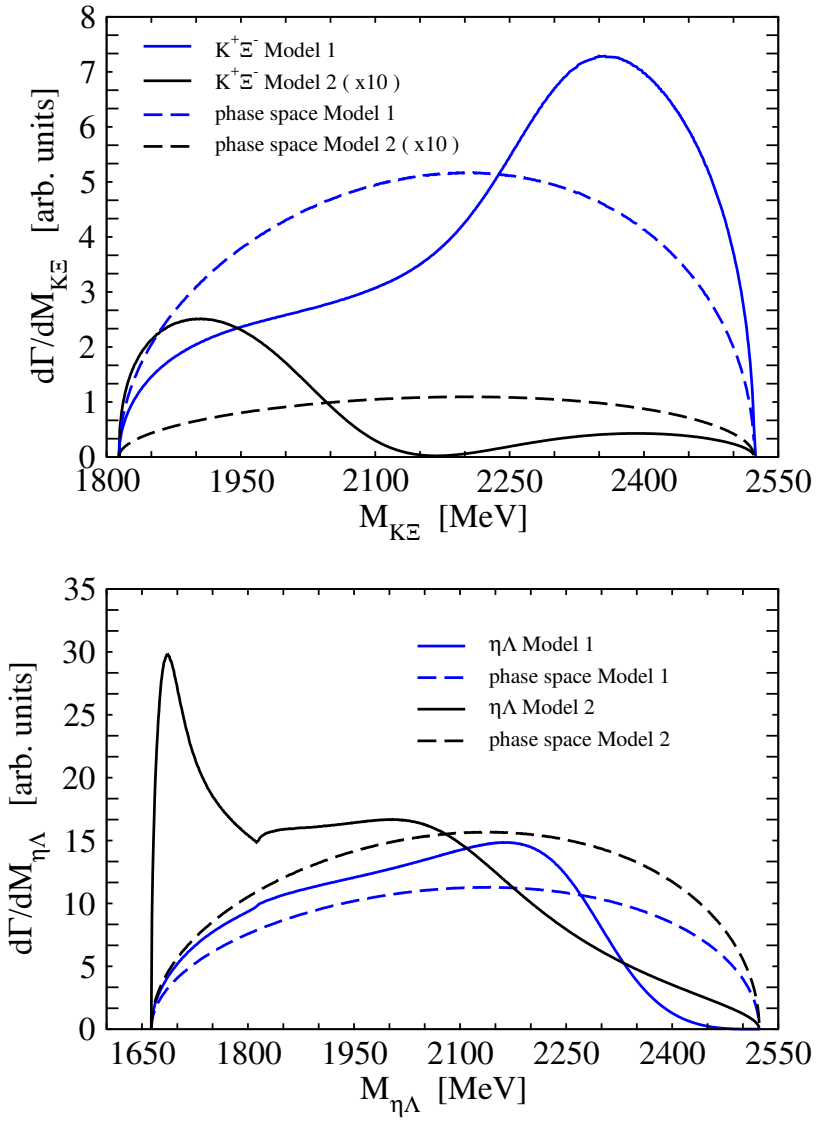

Figure 4.5: Invariant mass distributions of $K^+\Xi^-$ states (upper panel) and $\eta\Lambda$ states (lower panel) obtained for the two models discussed in the text: Model 1 (blue solid lines) and Model 2 (black solid lines). The pure phase-space distributions (dashed lines) are normalized to the corresponding invariant mass distribution, more details in the text. The invariant mass distribution of $K^+\Xi^-$ state and the corresponding phase-space distribution for Model 2 are multiplied by a factor 10 to aid its visualization.

Although we have given the invariant mass distributions in arbitrary units, one should bear in mind that all the figures, from Fig. 4.4 to Fig. 4.5 have the same normalization. Since measurements for the $\Lambda_b \to J/\psi\ K^- p$ reaction are already available from the CDF [91] and LHCb [40,92,93] collaborations, the measurements of the reactions proposed here could be referred to those of the $\Lambda_b \to J/\psi\ K^- p$ reaction and this would allow a direct comparison with our predictions. In this spirit, we note that the recent resonance analysis of [40] shows a $\Lambda(1405)$ contribution which lies in between the distribution found by the Bonn model in [90] and that of the Murcia-Valencia model in [90] or the models presented here.

In the upper panel of Fig. 4.5 we present the invariant mass distributions of $K^+\Xi^-$ pairs from the decay process $\Lambda_b \to J/\psi\ K^+\Xi^-$. Firstly, we would like to make clear that the invariant mass distribution of $K^+\Xi^-$ state and the corresponding phase-space distribution for Model 2 are multiplied by a factor 10 to aid its visualization. The fact that this decay filters the $I = 0$ components makes the differences between **Model 1** (blue solid line) and **Model 2** (black solid line) more evident, not only in the strength but also in the shape of the invariant mass distribution. In principle, from Fig. 4.3, one could expect that both models might give similar strength for these invariant mass distributions, but arranged almost in opposition to each other. As we clearly see from Fig. 4.5, the invariant mass distribution for both models is in accordance with Fig. 4.3 only in shape. The resulting strength from **Model 1** exceeds by more than 24 times the one from **Model 2**. The reason for such a difference stems from the fact that the selectivity of the Λ_b decay processes producing the J/ψ does not allow the formation of a $K\Xi$ pair in a primary step. This is only produced through rescattering of the $\bar{K}N$ and $\eta\Lambda$ primary components. Thus, the $\Lambda_b \to J/\psi\ K\Xi$ reaction is directly proportional to the meson-baryon scattering amplitude, concretely to the $\eta\Lambda \to K\Xi$ and $\bar{K}N \to K\Xi$

components in $I = 0$, which can lead to a marked pattern of interferences. The invariant mass distribution of the $K^+\Xi^-$ state for **Model 2** is a clear example of a destructive interference among the $\bar{K}N$ contributions and the $\eta\Lambda$ component as is illustrated in Fig. 4.6. There, we plot the $K\Xi$ invariant mass distribution when we exclude the $\eta\Lambda \to K\Xi$ amplitude by setting $h_{\eta\Lambda}$ to 0 (black dot-dashed line), or excluding the $\bar{K}N \to K\Xi$ contributions by setting h_{K^-p} and $h_{\bar{K}^0 n}$ to 0 (black solid line). Comparing these two black lines in Fig. 4.6, it is directly seen that the only way to obtain the complete invariant mass (red solid line) is by means of a destructive interference.

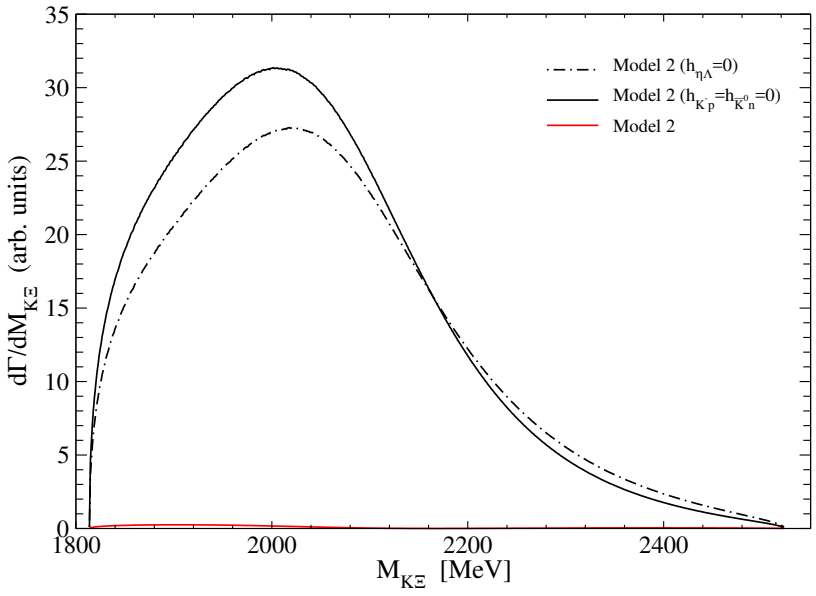

Figure 4.6: The effects on the invariant mass distributions of $K^+\Xi^-$ state for Model 2 obtained: switching off the $\bar{K}N$ contributions to $M_{K\Xi}$ (black solid line,$h_{K^-p} = h_{\bar{K}^0 n} = 0$) and switching off the $\eta\Lambda$ contribution to $M_{K\Xi}$ (black dot-dashed line,$h_{\eta\Lambda} = 0$). The full invariant mass distributions of $K^+\Xi^-$ state for Model 2 is represented by the red solid line.

If, in order to eliminate the dependence on undetermined loop functions and on the unknown weak parameter V_p, we represented each $\Lambda_b \to J/\psi\ K^+\Xi^-$ distribution relative to its corresponding $\Lambda_b \to J/\psi\ \bar{K}N$ one shown in Fig. 4.4, the difference would

be somewhat enhanced. Therefore, measuring the decay of the Λ_b into $J/\psi\ K^+\Xi^-$ and into $J/\psi\ \bar{K}N$ could help us discriminate between models that give a similar account of the scattering $K^-p \to K^0\Xi^0, K^+\Xi^-$ processes.

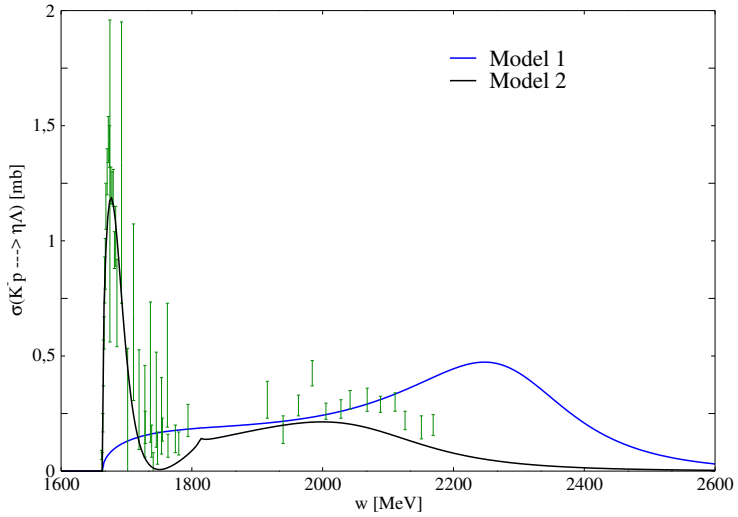

Figure 4.7: Total cross section for the $K^-p \to \eta\Lambda$ reaction obtained from the **Model 1** fit (blue line) and the **Model 2** fit (black line), see text for more details.

The $\Lambda_b \to J/\psi\ \eta\Lambda$ decay can proceed at tree level making the possible interference effects of the loop diagrams acquire a secondary role. This is clearly reflected when comparing $\Lambda_b \to J/\psi\ \eta\Lambda$, $J/\psi\ K^+\Xi^-$ distributions for **Model 2** (black solid lines) shown in Fig. 4.5, which differ by a factor of 65. This difference is enhanced due to the destructive interference of the rescattering terms for the $\Lambda_b \to J/\psi\ K^+\Xi^-$ decay, as we have seen in the previous paragraph. Conversely, the magnitude of the $\Lambda_b \to J/\psi\ \eta\Lambda$ distribution for **Model 1**(blue solid lines in the bottom panel of Fig. 4.5) is of the same order as the $\Lambda_b \to J/\psi\ K^+\Xi^-$ one (blue solid lines in the top panel of Fig. 4.5), even if the latter does not receive the contribution of the tree level term. This can be explained by means of a strong constructive interference of the reescattering terms, just the opposite of what happens for **Model 2**. The $\eta\Lambda$ invariant mass distributions

in the bottom panel of Fig. 4.5 corresponding to **Model 1** (blue solid line) and **Model 2** (black solid line), show a shape and relative strength between models similar to the $K^- p \to \eta\Lambda$ cross section (see Fig. 4.7).

In addition, the invariant mass distributions from the $\Lambda_b \to J/\psi\ K^+\Xi^-$ and $\Lambda_b \to J/\psi\ \eta\Lambda$ decays obtained in **Model 1** and **Model 2** are compared with phase space in Fig. 4.5. The phase-space distributions (dashed lines) are obtained by taking the amplitude $\mathcal{M}$ as constant in eq. (4.12) and normalizing to the area of the invariant mass distribution of the corresponding model. The comparison allows one to see that there are dynamical features in the meson-baryon amplitudes leading to a distinct shape of the mass distributions. In the case of **Model 1** (blue solid line), we observe a peaked structure around 2350 MeV in the $K^+\Xi^-$ distribution. This peak resembles a resonance, but we should take into account that the limitation of the phase space at about 2500 MeV produces a narrower structure than that of the cross sections of the $K^- p \to K\Xi$ reactions, as we can see from the $I = 0$ contribution in Fig. 4.3 (left panels), which is much broader. Actually, the very different shape that this model predicts for $\Lambda_b \to J/\psi\ \eta\Lambda$ (see blue solid lines in the bottom panel of Fig. 4.5), showing no peaked structure, which essentially implies the absence of a resonance since it would necessarily appear in both final states at the same energy. In our models, it is the energy dependence in the parametrization of the next-to-leading order contribution and the interference of terms that creates this shape. On the other hand, from the $\eta\Lambda$ invariant mass distribution corresponding to **Model 2**, we can still appreciate the dynamically generated $\Lambda(1670)$ resonance. In any case, what is clear is that the experimental implementation of this reaction will provide valuable information concerning the meson-baryon interaction at higher energies, beyond what is offered to us by present scattering data.

4.2 The hidden-charm $S = -1$ pentaquark in the $\Lambda_b \to J/\psi\ \eta\Lambda$ decay

The LHCb collaboration reported recently two exotic structures in the invariant $J/\psi p$ mass spectrum of the $\Lambda_b \to J/\psi\ K^- p$ process. These pentaquark states were named $P_c(4380)$, with a mass of $4380 \pm 8 \pm 29$ MeV and a width of $205 \pm 18 \pm 86$ MeV, and $P_c(4450)$, with a mass of $4449.8 \pm 1.7 \pm 2.5$ MeV and a width of $39 \pm 5 \pm 19$ MeV [40, 41]. Hidden charm baryon states with similar characteristics of the states reported had already been predicted, employing a molecular picture [35–39] or a quark model approach [127, 128]. A list of early references on pentaquark states can be seen in Ref. [129]. The CERN discovery triggered a large number of theoretical works trying to give an explanation for the two reported states. The molecular picture was invoked in [42, 130–132], the diquark picture in [133–137], QCD sum rules were used in [138, 139], and the soliton model was employed in [140]. It has also been argued that the observed enhancement could be due to kinematical effects or triangular singularities [141–143]. Suggestions of different reactions to observe the pentaquarks have been reported [144–148], while explicit decay modes to elucidate their structure have also been studied in [149, 150]. Further discussions on the issue and the nature of the two P_c states can be seen in Refs. [151, 152] and particularly in the recent detailed review of Ref. [153].

Concerning the present section, we recall that a theoretical study of the $\Lambda_b \to J/\psi\ K^- p$ reaction was done in [90], prior to the experimental study of Ref. [40], predicting the contribution of the tail of the $\Lambda(1405)$ in the $K^- p$ invariant mass distribution. The analysis of [40] contains such a contribution in agreement in shape with

the predictions, where the absolute normalization is unknown. Moreover, it was shown in [42] that the distributions in the pentaquark channel, i.e. in the invariant $J/\psi p$ mass spectrum of [40], could be explained via the incorporation of the hidden charm N^* states predicted in [35–38], which are molecular states mostly made from $\bar{D}^*\Sigma_c$ or $\bar{D}^*\Sigma_c^*$ components and having a small coupling to $J/\psi p$, one of their open decay channels. It is unlikely that there are no partners of the states found in [40], and indeed, in [35, 36] states of spin-parity $3/2^-$ with hidden charm but strangeness $S = -1$ were predicted, mostly made of $\bar{D}^*\Xi_c$ or $\bar{D}^*\Xi_c'$, decaying into $J/\psi\Lambda$. In view of this, the decay of Ξ_b^- into $J/\psi K^-\Lambda$ was suggested in [154] as a suitable reaction to find a hidden charm strange state. Predictions for the $\bar{K}\Lambda$ and $J/\psi\Lambda$ mass distributions were done, and, playing with uncertainties, it was shown that a clear peak in the $J/\psi\Lambda$ mass distribution should show up. This reaction is presently being considered by the LHCb collaboration. However, since there is a much smaller statistics in the production of Ξ_b^- than that of Λ_b, it is interesting to explore alternative reactions to observe this strangeness $S = -1$ hidden-charm pentaquark. In the present section we suggest to employ the $J/\psi\,\eta\Lambda$ decay mode of the Λ_b. Since the $\eta\Lambda$ pair is populated with a weight $\sqrt{2}/3$ relative to the K^-p pair in the primary $\Lambda_b \to J/\psi\ MB$ reaction (see eq. (4.9)), the $\Lambda_b \to J/\psi\ \eta\Lambda$ decay rate should be similar as that found for $J/\psi\ K^-p$ final states in the study of the non-strange pentaquark, and the new strange state should be looked for in the $J/\psi\Lambda$ mass distribution instead of the $J/\psi p$ one.

We note that the possible existence of an strange $S = -1$ pentaquark partner was also studied in [126] from the non-strange decay mode $\Lambda_b \to J/\psi\ K^0\Lambda$, which is one of the coupled channels of the decay $\Lambda_b \to J/\psi\ \pi^-p$ from which, even if it is more Cabbibo suppressed than the $\Lambda_b \to J/\psi\ K^-p$ process, a possible signal of the $P_c(4450)$ may also have been seen [41, 155]. The study of [126] explored the effect of different weak decay

amplitudes to produce either a $J^P = 1/2^-$ or a $J^P = 3/2^-$ strange pentaquark. In this work, we will also take these possibilities into account.

4.2.1 Formalism

In Sect.4.1.1, we discussed how the $\Lambda_b \to J/\psi\,\eta\Lambda$ decay is described by means of weak transition followed by a hadronization process whose topology is depicted in Fig. 4.1. The main motivation there was the study of the invariant mass distribution of the final $S = -1$ pseudoscalar meson-baryon pair in order to extract valuable information about its dynamics at higher energies by means of comparing with experimental data once available. Now we turn our attention to the $J/\psi\Lambda$ invariant mass distribution

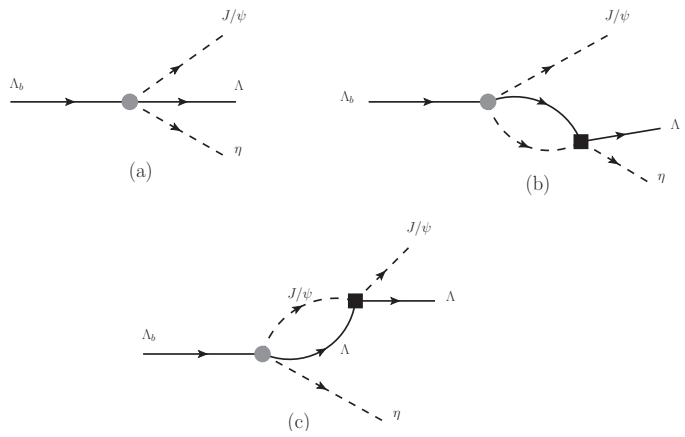

Figure 4.8: Diagrammatic representation of the decay amplitude for $\Lambda_b \to J/\psi\,\eta\Lambda$: a) tree level, b) the $\eta\Lambda$ production through the coupled channel interaction of the initially produced $\eta\Lambda$ and $\bar{K}N$ meson-baryon pairs, c) $J/\psi\Lambda \to J/\psi\Lambda$ interaction.

because, as we have mentioned, a strange partner of the $P_c(4450)$ could be associated to the molecular states $\bar{D}^*\Xi_c$ or $\bar{D}^*\Xi_c'$, which decay into $J/\psi\Lambda$, as was predicted by the authors of [35, 36]. To this end, we need to introduce some modifications in the final state interactions by new diagrams contributing to the $\Lambda_b \to J/\psi\,\eta\Lambda$ amplitude.

We first introduce the final-state $J/\psi\Lambda \to J/\psi\Lambda$ interaction which is schematically represented in diagram (c) of Fig. 4.8. Note that this figure also contains the other diagrammatic contributions which appeared originally in Fig. 4.2: the direct tree-level process, depicted by diagram (a) and the final-state interaction contribution of the meson-baryon pair into $\eta\Lambda$ production (b). Thus, the corresponding amplitude is obtained by adding the new contribution to eq. (4.9), namely:

$$\mathcal{M}(M_{\eta\Lambda}, M_{J/\psi\Lambda}) = V_p \Big[h_{\eta\Lambda} \quad + \sum_i h_i G_i(M_{\eta\Lambda}) t_{i,\eta\Lambda}(M_{\eta\Lambda}) + h_{\eta\Lambda} G_{J/\psi\Lambda}(M_{J/\psi\Lambda})\, t_{J/\psi\Lambda,J/\psi\Lambda}(M_{J/\psi\Lambda}) \Big], \tag{4.18}$$

where we take the loop function $G_{J/\psi\Lambda}$ employed in the model of [35, 36] on which, as we will show below, we base our prescription for the $t_{J/\psi\Lambda,J/\psi\Lambda}$ amplitude.

At this point it is worth mentioning that the model for the final state interaction in the $\eta\Lambda$ channel generates some resonances dynamically, like the $\Lambda(1405)$ or the $\Lambda(1670)$, that are either below or at the edge of the threshold of $\eta\Lambda$ invariant masses $M_{\eta\Lambda}$ accessible from the decay of the Λ_b. We therefore would like to explore the possibility of adding to the amplitude the explicit contribution of some Λ^* which lies in the relevant $M_{\eta\Lambda}$ region, essentially between 1700 MeV and 2500 MeV, and might couple sensibly to $\eta\Lambda$ states, as represented diagrammatically in Fig. 4.9. One state with these characteristics is listed in the PDG compilation [99], the one star $\Lambda(2000)$, having a width $\Gamma \sim 100 - 300$ MeV and a branching ratio to the decay into $\eta\Lambda$ of $(16 \pm 7)\%$. The recent unitary multichannel model for $\bar{K}N$ scattering, with parameters fitted to partial waves up to $J = 7/2$ and up to 2.15 GeV of energy, also gives an s-wave $J^P = 1/2^-$ Λ state with similar mass and width properties [156]. We also note

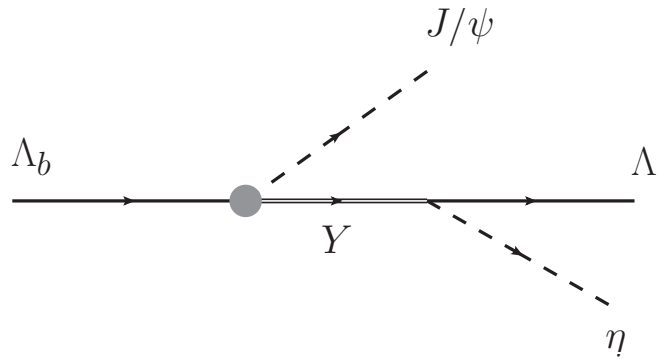

Figure 4.9: Diagrammatic representation of an s-wave resonance contribution to the $\Lambda_b \to J/\psi\,\eta\Lambda$ decay amplitude.

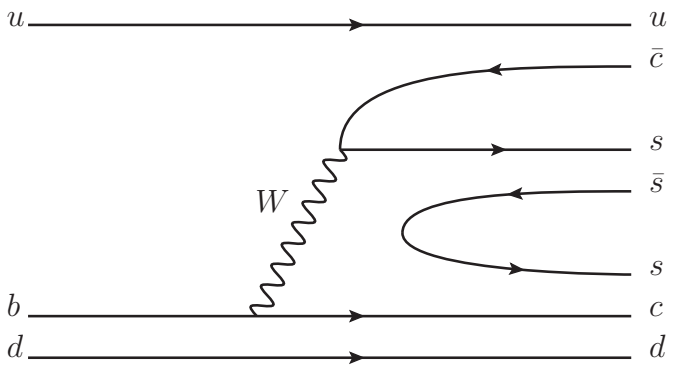

Figure 4.10: Diagram describing the weak decay Λ_b into the $\bar{D}^*$ and a $\eta\Xi_c'$ pair.

that, since our model will rely on the strange pentaquark predicted in Refs. [35, 36] at an energy around 4550 MeV, which couples strongly to $\bar{D}^{*0}\Xi_c'$ states, one should consider the possibility that the influence of this resonance in the final $J/\psi\Lambda$ mass distribution could also be due to the creation of a virtual $\bar{D}^*\eta\Xi_c'$ state in a first step of the Λ_b decay, through the mechanism of Fig. 4.10, followed by multiple interactions to generate the resonance, which would eventually decay into a $J/\psi\Lambda$ pair in the final state, represented by the diagrams of Fig. 4.11. However, this configuration requires a different topology, as seen in Fig. 4.10, in which the ud quarks of the Λ_b do not act as a coupled spectator pair. Although it is hard to quantify the size of the amplitude

of Fig. 4.1 with respect to that of Fig. 4.10, the fact that in this later case one of the spectator quarks ends up in the charmed meson and the other one goes to the baryon makes us believe that the corresponding amplitude will be reduced. We will therefore assume the dominance of the mechanism of Fig. 4.1 over that of Fig. 4.10 by a factor of two or more and will give predictions for different relative signs of the two processes. We note that the lowest order contribution to the $\Lambda_b \to J/\psi\,\eta\Lambda$ decay induced by virtual $\bar{D}^*\eta\Xi_c'$ states is the amplitude of Fig. 4.11 (a). We have checked, by explicit numerical evaluation, that the next-order contribution of Fig. 4.11 (b), involving the additional final state interaction of the $\eta\Lambda$ pair, gives a negligible correction, hence it will be ignored in the results presented in Sect. 4.2.2.

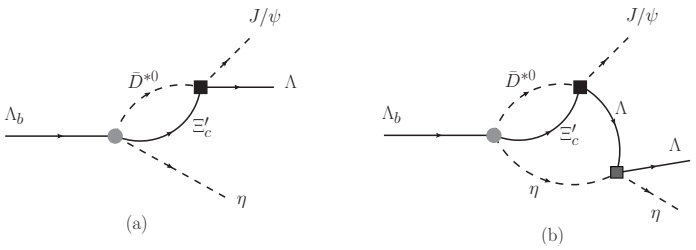

Figure 4.11: Diagrammatic representation of the decay of the Λ_b into a virtual $\eta\bar{D}^{*0}\Xi_c'$ intermediate state, followed by the $\bar{D}^{*0}\Xi_c' \to J/\psi\Lambda$ conversion process, (a), and implementing also the final state interaction of the final $\eta\Lambda$ pair, (b).

Adding the s-wave resonant contribution of Fig. 4.9 and the process initiated by an intermediate $\bar{D}^*\eta\Xi_c'$ state followed by final state interactions leading to a $J/\psi\Lambda$ pair and an η meson represented by the diagram of Fig. 4.11 (a), the final amplitude for

$\Lambda_b \to J/\psi\,\eta\Lambda$ decay, producing a strange pentaquark with $J^P = 1/2^-$ becomes:

$$\begin{aligned}\mathcal{M}(M_{\eta\Lambda}, M_{J/\psi\Lambda}) = V_p\Big[h_{\eta\Lambda} \quad &+\sum_i h_i G_i(M_{\eta\Lambda}) t_{i,\eta\Lambda}(M_{\eta\Lambda}) \\ &+ h_{\eta\Lambda} G_{J/\psi\Lambda}(M_{J/\psi\Lambda})\, t_{J/\psi\Lambda,J/\psi\Lambda}(M_{J/\psi\Lambda}) \\ &+ \beta\; G_{\bar{D}^*\Xi_c'}(M_{\bar{D}^*\Xi_c'})\, t_{\bar{D}^*\Xi_c',J/\psi\Lambda}(M_{J/\psi\Lambda}) \\ &+ \alpha\, \frac{M_{\Lambda^*(2000)}}{M_{\eta\Lambda} - M_{\Lambda^*(2000)} + \mathrm{i}\,\frac{\Gamma_{\Lambda^*(2000)}}{2}}\Big]\,, \end{aligned} \tag{4.19}$$

where α is a dimensionless parameter that determines the strength of the s-wave resonant mechanism, while β controls the strength of Λ_b decaying virtually into $\bar{D}^*\eta\Xi_c'$, relative to its decay into $J/\psi\,\eta\Lambda$.

The amplitudes of eqs. (4.18) and (4.19) come with the matrix element $\langle m_\Lambda \mid \vec{\sigma}\vec{\epsilon}\,\mid m_{\Lambda_b}\rangle$, tied to the s-wave character assumed for the weak decay vertex and accounting for the spin 1/2 of the decaying Λ_b, and the spins 1/2 and 1 of the emitted Λ and J/ψ meson, respectively. Moreover, as will be recalled in the following paragraphs, the $J/\psi\Lambda$ (and $\eta\Lambda$) interaction models are also taken in s-wave, hence the spin values of the $J/\psi\Lambda$ pair could in principle be $J = 1/2$ or $J = 3/2$. However, the $\vec{\sigma}\vec{\epsilon}$ operator projects the $J/\psi\Lambda$ system into $J = 1/2$ as shown in [157] and in this case only the $J = 1/2$ spin would be allowed for the strange pentaquark.

Our general strategy is to assume that the decay process proceeds involving the smallest possible angular momentum at the vertices. Therefore, in order to produce the strange pentaquark with $J = 3/2$ it is necessary to implement at least a p-wave contribution in the weak decay mechanism. A p-wave operator of the form

$$T_{\text{tree}}^{\text{p-wave}} = \mathrm{i}B\varepsilon_{ijk}\sigma_k q_i \epsilon_j \tag{4.20}$$

was considered in [126], where it was also shown that, if the peak seen in [40] corresponds to the molecular states with $J^P = 3/2^-$ generated in [35, 36] from the scalar-vector meson interaction in s-wave, the momentum $\vec{q}$ in the former equation must be that of the η-meson, which is taken in the rest frame of the $\eta\Lambda$ system. A decomposition of the p-wave vertex in terms of two operators,

$$\begin{aligned} \hat{S}_{3/2} &= \langle m_\Lambda \mid q_j\epsilon_j + \frac{\mathrm{i}}{2}\varepsilon_{ijk}\sigma_k q_i\epsilon_j \mid m_{\Lambda_b}\rangle \\ \hat{S}_{1/2} &= \langle m_\Lambda \mid q_j\epsilon_j - \mathrm{i}\varepsilon_{ijk}\sigma_k q_i\epsilon_j \mid m_{\Lambda_b}\rangle \ , \end{aligned} \tag{4.21}$$

that project, respectively, over the spin $J = 3/2$ and $J = 1/2$ of the two-body $J/\psi\Lambda$ system, was also given in [126]:

$$T^{\mathrm{p-wave}}_{\mathrm{tree}} = \mathrm{i}B\varepsilon_{ijk}\sigma_k q_i\epsilon_j = \frac{2}{3}B\,\hat{S}_{3/2} - \frac{2}{3}B\,\hat{S}_{1/2}\ . \tag{4.22}$$

The $J = 3/2$ pentaquark will then be generated by the final state interaction of the $J/\psi\Lambda$ pair initiated by the p-wave decay vertex of eq. (4.20), in a process of the type represented by the diagram of Fig. 4.8(c), or also from the virtual excitation of intermediate $\bar{D}^*\eta\Xi_c'$ states followed by multiple interactions leading to $J/\psi\Lambda$ pairs in the final state, as seen in Fig. 4.11(a). Note that in this later case the p-wave decay vertex will have the same structure as that of eq. (4.20), but with a different strength constant, B', and will not act at tree-level.

Considering the s-wave and p-wave contributions, the amplitude that allows for the

appearance of a pentaquark with $J = 3/2$ is then given by:

$$\begin{aligned}
&\mathcal{M}(M_{\eta\Lambda}, M_{J/\psi\Lambda}) = \\
&V_p \left[h_{\eta\Lambda} + \sum_i h_i G_i(M_{\eta\Lambda}) t_{i,\eta\Lambda}(M_{\eta\Lambda}) \right] \langle m_\Lambda \mid \vec{\sigma}\vec{\epsilon} \mid m_{\Lambda_b} \rangle \\
&+\frac{2}{3} B\, \hat{S}_{3/2} - \frac{2}{3} B\, \hat{S}_{1/2} \\
&+\frac{2}{3} B\, G_{J/\psi\Lambda}(M_{J/\psi\Lambda})\, t_{J/\psi\Lambda, J/\psi\Lambda}(M_{J/\psi\Lambda})\, \hat{S}_{3/2} \\
&+\frac{2}{3} B'\, G_{\bar{D}^*\Xi_c'}(M_{\bar{D}^*\Xi_c'})\, t_{\bar{D}^*\Xi_c', J/\psi\Lambda}(M_{J/\psi\Lambda})\, \hat{S}_{3/2} \ ,
\end{aligned} \tag{4.23}$$

where the term proportional to V_p stands for the contribution of the s-wave weak decay amplitude[1], the next row contains the contribution of the p-wave tree level term and the last two rows correspond to the final state interaction contributions that generate the $J = 3/2$ pentaquark initiated by $J/\psi\Lambda$ states (proportional to B) or by $\bar{D}^*\Xi_c'$ states (proportional to B'). The former equation can be cast schematically as:

$$\mathcal{M} = C_1 \langle m_\Lambda \mid \vec{\sigma}\vec{\epsilon} \mid m_{\Lambda_b} \rangle + C_2\, \hat{S}_{3/2} + C_3 \hat{S}_{1/2} \ . \tag{4.24}$$

Finally, the double differential cross-section for the $\Lambda_b \to J/\psi\, \eta\Lambda$ decay process reads [90]:

$$\begin{aligned}
&\frac{d^2\Gamma}{dM_{\eta\Lambda} dM_{J/\psi\Lambda}} = \\
&\frac{1}{(2\pi)^3} \frac{4 M_{\Lambda_b} M_\Lambda}{32 M_{\Lambda_b}^3} \overline{\sum} |\mathcal{M}(M_{\eta\Lambda}, M_{J/\psi\Lambda})|^2 2M_{\eta\Lambda} 2M_{J/\psi\Lambda} \ ,
\end{aligned} \tag{4.25}$$

[1]Note that we have omitted here the contribution of an explicit $\Lambda(2000)$ resonance, since its effect does not bring any qualitative changes in the $J/\psi\Lambda$ pair spectrum, as will be shown in the Results section.

where, after performing the sum over final spins and polarizations and the average over initial spins (see appendix in [126]), one has:

$$\overline{\sum}|\mathcal{M}(M_{\eta\Lambda}, M_{J/\psi\Lambda})|^2 = 3|\mathcal{M}(M_{\eta\Lambda}, M_{J/\psi\Lambda})|^2 \ , \tag{4.26}$$

with $\mathcal{M}$ being that of eqs. (4.18) or (4.19), corresponding to an s-wave weak vertex and, hence, producing a pentaquark with $J = 1/2$, or

$$\overline{\sum}|\mathcal{M}(M_{\eta\Lambda}, M_{J/\psi\Lambda})|^2 = 3|C_1|^2 + \frac{3}{2}\vec{q}^{\,2}|C_2|^2 + 3\vec{q}^{\,2}|C_3|^2 \ , \tag{4.27}$$

with $\mathcal{M}$ being that of eq. (4.23), corresponding to a weak vertex that also has a p-wave term and, hence, making the production of a pentaquark with $J = 3/2$ possible.

Fixing the invariant mass $M_{J/\psi\Lambda}$, one can integrate over $M_{\eta\Lambda}$ in order to obtain $d\Gamma/dM_{J/\psi\Lambda}$. In this case, the limits are given by:

$$\begin{aligned}\left(M^2_{\eta\Lambda}\right)_{\max} &= \left(E^*_\Lambda + E^*_\eta\right)^2 \\ &\quad -\left(\sqrt{E^{*\,2}_\Lambda - M^2_\Lambda} - \sqrt{E^{*\,2}_\eta - m^2_\eta}\right)^2\end{aligned} \tag{4.28}$$

and

$$\begin{aligned}\left(M^2_{\eta\Lambda}\right)_{\min} &= \left(E^*_\Lambda + E^*_\eta\right)^2 \\ &\quad -\left(\sqrt{E^{*\,2}_\Lambda - M^2_\Lambda} + \sqrt{E^{*\,2}_\eta - m^2_\eta}\right)^2 \ ,\end{aligned} \tag{4.29}$$

where

$$E^*_\Lambda = \frac{M^2_{J/\psi\Lambda} - m^2_{J/\psi} + M^2_\Lambda}{2M_{J/\psi\Lambda}} \ , \tag{4.30}$$

$$E^*_\eta = \frac{M^2_{\Lambda_b} - M^2_{J/\psi\Lambda} - m^2_\eta}{2M_{J/\psi\Lambda}} \ . \tag{4.31}$$

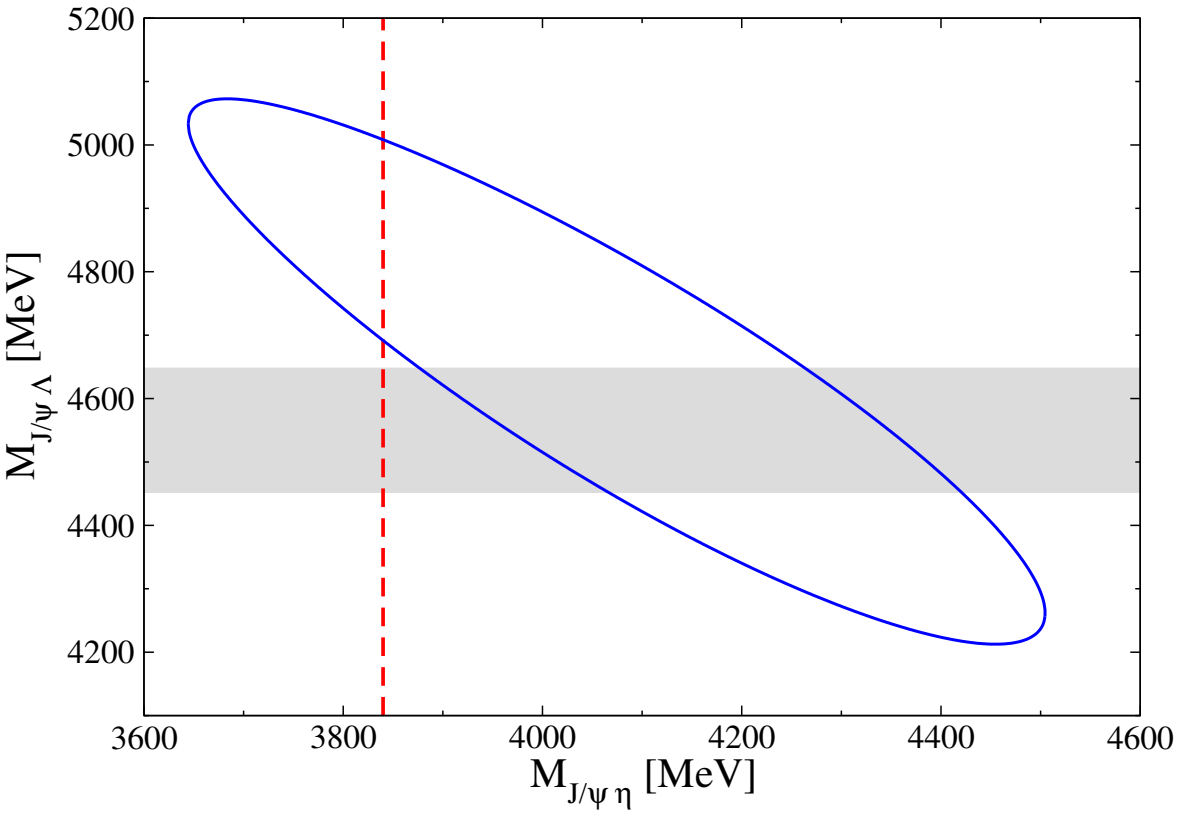

Figure 4.12: Dalitz plot showing the locus of allowed $M_{J/\Psi\Lambda}$, $M_{J/\Psi\,\eta}$ invariant masses in the decay $\Lambda_b \to J/\psi\ \eta\Lambda$. The gray band covers the uncertainties assumed in the present work for the molecular $S = -1$ pentaquark predicted in Refs. [35,36], while the vertical line signals the position of the $J/\Psi\,\eta$ bound state found in the model Ref. [158].

The Dalitz plot showing the allowed final invariant masses covered in the $\Lambda_b \to J/\psi\ \eta\Lambda$ decay is presented in Fig. 4.12. The plot is displayed in terms of the $M_{J/\Psi\Lambda}$ and $M_{J/\Psi\,\eta}$ invariant masses. The value of $M_{\eta\Lambda}$ can straightforwardly be derived from the relation: $M^2_{J/\psi\Lambda} + M^2_{\eta\Lambda} + M^2_{J/\psi\,\eta} = M^2_{\Lambda_b} + M^2_{\Lambda} + m^2_{J/\psi} + m^2_\eta$, which shows that there are only two independent invariant masses. The grey band in the figure covers the uncertainties assumed in the present work for the molecular $S = -1$ pentaquark predicted in Refs. [35,36], while the vertical line signals the position of the $J/\Psi\,\eta$ bound

state found in the model Ref. [158], with quantum numbers $0^-(1^{+-})$, mostly formed from $D^*\bar{D} + c.c.$. We note that such a state, which would be a partner state of the $X(3872)$ with negative C parity and is predicted in some tetra-quark models [159], has not been found experimentally so far. Furthermore, according to Ref. [158], the coupling of this state to $J/\psi\,\eta$ is ten times smaller than that to $D^*\bar{D}+c.c.$. This is more than twice the reduction of a factor four found for the coupling of our pentaquark state to $J/\psi\Lambda$ with respect to $\bar{D}^*\Xi_c'$. However, the main reason for neglecting the $J/\psi\,\eta$ final state interaction, as we do here, is that, even if a resonance which coupled to $J/\psi\,\eta$ existed, there would be no reflection of it in the $J/\psi\Lambda$ mass distribution in our case because the Dalitz plot is not narrow enough. Indeed, we recall that the $J/\psi\Lambda$ mass distribution is obtained by integrating the double differential cross section of eq. (4.25) over $M_{\eta\Lambda}$, which is equivalent to integrating over $M_{J/\psi\,\eta}$ according to what we have mentioned at the begining of this paragraph. Therefore, on inspecting Fig. 4.12, we conclude that the narrow structure in the $M_{J/\psi\,\eta}$ distribution, signaled by the vertical dashed line, will not affect the $M_{J/\psi\Lambda}$ spectrum in the region of the $S = -1$ pentaquark, signaled by the horizontal grey area that accounts for the uncertainties assumed in this work for the $S = -1$ molecular state. The $J/\psi\,\eta$ state would enhance the $M_{J/\psi\Lambda}$ spectrum over a relatively wide range of energies, from 4.7 GeV to 5 GeV, not leaving any clear peaked structure.

Next, we briefly describe the theoretical models employed to obtain the amplitudes $t_{i,\eta\Lambda}$, $t_{J/\psi\Lambda,J/\psi\Lambda}$ and $t_{\bar{D}^*\Xi_c',J/\psi\Lambda}$, which account for the final state interaction effects.

The $S = -1$ meson-baryon amplitude with $\eta\Lambda$ in the final state appearing in diagram (b) of Fig. 4.8 is determined from the coupled-channel unitary **Model 1** and **Model 2** of Sect. 4.1.1 which are referred to **WT+NLO** and **WT+NLO+Born (**η

chan) models widely explained in the second chapter.

With respect to the final state interaction in the $J/\psi\Lambda$ sector, represented by the diagrams of Fig. 4.8(c) and Fig. 4.11(a), we recall that two states with strangeness and hidden charm with $J^P = 3/2^-$ and $I = 0$ were found in Refs. [35, 36] as meson-baryon molecules, having pole positions $\sqrt{s} = 4368 - 2.8\text{i}$ and $\sqrt{s} = 4547 - 6.4\text{i}$ and coupling to $J/\psi\Lambda$ states with strength $\mid g_{J/\psi\Lambda} \mid = 0.47$ and 0.61, respectively. The magnitude of each of these couplings is relatively small compared to the coupling of the pole to the main meson-baryon component, which for the lower energy pole is $\bar{D}^*\Xi_c$, with $\mid g_{\bar{D}^*\Xi_c} \mid = 3.6$, while for the higher energy one is $\bar{D}^*\Xi_c'$, with $\mid g_{\bar{D}^*\Xi_c'} \mid = 2.6$. In either case, $\mid g_{J/\psi\Lambda} \mid$ is large enough to create a peak in the mass distribution, as we shall see. As candidate for the strangeness -1 pentaquark, we will consider the state at higher energy since its mass is close to the non-strange pentaquark found in [40]. One must however accept that the mass obtained for these states has uncertainties since, unlike in other sectors, one does not have any experimental data to constrain the parameters of the theory. We therefore take the nominal value of about $M_R = 4550$ MeV for the mass of the strange pentaquark and will explore the stability of our results to variations of this mass. We shall take $\Gamma_R = 10$ MeV in agreement with the findings of [35, 36]. Our explorations are implemented employing the following Breit-Wigner representation for the $t_{J/\psi\Lambda,J/\psi\Lambda}$ and $t_{\bar{D}^*\Xi_c',J/\psi\Lambda}$ amplitudes

$$t_{J/\psi\Lambda,J/\psi\Lambda} = \frac{g^2_{J/\psi\Lambda}}{M_{J/\psi\Lambda} - M_R + \text{i}\,\frac{\Gamma_R}{2}} \ , \tag{4.32}$$

$$t_{\bar{D}^*\Xi_c',J/\psi\Lambda} = \frac{g_{\bar{D}^*\Xi_c'}\, g_{J/\psi\Lambda}}{M_{J/\psi\Lambda} - M_R + \text{i}\,\frac{\Gamma_R}{2}} \ . \tag{4.33}$$

Then the production of the resonance is done through the $J/\psi\Lambda \to J/\psi\Lambda$ and

$\bar{D}^*\Xi_c' \to J/\psi\Lambda$ amplitudes, parametrized through the expressions given in Eqs. (4.32) and (4.33), as seen in diagrams of Fig. 4.8(c) and Fig. 4.11(a), respectively, as well as in eqs. (4.18), (4.19) or (4.23). The values of the couplings are $g_{J/\psi\Lambda} = -0.61 - 0.06\text{i}$ and $g_{\bar{D}^*\Xi_c'} = 2.61 - 0.13\text{i}$. The loop functions $G_{J/\psi\Lambda}$ and $G_{\bar{D}^*\Xi_c'}$ appearing in these equations are taken from [35, 36], where a dimensional regularization method with a scale $\mu = 1000$ MeV was employed, using subtraction constants $a_{J/\psi\Lambda} = a_{\bar{D}^*\Xi_c'} = -2.3$ (using our convention, $-8.2 \cdot 10^{-3}$).

4.2.2 Results and discussion

We start this section by presenting, in Fig. 4.13, the invariant mass distributions of $J/\psi\Lambda$ and $\eta\Lambda$ states produced in the decay $\Lambda_b \to J/\psi\ \eta\Lambda$, obtained from the simplest s-wave weak decay approach of eq. (4.18) (only the 3 diagrams of Fig. 4.8) and employing **Model 1** (dashed blue line) and **Model 2** (solid black line) for the $S = -1$ $\eta\Lambda$ interaction. For both models, the peak of the pentaquark is clearly seen at 4550 MeV (top panel), the value of the mass M_R employed in the parametrization of eq. (4.32). We can also conclude that this $J/\psi\Lambda$ Breit-Wigner term has a dominant contribution to the scattering amplitude in the resonance region. The invariant mass distribution of $\eta\Lambda$ pairs is shown in the bottom panel of Fig. 4.13, where the $J/\psi\Lambda$ resonant structure has disappeared since the invariant $M_{J/\psi\Lambda}$ masses have been integrated out. The $\eta\Lambda$ invariant mass distributions have essentially the same shape as those already shown in the lower panel of Fig. 4.5, but they are enhanced notably due to the effects of the additional contribution associated with the hidden charm strange pentaquark whose amplitude is significant at 10 MeV above and below the resonance mass $M_R = 4550$ MeV (see the orange band in Fig. 4.14). Note that the enhancement of $\eta\Lambda$ invariant mass

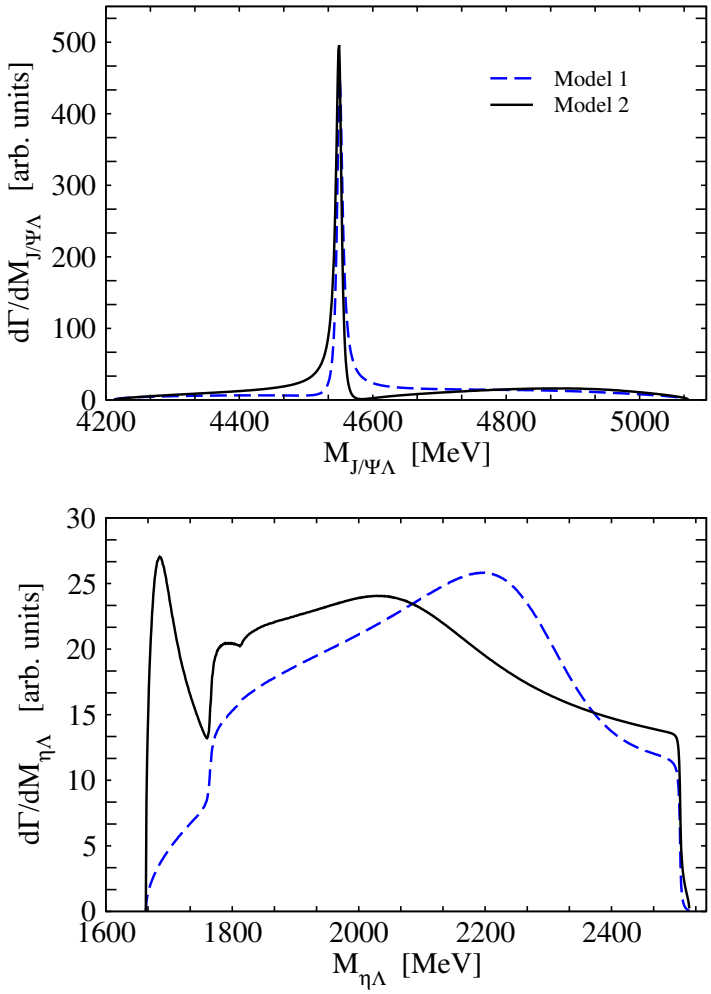

Figure 4.13: Invariant mass distributions of $J/\psi\Lambda$ (top panel) and $\eta\Lambda$ (bottom panel) states produced in the decay $\Lambda_b \to J/\psi\ \eta\Lambda$, obtained for **Model 1** (dashed blue line) and **Model 2** (solid black line).

distributions in Fig. 4.13 is produced just above 1800 MeV which is in accordance with the fact that this orange band overlaps the accessible area for the possible values of the $M_{\eta\Lambda}$ and $M_{J/\psi\Lambda}$ invariant masses, as can be seen in Fig. 4.14.

In the following, results will be presented for only one model of the strong $\eta\Lambda$ interaction, chosen to be **Model 2** as it provides a better overall account of the scattering observables. The $J/\psi\Lambda$ invariant mass distributions displayed in Figs. 4.15 and 4.16,

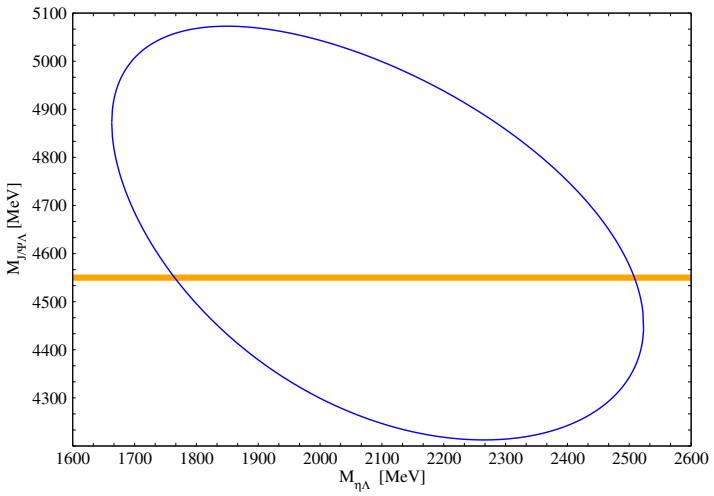

Figure 4.14: Dalitz plot showing the locus of allowed $M_{J/\Psi\Lambda}$, $M_{\eta\Lambda}$ invariant masses in the decay $\Lambda_b \to J/\psi\ \eta\Lambda$. The orange band covers the uncertainties assumed in eq. (4.32) for the molecular $S = -1$ pentaquark, namely $M_R = 4550$ MeV and $\Gamma_R = 10$ MeV.

for different values of the pentaquark coupling to $J/\psi\Lambda$ and for different values of the pentaquark mass, respectively, show obvious trends. From Fig. 4.15 we can conclude that the pentaquark could be seen over the background even if its coupling to $J/\psi\Lambda$ states were as low as $\mid g_{J/\psi\Lambda} \mid = 0.48$. The unitary approaches of Refs. [35–38] predict values for this coupling in between $0.5 - 1.0$, which make us believe that the strange pentaquark could leave a clear signature in the $J/\psi\Lambda$ mass spectrum.

The invariant mass distribution of $\eta\Lambda$ states is not sensitive to the characteristics of the pentaquark, as already noted in the discussion of Fig 4.13. We have checked that changes in either the coupling $\mid g_{J/\psi\Lambda} \mid$ or in the mass M_R do not practically change the aspect of the $\eta\Lambda$ invariant mass spectrum.

In Fig. 4.17 we explore the effect of including the additional effect of a $\Lambda(2000)$ s-wave resonance coupling to $\eta\Lambda$ states. The unknown coupling strength α of eq. (4.19) is varied such that it produces a clearly visible change in the spectrum of $\eta\Lambda$ invariant

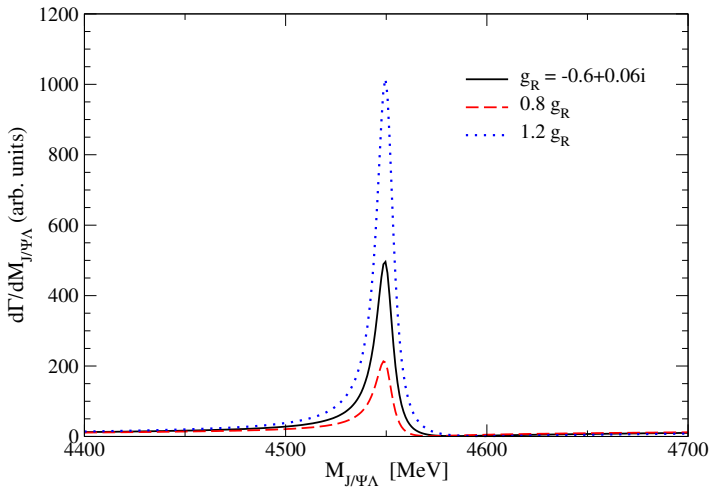

Figure 4.15: Invariant mass distributions of $J/\psi\Lambda$ states produced in the decay $\Lambda_b \to J/\psi\ \eta\Lambda$, obtained for **Model 2** and for different values of the coupling of the pentaquark to $J/\psi\Lambda$.

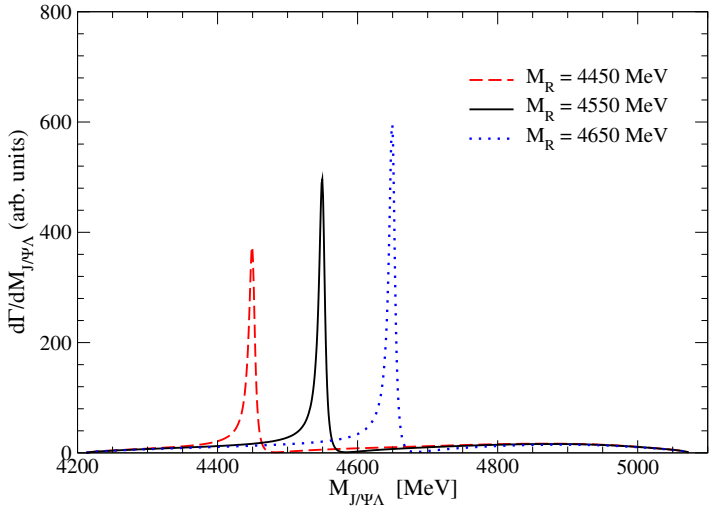

Figure 4.16: Invariant mass distributions of $J/\psi\Lambda$ states produced in the decay $\Lambda_b \to J/\psi\ \eta\Lambda$, obtained for **Model 2** and for different values of the pentaquark mass states.

masses with respect to what we obtain in the absence of this contribution, as seen in the bottom panel of Fig. 4.17. In the top panel we observe that the inclusion of the $\Lambda(2000)$ on the $J/\psi\Lambda$ pair distribution, where the $\eta\Lambda$ invariant masses have been integrated out, essentially enhances the strength while keeping the same shape for the

different values of α.

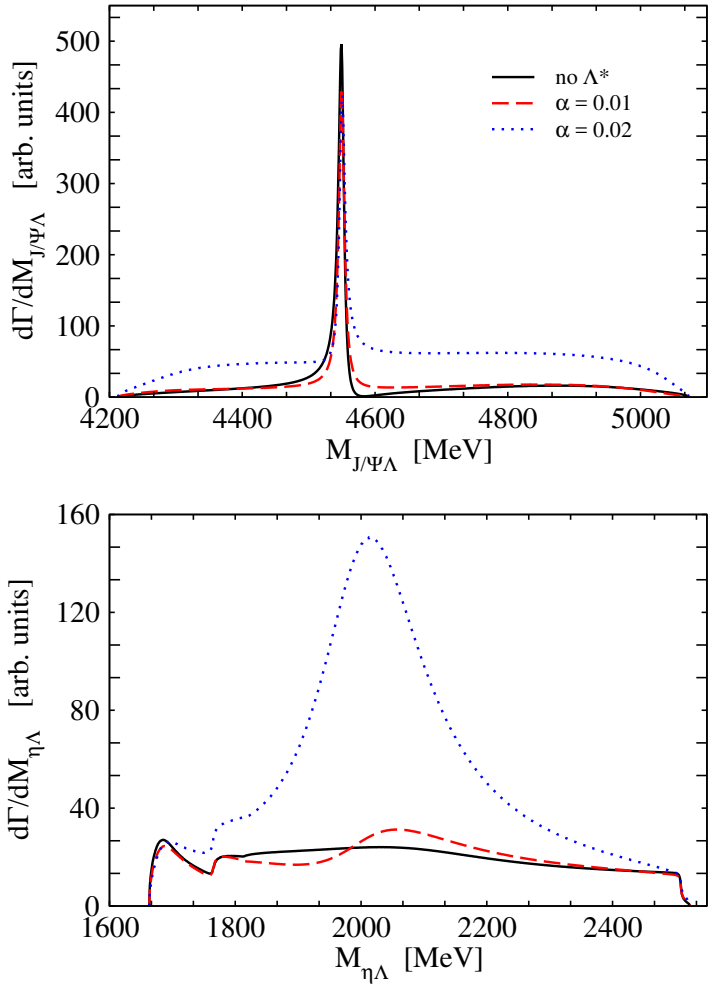

Figure 4.17: Invariant mass distributions of $J/\psi\Lambda$ (top panel) and $\eta\Lambda$ (bottom panel) states produced in the decay $\Lambda_b \to J/\psi\ \eta\Lambda$, obtained from **Model 2**, assuming a pentaquark of $J^P = 1/2^-$ and different strengths of the $\Lambda(2000)$ resonant contribution.

We next explored the influence of the strange pentaquark being initiated by the excitation of a virtual $\bar{D}^{*0}\eta\Xi_c'$ state, followed by the multiple scattering of $\bar{D}^{*0}\Xi_c'$ leading to a final $J/\psi\Lambda$ pair and an η meson. As discussed in the previous section, the topology for this decay should lead to a reduced amplitude with respect to that of the $J/\psi\,\eta\Lambda$ case. We implement this phenomenologically through the parameter β, as seen in

eq. (4.19), which is given the values $-0.5, -0.25, 0.0, 0.25$, and 0.5 accounting also for different relative sign cases. The results obtained with the negative values are displayed in Fig. 4.18 and those with the positive values in Fig. 4.19. In all the cases, the

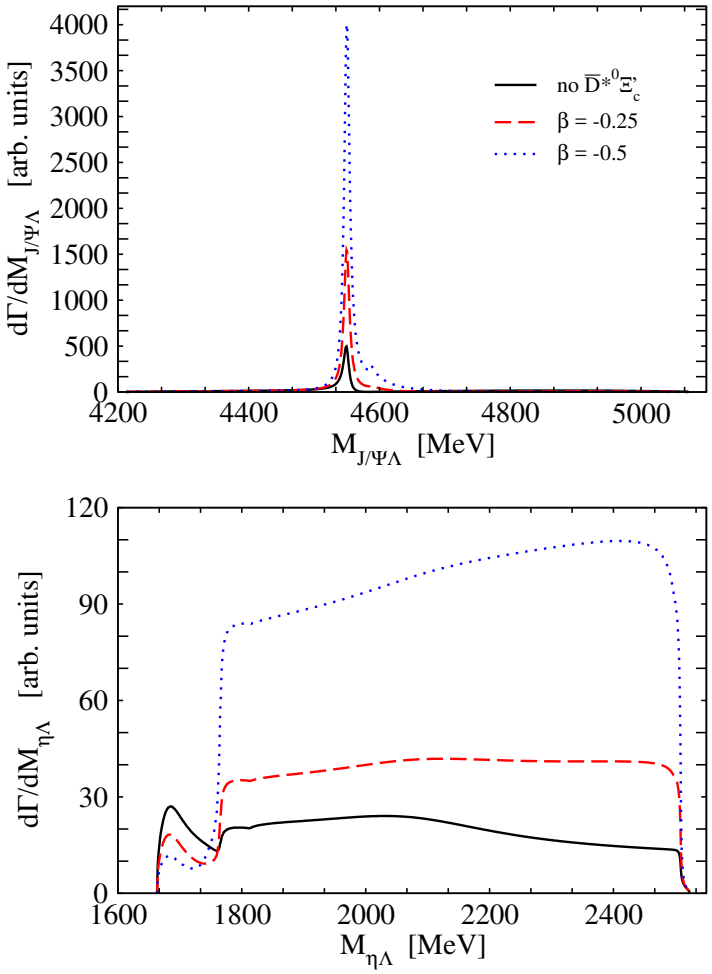

Figure 4.18: Invariant mass distributions of $J/\psi\Lambda$ (top panel) and $\eta\Lambda$ (bottom panel) states produced in the decay $\Lambda_b \to J/\psi\ \eta\Lambda$, obtained from **Model 2**, assuming a pentaquark of $J^P = 1/2^-$ and different strengths of the $\bar{D}^{*0}\Xi_c'$ intermediate state contribution.

pentaquark signal, seen in the $J/\psi\Lambda$ invariant mass distribution (top panels), clearly dominates over the background; for the negative values of β the signal is enhanced more strongly due to a constructive interference between both mechanisms of the pentaquark

production, since $g_{J/\psi\Lambda}$ and $g_{\bar{D}^*\Xi_c'}$ have opposite signs. Conversely, for the positive values of β, we have destructive interference between these two mechanisms responsible for the pentaquark production. It can also be concluded from Figs. 4.18 and 4.19 that the $\bar{D}^*\Xi_c'$ mechanism dominates over the $J/\psi\Lambda$ one. This fact is reflected on the $\eta\Lambda$ invariant mass distributions of the bottom panels in Figs. 4.18 and 4.19 which show a tremendous enhancement accounting for the new contributions to the pentaquark production.

Up to here, we have been discussing the results assuming the pentaquark to have $J^P = 1/2^-$, which can then be produced by an s-wave mechanism for the Λ_b decay. In the case of a $J^P = 3/2^-$ pentaquark, which is another of the possibilities for the states predicted in [35, 36], it is necessary to implement at least an additional p-wave contribution, as in eq. (4.20). Our results for this case are displayed in Fig. 4.20. The dotted line represents the case in which only the s-wave contribution is kept, producing a $J/\psi\Lambda$ pair in $1/2^-$. Since the pentaquark is now assumed to have $J^P = 3/2^-$, it does not show in that $J/\psi\Lambda$ invariant mass spectrum, which reduces to a structureless background. We could have included, as in the study of the $J = 1/2$ pentaquark case, the $\Lambda(2000)$ s-wave resonance contribution, but we have omitted this effect in the present $J = 3/2$ discussion because, although it would be seen as an additional structure in the $\eta\Lambda$ invariant mass distribution, it would simply contribute a practically constant strength to the spectrum of $J/\psi\Lambda$ pairs, similarly to what we have found in Fig. 4.17.

When we add the p-wave vertex of eq. (4.20), we obtain the distributions displayed by the dashed curves in Fig. 4.20. The size of the coupling constant, $B = 0.001$ MeV^{-1}, has been chosen so that the p-wave contribution has a visible effect over the

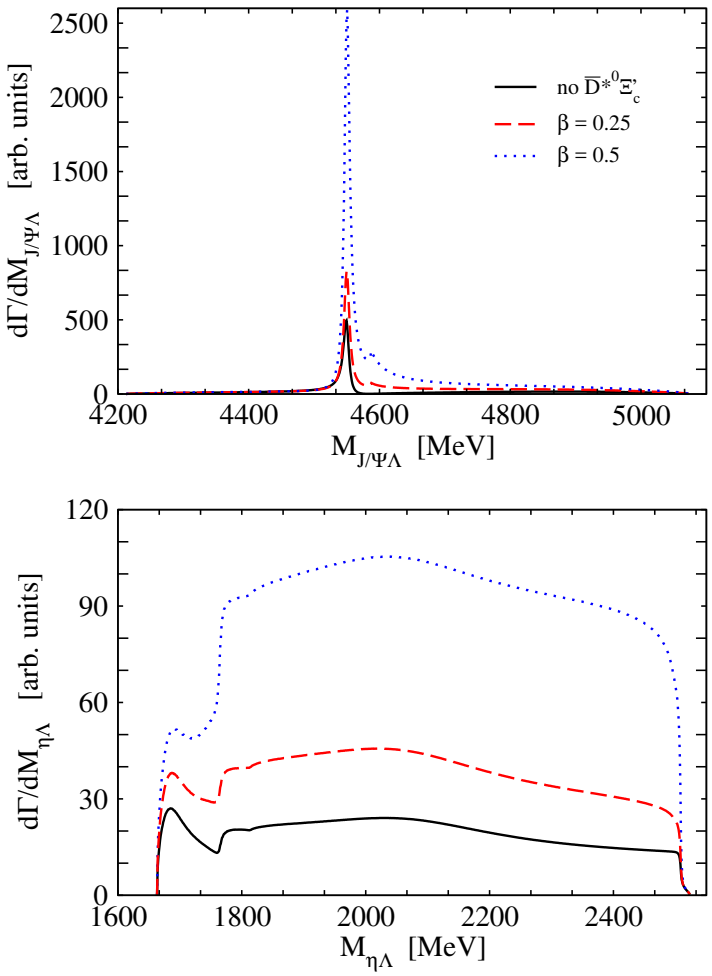

Figure 4.19: Invariant mass distributions of $J/\psi\Lambda$ (top panel) and $\eta\Lambda$ (bottom panel) states produced in the decay $\Lambda_b \to J/\psi\ \eta\Lambda$, obtained from **Model 2**, assuming a pentaquark of $J^P = 1/2^-$ and different strengths of the $\bar{D}^{*0}\Xi_c'$ intermediate state contribution.

s-wave $J/\psi\Lambda$ and $\eta\Lambda$ invariant mass distributions. The $J/\psi\Lambda$ spectrum, shown in the top panel of Fig. 4.20, presents a dip at the pentaquak mass, which comes from the interference between the tree level and the $J/\psi\Lambda$ final state interaction terms, displayed by Figs. 4.8(a) and (c), respectively, as can also be seen in eq. (4.23). This is the same behaviour as that observed in the study of the strange pentaquark from the $\Lambda_b \to J/\psi K^0\Lambda$ decay in [126]. In the present work, we also incorporate the excitation

of the pentaquark from the multiple scattering of $\bar{D}^{*0}\Xi_c'$ pairs produced in the virtual $\Lambda_b \to \bar{D}^{*0}\eta\Xi_c'$ decay, which proceeds also in p-wave with a strength B'. This is a necessary consideration if one wants to interpret the pentaquark as the state emerging from the interaction of $\bar{D}^{*0}\Xi_c'$ and its related coupled states. If we now assume a ratio between the $\Lambda_b \to \bar{D}^{*0}\eta\Xi_c'$ and $\Lambda_b \to J/\psi\,\eta\Lambda$ amplitudes of $B'/B = 0.5$, we obtain the solid curve, where the dip has turned into a wiggly shape. When the sign of B' is opposed to that of B, we find a similar behaviour, although in a reflected way, as depicted by the dot-dashed curve. In either case, a visible pentaquark signal is obtained.

With all the options and uncertainties considered, we see that the existence of the molecular state predicted in Refs. [35, 36] leads to a clear signal in the $J/\psi\Lambda$ invariant mass spectrum in the range of about 4450-4650 MeV. If a signal was seen outside this range its explanation within the molecular picture would be highly questionable. On the other hand, the non observation of a signal would indicate that the pentaquark state does not exist, or that its coupling to $J/\psi\Lambda$ is significantly smaller than what was determined in the model of [35, 36], in either case questioning the validity of this model.

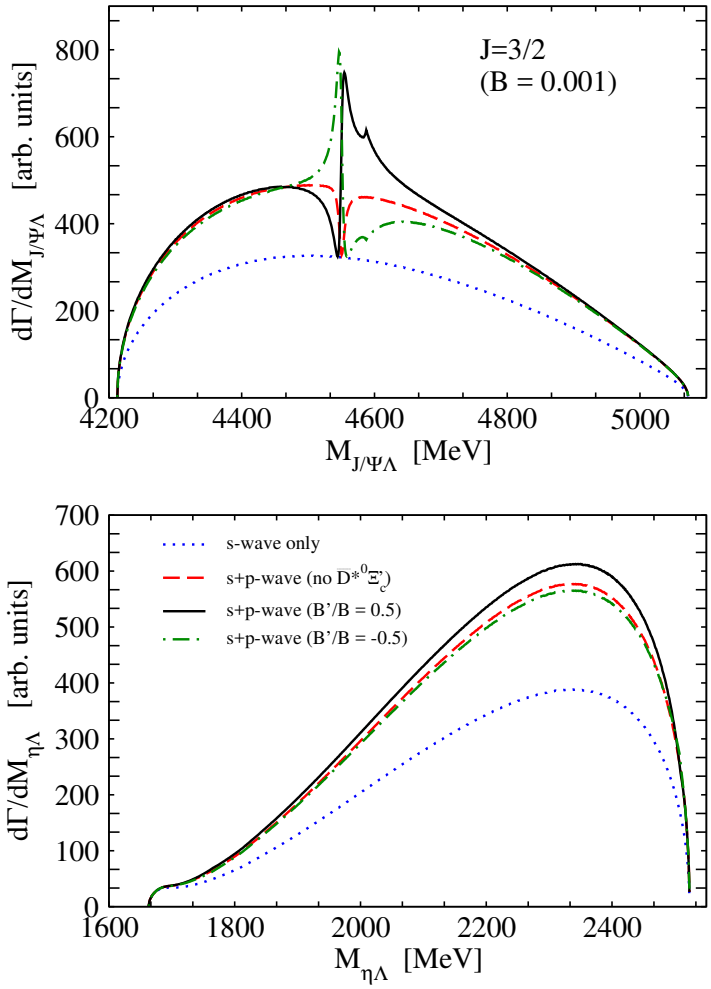

Figure 4.20: Invariant mass distributions of $J/\psi\Lambda$ (top panel) and $\eta\Lambda$ (bottom panel) states produced in the decay $\Lambda_b \to J/\psi\ \eta\Lambda$, obtained from **Model 2**, assuming a pentaquark of $J^P = 3/2^-$. The dotted line is obtained with only an s-wave weak decay vertex, the dashed line also contains a p-wave contribution with $B = 0.001$ MeV^{-1}, and the solid and dot-dashed line implement the additional contribution of the $\bar{D}^{*0}\Xi_c'$ intermediate state with $B'/B = 0.5$ and $B'/B = -0.5$ respectively.

Conclusions

The purpose of this thesis has been to study the $S = -1$ meson-baryon interaction in s-wave employing an effective chiral $SU(3)$ lagrangian up to NLO and implementing unitarization in coupled channels. Such a study requires fixing the NLO coefficients of the lagrangian which are not well established yet.

In general, the low energy constants of an effective lagrangian are obtained from fitting procedures to the experimental available data. These parameters have been constrained to a large set of experimental K^-p scattering data into $\pi\Sigma, \bar{K}N, \pi\Lambda$ channels, to γ, R_n and R_c branching ratios, and to the precise SIDDHARTA value of the energy shift and width of kaonic hydrogen. The novelty of our work is the inclusion of the scattering data from $K^-p \to K^+\Xi^-, K^0\Xi^0$ reactions in the fitting procedure, since these reactions become especially sensitive to higher order terms, as they cannot proceed with the WT term of the lagrangian, except indirectly via unitarization contributions. We have paid special attention to the effects that a systematic inclusion in the lagrangian of the NLO and Born terms has on the low energy constants, particularly

on the NLO coefficients.

The main difference among the models we get from the fits is reflected in the isospin components of the total cross sections of the reactions we study. To check the reliability of these models, we have performed new fits which take into account data from isospin filtering reactions. The stability and accuracy of the parameters have been tested by including phenomenological resonant contributions to the scattering amplitudes of the reactions that are especially sensitive to the NLO corrections. These resonant terms have been useful to reach better agreement with the experimental data.

In order to explore other processes that take place at higher energies and which can provide more information of the NLO parameters, we have studied the Λ_b decay into states containing a J/Ψ and meson-baryon pairs. Furthermore, the $\Lambda_b \to J/\psi\eta\Lambda$ process has allowed us to study the implications of observing a possible strange partner of the hidden charm pentaquark state $P_c(4450)$. The conclusions and analysis of each chapter are summarized below.

Chapter 2 is devoted to studying the role played by NLO and Born terms, as well as the relevance of certain reactions in obtaining a more reliable parametrization for the NLO coefficients.

We started by comparing different fitting procedures consisting of unitarized calculations employing a kernel in which we include or not the NLO term and which take into account or not the scattering data of the $K^- p \to K\Xi$ reactions. From the results of all these combinations, and particularly from the successful reproduction of the experimental data reached by the **WT+NLO** model, we have shown for the first time that the NLO order terms of the chiral Lagrangian are absolutely necessary to repro-

duce the $K^-p \to K\Xi$ reaction data. In this way, the sensitivity of the NLO lagrangian to the $K^-p \to K\Xi$ reactions has been clearly established. Given this sensitivity and the fact that the existing $K^-p \to K\Xi$ scattering data is limited and suffers from large uncertainties, more accurate data is required before giving a more definitive answer about the values of the NLO coefficients.

Next, contrary to the assumption we made about the little effect of the Born terms in the earlier stage which was supported by studies of other groups, we have proved that they become non-negligible in the $K^-p \to K\Xi$ reactions. The parametrization of the new fit (**WT+NLO+Born**) led to significant changes in the NLO coefficients compared to those of the **WT+NLO** model. Despite this, we do not get any improvement either in accuracy of the parameters nor in the $\chi^2_{\text{d.o.f.}}$. This fact has led us to an interesting finding that allows us to understand how such different parametrizations could give such a similar agreement with the experimental data: the inclusion or non inclusion of the Born terms can seriously modify the isospin decomposition of the $K^-p \to K\Xi$ cross sections due to their sensitivity to the higher order terms. Such differences in the isospin components point to the need for constraining the models with experimental data from reactions that proceed through $I = 0$ or $I = 1$, thus providing more reliable parameters of the meson-baryon lagrangian.

Most of the data employed in our fits is coming from antikaon proton scattering and therefore contain contributions from both isospin $I = 0$ and $I = 1$ components; the only exception is the $\pi^0\Sigma^0$ channel, which selects $I = 0$. We then widened the number of experimental observables used in the fits including scattering data from $K^-p \to \eta\Lambda, \eta\Sigma^0$ reactions, which are of pure isospin 0 and 1 respectively. These efforts culminated in the **WT+NLO+Born (η chan)** model that, as far as we know, is

the only chiral model in the literature which reproduces K^-p scattering data into all possible $S = -1$ channels with good agreement. Regarding the parametrization related to this model, the inclusion of this new experimental data has been crucial for obtaining a very homogeneous and accurate set of NLO coefficients, as well as natural sized values for all the subtraction constants. This leads us to think that the inclusion of more experimental data from isospin filtering processes could favour more reliable values for the low energy constants.

The proposed measurement of the $K_L^0 p \to K^+\Xi^0$ reactions in $I = 1$ with a secondary K_L^0 beam at Jlab would complement the information one can obtain from K^-p scattering data to constrain the theoretical models. We have presented our prediction for this reaction employing some of our models, concluding that, as more contributions are taken into account in the interaction kernel and more data is included in the fit, the predicted values are closer to the only two available experimental points of this reaction. Neither of these two data points have been used in any fitting procedure. This prediction seems to confirm the reliability of our parametrizations, particularly the **WT+NLO+Born (η chan)** one, which we consider our best pure chiral model.

In order to improve the description of the experimental $K^-p \to K\Xi$ and $K^-p \to \eta\Lambda$ scattering data, it is also possible to consider the inclusion of high-spin resonaces in such processes. Since they are the most sensitive reactions to the NLO terms, this could also lead to modifications of the NLO parameters. In this way, we can study the stability and accuracy of the parameters present in the models. This is performed in the third chapter of this thesis.

We first allowed for the explicit contribution of the high spin hyperon resonances $\Sigma(2030)$ and $\Sigma(2250)$ to the $K^-p \to K\Xi$ amplitudes, aiming at establishing an ap-

propriate amount for the background, which in this work is associated to the chiral contributions, and, hence, obtaining more reliable values of the associated low energy constants. The resonant amplitude has been calculated by applying the Rarita-Schwinger method while the chiral amplitude has been obtained employing a lagrangian with a WT and NLO contribution giving rise to the **NLO+RES** model. Since the resonant terms introduce an angular dependence in the amplitudes, we also attempted the description of the $K\Xi$ differential cross sections. We find the resonant terms to have a double benefit. On the one hand, they allow for a reasonable overall description of the scattering data, including the total and the differential cross sections of the $K\Xi$ production reactions. On the other hand, by absorbing certain structures of the cross section, the inclusion of resonant contributions permits finding a more stable solution and therefore more precise values of the low energy constants of the chiral unitary model.

Then, we performed a similar study for **WT+NLO+Born (η chan)** model, which we consider our best chiral model. In contrast to the study carried out previously, this model has been constrained with additional data ($K^-p \to \eta\Lambda$ cross section data), meaning that, since the $K^-p \to \eta\Lambda$ reaction is also very senstive to the NLO terms, the corresponding NLO coefficients are more reliable. This makes the analysis of stability acquire a more decisive character. Aiming for this, we extended the resonant contributions to the $K^-p \to \eta\Lambda$ process, particularly we have taken into account the contribution of the $\Lambda(1890)$ resonance which has also been incorporated into the $K^-p \to K\Xi$ amplitudes, in addition to the $\Sigma(2030)$ and $\Sigma(2250)$ resonances. The results obtained confirm the previous findings: there is a notable improvement of the agreement with the experimental data and the parameters take similar values to the ones corresponding to the model without resonances. This stability is specially marked

for most of the NLO coefficients.

Having proved the effects of the isospin filtering processes on the NLO coefficients, in Chapter 4 we have shown that the $\Lambda_b \to J/\psi\ \eta\Lambda$ decay and, particularly, the $\Lambda_b \to J/\psi\ K\Xi$ one provide very valuable information concerning the meson-baryon interaction in the $S = -1$ and isospin $I = 0$ sector. The dynamics of the reaction, where the light quarks of the Λ_b play a spectator role, is such that it filters $I = 0$ in the final state. This is so because the ud quarks in the Λ_b baryon necessarily couple to $I = 0$ and the weak decay favours the $b \to c\bar{c}s$ transition, so there is an s-quark at the end of the weak process, which together with the ud pair in $I = 0$ gives a total isospin $I = 0$. Thus, these decays may offer complementary information to that obtained from $K^-p \to K\Xi$ scattering data, where both $I = 0$ and $I = 1$ contributions combine to give the final results.

Our study is based on the models **WT+NLO** (**Model 1**) and **WT+NLO+Born (η chan)** (**Model 2**) developed in this thesis to describe the K^-p scattering. Both models produce quite different invariant mass distributions for the decay of the Λ_b into $K\Xi$ and $\eta\Lambda$ states, which are also in turn quite different from phase space, indicating the sensitivity of these processes to the strong internal dynamics. The differences between models are more visible in the $\Lambda_b \to J/\psi\ K\Xi$ decay process. The reason stems from the fact that the decay into $\eta\Lambda$ can proceed at tree level, while the selectivity of the Λ_b decay processes producing the J/ψ does not allow the formation of a $K\Xi$ pair in a primary step. This is only produced through rescattering of the $\bar{K}N$ and $\eta\Lambda$ primary components. Thus the $\Lambda_b \to J/\psi\ K\Xi$ reaction is directly proportional to the meson-baryon scattering amplitude, concretely to the $\eta\Lambda \to K\Xi$ and $\bar{K}N \to K\Xi$ components in $I = 0$, which can lead to a marked pattern of interferences. These

models also predict sizable differences for the Λ_b decay in the energy region of $K\Xi$ and $\eta\Lambda$ production, reflecting that the $I = 0$ component of the meson-baryon interaction, which is the one playing a role in the Λ_b decay processes studied here, is not very well constrained by the fitting to $K^- p \to K\Xi$ data.

The recent finding of two structures in the $J/\psi p$ invariant mass distribution of the $\Lambda_b \to J/\psi K^- p$ decay, associated to two pentaquark states, together with its plausible explanation in terms of a previously predicted hidden charm baryon molecular state, prompted us to study the decay of the Λ_b into $J/\psi\,\eta\Lambda$ final states. The $\Lambda_b \to J/\psi\,\eta\Lambda$ decay will occur with similar strength as the $\Lambda_b \to J/\psi K^- p$ one, and one could observe, in the $J/\psi\Lambda$ invariant mass spectrum, possible strange partners of the two non-strange pentaquark states reported by the LHCb collaboration. We recall that when the hidden charm N^* resonances were theoretically predicted as molecular states in several unitary approaches, some partner hidden charm strange Λ^* states were also found. We have taken advantage of this finding and have predicted what signal one of these state should leave in the $\eta\Lambda$ and $J/\psi\Lambda$ invariant mass distributions of the $\Lambda_b \to J/\psi\,\eta\Lambda$ reaction. We have found that, taking the values of the couplings of the hidden charm Λ^* state to the $\bar{D}^{*0}\Xi_c'$ and $J/\psi\Lambda$ channels obtained in the unitary approaches, one should observe clear and sizable peaks in the $J/\psi\Lambda$ mass distribution of the $\Lambda_b \to J/\psi\,\eta\Lambda$ decay. We have studied the dependence of our results on reasonable changes in the parameters of the models involved in our description of the process, as well as on the unknown properties of the speculated hidden charm strange pentaquark. We have observed that, while changes appear in the position of the peak and in the shapes of the distributions, a resonance signal in the $J/\psi\Lambda$ invariant mass spectrum is clearly seen in all the cases. This gives us confidence that such an experiment should result in successful proof of the existence of this new state and we encourage the experimental analysis of this

decay channel, for which our theoretical study predicts a similar strength than for the $\Lambda_b \to J/\psi K^- p$ reaction already analyzed by LHCb.

The present work is our first step toward building a more complete chiral model in $S = -1$ sector to help analyze the forthcoming more precise data in the $K\Xi$ production. In addition, the findings and the features observed in this study indicate that the actual measure of the complementary observables analyzed here would provide valuable information, novel so far, that would enrich our knowledge of the meson-baryon interaction and help us make progress in our understanding of hadron dynamics.

Appendix A: Coupling coefficients

Table 4.1 presents the C_{ij} coefficients of eq. (1.59), while Table 4.2 presents the D_{ij}, L_{ij} coefficients of eq. (1.65). These three sets of Clebsch-Gordan-type coefficients are symmetric under the interchange of initial and final meson-baryon pairs.

	K^-p	$\bar{K}^0n$	$\pi^0\Lambda$	$\pi^0\Sigma^0$	$\eta\Lambda$	$\eta\Sigma^0$	$\pi^+\Sigma^-$	$\pi^-\Sigma^+$	$K^+\Xi^-$	$K^0\Xi^0$
K^-p	2	1	$\sqrt{3}/2$	1/2	3/2	$\sqrt{3}/2$	0	1	0	0
$\bar{K}^0n$		2	$-\sqrt{3}/2$	1/2	3/2	$-\sqrt{3}/2$	1	0	0	0
$\pi^0\Lambda$			0	0	0	0	0	0	$\sqrt{3}/2$	$-\sqrt{3}/2$
$\pi^0\Sigma^0$				0	0	0	2	2	1/2	1/2
$\eta\Lambda$					0	0	0	0	3/2	3/2
$\eta\Sigma^0$						0	0	0	$\sqrt{3}/2$	$-\sqrt{3}/2$
$\pi^+\Sigma^-$							2	0	1	0
$\pi^-\Sigma^+$								2	0	1
$K^+\Xi^-$									2	1
$K^0\Xi^0$										2

Table 4.1: C_{ij} coefficients of Eq. (1.59).

In addition, the fourth set of Clebsch-Gordan coefficients present in the direct and cross Born contributions to the interaction kernel, eqs. (1.61) and (1.62), are given by the following relations extracted from [15], but we should keep in mind a remark concerning their symmetry under the combined transformation $B_1 \leftrightarrow B_2$ and $\phi \leftrightarrow \bar{\phi}$. In other words, $C^{(\mathrm{Born})}_{\bar{\phi}B_1,B_2} = C^{(\mathrm{Born})}_{\phi B_2,B_1}$, for instance, $C^{(\mathrm{Born})}_{\bar{K}^0 n,\Lambda} = C^{(\mathrm{Born})}_{K^0\Lambda,n}$.

$$C^{(\mathrm{Born})}_{K^- p,\Lambda} = C^{(\mathrm{Born})}_{\bar{K}^0 n,\Lambda} = C^{(\mathrm{Born})}_{\eta\Xi^-,\Xi^-} = C^{(\mathrm{Born})}_{\eta\Xi^0,\Xi^0} = -D - 3F,$$

$$\sqrt{2}C^{(\mathrm{Born})}_{K^- p,\Sigma^0} = -\sqrt{2}C^{(\mathrm{Born})}_{\bar{K}^0 n,\Sigma^0} = C^{(\mathrm{Born})}_{\bar{K}^0 p,\Sigma^+} = C^{(\mathrm{Born})}_{K^- n,\Sigma^-} = C^{(\mathrm{Born})}_{\pi^+\Xi^-,\Xi^0}$$
$$= \sqrt{2}C^{(\mathrm{Born})}_{\pi^0\Xi^-,\Xi^-} = -\sqrt{2}C^{(\mathrm{Born})}_{\pi^0\Xi^0,\Xi^0} = \sqrt{6}(D - F),$$

$$C^{(\mathrm{Born})}_{\pi^0\Sigma^0,\Lambda} = C^{(\mathrm{Born})}_{\pi^+\Sigma^-,\Lambda} = C^{(\mathrm{Born})}_{\pi^-\Sigma^+,\Lambda} = C^{(\mathrm{Born})}_{\eta\Sigma^+,\Sigma^+} = C^{(\mathrm{Born})}_{\eta\Sigma^-,\Sigma^-}$$
$$= C^{(\mathrm{Born})}_{\eta\Sigma^0,\Sigma^0} = -C^{(\mathrm{Born})}_{\eta\Lambda,\Lambda} = 2D,$$

$$C^{(\mathrm{Born})}_{\pi^+\Sigma^-,\Sigma^0} = -C^{(\mathrm{Born})}_{\pi^-\Sigma^+,\Sigma^0} = -C^{(\mathrm{Born})}_{\pi^0\Sigma^-,\Sigma^-} = C^{(\mathrm{Born})}_{\pi^0\Sigma^+,\Sigma^+} = 2\sqrt{3}F,$$

$$C^{(\mathrm{Born})}_{K^+\Xi^-,\Lambda} = C^{(\mathrm{Born})}_{K^0\Xi^0,\Lambda} = C^{(\mathrm{Born})}_{\eta p,p} = C^{(\mathrm{Born})}_{\eta n,n} = -D + 3F,$$

$$\sqrt{2}C^{(\mathrm{Born})}_{K^+\Xi^-,\Sigma^0} = -\sqrt{2}C^{(\mathrm{Born})}_{K^0\Xi^0,\Sigma^0} = C^{(\mathrm{Born})}_{\pi^- p,n} = \sqrt{2}C^{(\mathrm{Born})}_{\pi^0 p,p} = -\sqrt{2}C^{(\mathrm{Born})}_{\pi^0 n,n}$$
$$= C^{(\mathrm{Born})}_{\bar{K}^0\Sigma^-,\Xi^-} = C^{(\mathrm{Born})}_{K^-\Sigma^+,\Xi^0} = \sqrt{6}(D + F). \tag{A.1}$$

D_{ij} coefficients

	K^-p	$\bar{K}^0n$	$\pi^0\Lambda$	$\pi^0\Sigma^0$	$\eta\Lambda$	$\eta\Sigma^0$	$\pi^+\Sigma^-$	$\pi^-\Sigma^+$	$K^+\Xi^-$	$K^0\Xi^0$
K^-p	$4(b_0+b_D)m_K^2$	$2(b_D+b_F)m_K^2$	$\frac{-(b_D+3b_F)\mu_2^2}{2\sqrt{3}}$	$\frac{(b_D-b_F)\mu_1^2}{2}$	$\frac{(b_D+3b_F)\mu_2^2}{6}$	$\frac{-(b_D-b_F)\mu_2^2}{2\sqrt{3}}$	0	$(b_D-b_F)\mu_1^2$	0	0
$\bar{K}^0n$		$4(b_0+b_D)m_K^2$	$\frac{(b_D+3b_F)\mu_1^2}{2\sqrt{3}}$	$\frac{(b_D-b_F)\mu_1^2}{2}$	$\frac{(b_D+3b_F)\mu_2^2}{6}$	$\frac{(b_D-b_F)\mu_2^2}{2\sqrt{3}}$	$(b_D-b_F)\mu_1^2$	0	0	0
$\pi^0\Lambda$			$\frac{4(3b_0+b_D)m_\pi^2}{3}$	0	0	$\frac{4b_Dm_\pi^2}{3}$	0	0	$\frac{-(b_D-3b_F)\mu_1^2}{2\sqrt{3}}$	$\frac{(b_D-3b_F)\mu_1^2}{2\sqrt{3}}$
$\pi^0\Sigma^0$				$4(b_0+b_D)m_\pi^2$	$\frac{4b_Dm_\pi^2}{3}$	0	0	0	$\frac{(b_D+b_F)\mu_1^2}{2}$	$\frac{(b_D+b_F)\mu_1^2}{2}$
$\eta\Lambda$					$\frac{4(3b_0\mu_3^2+b_D\mu_4^2)}{9}$	0	$\frac{4b_Dm_\pi^2}{3}$	$\frac{4b_Dm_\pi^2}{3}$	$\frac{(b_D-3b_F)\mu_2^2}{6}$	$\frac{(b_D-3b_F)\mu_2^2}{6}$
$\eta\Sigma^0$						$\frac{4(b_0\mu_3^2+b_Dm_\pi^2)}{3}$	$\frac{4b_Fm_\pi^2}{\sqrt{3}}$	$\frac{-4b_Fm_\pi^2}{\sqrt{3}}$	$\frac{-(b_D+b_F)\mu_2^2}{2\sqrt{3}}$	$\frac{(b_D+b_F)\mu_2^2}{2\sqrt{3}}$
$\pi^+\Sigma^-$							$4(b_0+b_D)m_\pi^2$	0	$(b_D+b_F)\mu_1^2$	0
$\pi^-\Sigma^+$								$4(b_0+b_D)m_\pi^2$	0	$(b_D+b_F)\mu_1^2$
$K^+\Xi^-$									$4(b_0+b_D)m_K^2$	$2(b_D-b_F)m_K^2$
$K^0\Xi^0$										$4(b_0+b_D)m_K^2$

L_{ij} coefficients

	K^-p	$\bar{K}^0n$	$\pi^0\Lambda$	$\pi^0\Sigma^0$	$\eta\Lambda$	$\eta\Sigma^0$	$\pi^+\Sigma^-$	$\pi^-\Sigma^+$	$K^+\Xi^-$	$K^0\Xi^0$
K^-p	$2d_2+d_3+2d_4$	$d_1+d_2+d_3$	$\frac{-\sqrt{3}(d_1+d_2)}{2}$	$\frac{-d_1-d_2+2d_3}{2}$	$\frac{d_1-3d_2+2d_3}{2}$	$\frac{d_1-3d_2}{2\sqrt{3}}$	$-2d_2+d_3$	$-d_1+d_2+d_3$	$-4d_2+2d_3$	$-2d_2+d_3$
$\bar{K}^0n$		$2d_2+d_3+2d_4$	$\frac{\sqrt{3}(d_1+d_2)}{2}$	$\frac{-d_1-d_2+2d_3}{2}$	$\frac{d_1-3d_2+2d_3}{2}$	$\frac{-(d_1-3d_2)}{2\sqrt{3}}$	$-d_1+d_2+d_3$	$-2d_2+d_3$	$-2d_2+d_3$	$-4d_2+2d_3$
$\pi^0\Lambda$			$2d_4$	0	0	d_3	0	0	$\frac{\sqrt{3}(d_1-d_2)}{2}$	$\frac{-\sqrt{3}(d_1-d_2)}{2}$
$\pi^0\Sigma^0$				$2(d_3+d_4)$	d_3	0	$-2d_2+d_3$	$-2d_2+d_3$	$\frac{d_1-d_2+2d_3}{2}$	$\frac{d_1-d_2+2d_3}{2}$
$\eta\Lambda$					$2(d_3+d_4)$	0	d_3	d_3	$\frac{-d_1-3d_2+2d_3}{2}$	$\frac{-d_1-3d_2+2d_3}{2}$
$\eta\Sigma^0$						$2d_4$	$\frac{2d_1}{\sqrt{3}}$	$\frac{-2d_1}{\sqrt{3}}$	$\frac{-(d_1+3d_2)}{2\sqrt{3}}$	$\frac{d_1+3d_2}{2\sqrt{3}}$
$\pi^+\Sigma^-$							$2d_2+d_3+2d_4$	$-4d_2+2d_3$	$d_1+d_2+d_3$	$-2d_2+d_3$
$\pi^-\Sigma^+$								$2d_2+d_3+2d_4$	$-2d_2+d_3$	$d_1+d_2+d_3$
$K^+\Xi^-$									$2d_2+d_3+2d_4$	$-d_1+d_2+d_3$
$K^0\Xi^0$										$2d_2+d_3+2d_4$

Table 4.2: D_{ij} and L_{ij} coefficients of Eq. (1.65).

Publications

A list of publications resulting from work presented in this thesis is given below.

Publications in refereed journals

1. A. Feijoo, V. K. Magas and A. Ramos, ***The*** $\bar{K}N \to K\Xi$ ***reaction in coupled channel chiral models up to next-to-leading order***, Phys. Rev. C 92 (2015) no. 1, 015206.

2. A. Feijoo, V. K. Magas, A. Ramos and E. Oset, $\Lambda_b \to J/\psi\ K\ \Xi$ ***decay and the higher order chiral terms of the meson baryon interaction***, Phys. Rev. D 92 (2015) no. 7, 076015; ***Erratum***: Phys. Rev. D 95 (2017) no. 3, 039905.

3. E. Oset *et al.*, ***Weak decays of heavy hadrons into dynamically generated resonances***, Int. J. Mod. Phys. E 25 (2016) 1630001.

4. A. Feijoo, V. K. Magas, A. Ramos and E. Oset, ***A hidden-charm*** $S = -1$ ***pentaquark from the decay of*** Λ_b ***into*** $J/\psi\ \eta\Lambda$ ***states***, Eur. Phys. J. C 76 (2016) no. 8, 446.

5. E. Oset *et al.*, ***Study of reactions disclosing hidden charm pentaquarks with or without strangeness***, Nucl. Phys. A 954 (2016) 371.

6. A. Ramos, A. Feijoo and V. K. Magas, ***The chiral*** $S = -1$ ***meson-baryon interaction with new constraints on the NLO contributions***, Nucl. Phys. A 954 (2016) 58.

Non-refereed Publications and Proceedings

1. V. K. Magas, A. Feijoo and A. Ramos, ***Effects of the next-to-leading order terms in the chiral SU(3) Lagrangian on the strangeness -1 s-wave meson-baryon interactions***, arXiv:1311.5025 [hep-ph]. Proceedings of the international conference: New Trends in High-Energy Physics, Alushta, Crimea, September 23 - 29, 2013.

2. V. K. Magas, A. Feijoo and A. Ramos, ***The*** $\bar{K}N \to K\Xi$ ***reaction in coupled channel chiral models up to next-to-leading order***, AIP Conf. Proc. 1606 (2014) 208. Proceedings of the 2^{nd} Russian-Spanish Congress on Particle and Nuclear Physics at all scales and Cosmology, Saint Petersburg, Russia, October 1 - 4, 2013.

3. A. Feijoo, V. K. Magas and A. Ramos, ***Antikaon induced*** Ξ ***production from a chiral model at NLO***, EPJ Web Conf. 81 (2014) 05012. Proceedings of the 13^{th} International Workshop on Meson Production, Properties and Interaction (MESON2014), Cracow, Poland, May 29 - June 03, 2014.

4. V. K. Magas, A. Feijoo and A. Ramos, ***Cascade production in antikaon reactions with protons and nuclei***, doi:10.3204/DESY-PROC-2014-04/170. Proceedings of the 20^{th} International Conference on Particles and Nuclei (PANIC 14), Hamburg, Germany, August 24 - 29, 2014, edited by Alexander Schmidt and Christian Sander.

5. A. Feijoo, V. K. Magas and A. Ramos, ***The Role of High Spin Hyperon Resonances in the*** Ξ ***Production Meson-Baryon Reactions***, J. Phys. Soc. Jpn. -in press. Proceedings of the 12^{th} Conference on Hypernuclear and Strange Particle Physics (HYP2015), Sendai, Japan, September 07 - 12, 2015.

6. V. K. Magas, A. Feijoo, E. Oset and A. Ramos, ***The*** $\Lambda_b \to J/\psi\ K$ ***Cascade decay and the NLO chiral terms of the meson-baryon interaction***, J. Phys. Soc. Jpn. -in press. Proceedings of the 12^{th} Conference on Hypernuclear and Strange Particle Physics (HYP2015), Sendai, Japan, September 07 - 12, 2015.

7. A. Ramos, A. Feijoo and V. K. Magas, ***The*** $\bar{K}N \to K\Xi$ ***Reaction in a Chiral NLO Model***, arXiv:1604.02141. Mini-Proceedings of the Workshop on Physics with Neutral Kaon Beam at JLab (KL2016), Newport News, VA, USA, February 01 - 03, 2016.

8. E. Oset *et al.*, ***Reactions Looking for Hidden Charm Pentaquarks with or without Strangeness***, Acta Phys. Polon. Supp. 9 (2016) 529. Proceedings of the international Winter Workshop Excited QCD 2016, Costa da Caparica, Portugal, March 06 - 12, 2016.

9. E. Oset *et al.*, ***Predictions for pentaquark states of hidden charm molecular nature and comparison with experiment***, EPJ Web Conf. 130 (2016) 06004. Proceedings of the 14^{th} International Workshop on Meson Production, Properties and Interaction (MESON2016), Cracow, Poland, June 02 - 07, 2016.

10. E. Oset *et al.*, ***The*** $\Lambda_b \to J/\psi K^0\Lambda$ ***and*** Λ_b ***into*** $J/\psi\eta\Lambda$ ***Reactions and a Hidden-Charm Pentaquark State with Strangeness***, JPS Conf. Proc. 13 (2017) 020043. Proceedings of the 14^{th} International Conference on Meson-Nucleon Physics and the Structure of the Nucleon (MENU 2016), Kyoto, Japan, July 25-30, 2016.

11. A. Feijoo, V. K. Magas and A. Ramos, ***Constraints on the*** $S = -1$ ***meson-baryon interaction at NLO***, EPJ Web Conf. 137 (2017) 05003. Proceedings of the 12^{th} Quark Confinement and the Hadron Spectrum (CONF12), Thessaloniki, Greece, August 29 - September 03, 2016.

12. V. K. Magas, A. Feijoo, E. Oset and A. Ramos, ***Traces of the hidden-charm*** $S = -1$ ***pentaquark in the*** $\Lambda_b \to J/\psi\eta\Lambda$ ***decay***, EPJ Web Conf. 137 (2017) 06015. Proceedings of the 12^{th} Quark Confinement and the Hadron Spectrum (CONF12), Thessaloniki, Greece, August 29 - September 03, 2016.

Resumen

En esta tesis se ha estudiado la interacción mesón-barión en onda S en el sector $S = -1$ empleando un lagrangiano de $SU(3)$ hasta segundo orden, implementando la unitarización en canales acoplados. La condición indispensable para llevar a cabo un estudio de este tipo, forzosamente, pasa por fijar el valor de los coeficientes presentes en los términos de segundo orden, los cuales no poseen un valor bien determinado.

Generalmente, las constantes de baja energía de los lagrangianos efectivos se obtienen mediante procesos de ajuste a los datos experimentales disponibles. Tradicionalmente, en este sector de extrañeza, dichos parámetros se ajustaban a los datos experimentales de la dispersión K^-p a los canales $\pi\Sigma, \bar{K}N, \pi\Lambda$, así como a las razones entre secciones eficaces en el umbral de producción de K^-p: γ, R_n y R_c; y a los precisos valores del corrimiento y la anchura parcial del estado 1s del hidrógeno kaónico obtenido por la colaboración SIDDHARTA. Lo novedoso en nuestra tesis es la inclusión de datos experimentales procedentes de la reacción de dispersión $K^-p \to K^+\Xi^-, K^0\Xi^0$ en los

procesos de ajuste. La motivación para ello se debe a la especial sensibilidad de estas reacciones a los términos de órdenes superiores, ya que estas reacciones no proceden de manera directa mediante el término WT que es el dominante a primer orden. A esto se le suma el hecho que las contribuciones provenientes de la redispersión de los canales acoplados no es capaz de reproducir adecuadamente los datos experimentales. Dado lo anterior, nos centramos en estudiar los efectos producidos por la inclusión sistemática en el lagrangiano de los términos de segundo orden ("NLO") y los de Born sobre las constantes de baja energía, particularmente sobre coeficientes de "NLO".

La principal diferencia entre los modelos que se obtienen de los ajustes se refleja en las componentes de isospin de la sección eficaz total de las reacciones que aquí se estudian. Así pues, para comprobar la fiabilidad de estos modelos, se llevaron a cabo nuevos ajustes teniendo en cuenta datos experimentales procedentes de reacciones de filtrado de isospin.

Adicionalmente, se han estudiado la estabilidad y la precisión de los parámetros obtenidos de los ajustes añadiendo contribuciones resonantes de manera fenomenológica a aquellas amplitudes de dispersión asociadas a las reacciones que son especialmente sensibles a las correcciones de segundo orden. Debe destacarse que las contribuciones resonantes han proporcionado una mejora del acuerdo entre los modelos teóricos y los datos experimentales.

La desintegración de Λ_b dando lugar a estados que contienen una partícula J/Ψ junto con un par mesón-barión resulta ser un proceso muy interesante para extraer información sobre los parámetros de "NLO" a energías más altas. Además, el proceso $\Lambda_b \to J/\psi\ \eta\Lambda$ nos ha permitido estudiar las implicaciones que tendría la posible existencia de un homólogo extraño del pentaquark con encanto escondido $P_c(4450)$. Las

conclusiones y el análisis de cada capítulo están descritos en los párrafos siguientes.

El Capítulo 2 está dedicado al estudio del papel que juegan los términos de "NLO" y los de Born, así como la relevancia de ciertas reacciones para obtener parametrizaciones más fiables de los coeficientes de "NLO".

Al principio, comparamos diferentes ajustes que se basaban en cálculos unitarizados empleando núcleos de interacción que incluían o no los términos de "NLO" y para los cuales se tenían en cuenta o no los datos experimentales de la reacción de dispersión $K^-p \to K\Xi$. Fruto de los resultados obtenidos de todas estas posibles combinaciones, y más particularmente de la excelente reproducción de los datos experimentales lograda por el modelo **WT+NLO**, se mostró por vez primera que los términos de "NLO" del lagrangiano quiral son absolutamente necesarios para reproducir los datos experimentales de las reacciones $K^-p \to K\Xi$. De este modo, se evidenció la sensibilidad del segundo orden del lagrangiano a las reacciones $K^-p \to K\Xi$. Dada esta sensibilidad junto con el hecho que los datos existentes de la reacción de dispersión $K^-p \to K\Xi$ son limitados y que tienen asociada una gran incertidumbre, para poder dar una respuesta definitiva sobre los valores de los parámetros de "NLO" se requerirían datos experimentales más precisos.

Después, contrariamente a lo que se asumió a cerca del negligible efecto de los términos de Born, demostramos que estas contribuciones no pueden menospreciarse en las reacciones $K^-p \to K\Xi$. Las significativas diferencias en los coeficientes de "NLO" entre la nueva parametrización obtenida para el modelo **WT+NLO+Born** y la que se obtuvo para el modelo **WT+NLO** confirmaron el hecho anterior. A pesar de esto, no se apreció ninguna mejora en la precisión de los parámetros ni en el $\chi^2_{\text{d.o.f.}}$. Este resultado nos condujo a un interesante hallazgo que nos permitió entender cómo dos

parametrizaciones tan diferentes pueden tener una bondad del ajuste tan similar: la inclusión o no de los términos de Born puede modificar notablemente la descomposición en componentes de isospin de la sección eficaz total de la reacción $K^- p \to K\Xi$ debido a su sensibilidad a los términos de orden superior. Tales diferencias entre las componentes de isospin nos llevan a pensar que si nuestros modelos se ajustan a datos experimentales procedentes de reacciones que actúan como selectores de isospin podremos extraer valores más realistas para los parámetros presentes en el lagrangiano.

La mayoría de los datos experimentales empleados en nuestros ajustes vienen de la dispersión protón-antikaón y, consecuentemente, contienen contribuciones tanto de componentes de isospin $I = 0$ como de $I = 1$; siendo la única excepción el canal $\pi^0\Sigma^0$, que filtra isospin 0. Así pues, se decidió ampliar el numero de observables empleados en los ajustes añadiendo datos experimentales de las reacciones de dispersión $K^- p \to \eta\Lambda, \eta\Sigma^0$, las cuales tienen solamente una única componente de isospin para sus secciones eficaces, i. e., isospin 0 y 1 respectivamente. Todos estos esfuerzos culminaron con la obtención del modelo **WT+NLO+Born (η chan)** que, hasta donde sabemos, es el único capaz de reproducir razonablemente bien los datos de la dispersión $K^- p$ a todos los posibles canales del sector $S = -1$. Respecto a los parámetros de este modelo, se puede destacar el papel relevante de estos nuevos datos experimentales a la hora de obtener unos valores muy homogéneos y precisos para las constantes de "NLO" junto con unas constantes de substracción cuyos valores se acercan más a los valores naturales. A la vista de estos resultados, la inclusión en los ajustes de nuevas reacciones donde se filtre el isospin podría favorecer la obtención de valores más realistas para las constantes de baja energía.

La propuesta para medir la reacción $K_L^0 p \to K^+\Xi^0$ en $I = 1$ empleando el haz

secundario de K_L^0 en Jlab podría suponer una fuente de información complementaria a la dispersión K^-p. Se ha presentado una predicción para esta reacción empleando algunos de nuestros modelos de la cual se concluye que, cuantas más contribuciones se tienen en cuenta en el núcleo de interacción y más datos experimentales se incluyen en los ajustes, más cerca estamos de reproducir los dos únicos puntos disponibles para esta reacción. Hay que remarcar que ninguno de estos puntos se ha utilizado en los ajustes. A la luz de estos resultados, parece que nuestros parámetros toman cada vez valores más confiables, particularmente los del modelo **WT+NLO+Born (η chan)**, al cual consideramos nuestro mejor modelo quiral puro.

Con la intención de mejorar la descripción de los datos experimentales de las reacciones $K^-p \to K\Xi$ y $K^-p \to \eta\Lambda$, se incluyeron resonancias de spin alto en estos procesos. Como estas reacciones son las más sensibles a los términos de "NLO", este hecho podría inducir modificaciones en los valores de los coeficientes de "NLO". De este modo, podemos estudiar la estabilidad y presición de los parámetros presentes en los modelos. Este estudio se llevó a cabo en el Capítulo 3.

La primera parte de este estudio consistió en la inclusión explícita de los hyperones de spin alto $\Sigma(2030)$ y $\Sigma(2250)$ en la amplitud de dispersión $K^-p \to K\Xi$, con la intención de fijar una contribución quiral con la cual los términos resonantes puedan interferir para reproducir adecuadamente las estructuras mostradas por los datos experimentales sin tener que forzar a los parámetros de "NLO" a tomar valores sobrestimados. Para calcular la amplitud resonante, hemos utilizado el método de Rarita-Schwinger, mientras que la amplitud quiral se ha calculado empleando un lagrangiano con los términos WT y NLO dando lugar a un nuevo modelo, **NLO+RES**. Como los términos resonantes introducen una dependencia angular en las amplitudes, se de-

cidió aprovechar este hecho para reproducir los datos experimentales de la sección eficaz diferencial con un acuerdo razonable dadas las limitaciones del modelo para ello. De aquí se puede concluir que la inclusión de términos resonantes cumple una doble función. Por un lado, nos permite obtener una mejora global en la descripción de los datos de dispersión, tanto los de las secciones eficaces totales com los de las diferenciales en las reacciones de producción $K\Xi$. Por otro lado, absorbiendo ciertas estructuras de las secciones eficaces, la inclusión de términos resonantes permite encontrar mínimos más estables y, por consiguiente, valores más precisos de las constantes de baja energía del modelo quiral unitario.

Seguidamente, realizamos un estudio similar para el modelo **WT+NLO+Born (η chan)**. Comparado con el anterior, este modelo ha sido ajustado a datos experimentales adicionales (datos de la sección eficaz $K^-p \to \eta\Lambda$). Como esta reacción también es sensible a las contribuciones de "NLO", sus correspondientes coeficientes serán más confiables. Esto hace que el estudio de la estabilidad adquiera un carácter más decisivo. Con esta motivación, se han extendido las contribuciones resonantes a los procesos $K^-p \to \eta\Lambda$, teniendo en cuenta para este caso particular solo la contribución de la resonancia $\Lambda(1890)$. Esta última resonancia ha sido también incorporada, junto con las ya empleadas $\Sigma(2030)$ y $\Sigma(2250)$, a las amplitudes de dispersión $K^-p \to K\Xi$. Los resultados obtenidos confirman lo que ya se había observado con anterioridad: hay una notable mejora en la reproducción de los datos experimentales y los parámetros adquieren valores similares a los del correspondiente modelo sin resonancias. Esta estabilidad es especialmente remarcable para la mayoría de los coeficientes de "NLO".

Habiendo demostrado los efectos de los procesos que filtran isospin sobre los coeficientes de "NLO", en el Capítulo 4 se muestra que la desintegración $\Lambda_b \to J/\psi\ \eta\Lambda$ y,

particularmente, la $\Lambda_b \to J/\psi\ K\Xi$ proporcionan una información interesante relativa a la interacción mesón-barión en el sector $S = -1$ y $I = 0$. La dinámica de esta reacción, en la cual los quarks ligeros que conforman la Λ_b actúan como espectadores, es tal que filtra $I = 0$ en los estados finales. Esto es así, ya que los quarks ud en el barión Λ_b se acoplan necesariamente a isospin 0 y la desintegración débil favorece la transición $b \to c\bar{c}s$; quedando, por lo tanto, un quark s al final del proceso débil, el cual tiene isospin 0 que junto al anterior par ud darán un isospin total $I = 0$. Así pues, estas desintegraciones podrían ofrecer información complementaria a la que se obtiene de los datos de la reacción de dispersión $K^- p \to K\Xi$ cuyas componentes de isospin ($I = 0$ y $I = 1$) se combinan para dar los resultados finales.

Basamos nuestro estudio en los modelos **WT+NLO** (**Model 1**) y **WT+NLO+Born (η chan)** (**Model 2**) que han sido desarrollados en esta tesis para describir la dispersión $K^- p$. Las distribuciones de masa invariante producidas por ambos modelos son diferentes para las desintegraciones de Λ_b a los estados $K\Xi$ y $\eta\Lambda$, siendo a su vez bastante diferentes respecto al espacio fásico, indicando la sensibilidad de estos procesos a la dinámica interna de la interacción fuerte en los estados finales. La diferencia entre modelos es mucho más apreciable en el proceso de desintegración $\Lambda_b \to J/\psi\ K\Xi$. La razón se deriva del hecho que la desintegración en $\eta\Lambda$ puede proceder de manera directa ("tree level"), mientras que para la desintegración de Λ_b que da lugar a una J/ψ no permite una formación del par $K\Xi$ directamente, a no ser que este se produzca via la redispersión de los componentes primarios $\bar{K}N$ y $\eta\Lambda$. Por tanto, la reacción $\Lambda_b \to J/\psi\ K\Xi$ es directamente proporcional a la amplitud de dispersión mesón-barión, concretamente a las componentes de $I = 0$ correspondientes a $\eta\Lambda \to K\Xi$ y $\bar{K}N \to K\Xi$ cuya interferencia puede dar lugar a patrones muy marcados. Estos modelos también predicen diferencias notables para las desintegración Λ_b en las regiones de energéticas

donde se producen los pares $K\Xi$ y $\eta\Lambda$, poniendo de manifiesto que la componente de $I = 0$ de la interacción mesón-barión, que es la única posible por provenir de la desintegración Λ_b, no está bien fijada por los ajustes a los datos experimentales de las reacciones $K^- p \to K\Xi$.

Las dos estructuras halladas recientemente en la distribución de masa invariante $J/\psi p$ de la desintegración $\Lambda_b \to J/\psi K^- p$ que han sido asociadas a dos estados de pentaquark, con su plausible explicación en términos de un estado molecular con un barión y un par $\bar{c}c$, nos llevaron a estudiar la desintegración de la Λ_b en los estados finales $J/\psi\,\eta\Lambda$. La desintegración $\Lambda_b \to J/\psi\,\eta\Lambda$, que puede conectarse en canales acoplados a la desintegración $\Lambda_b \to J/\psi K^- p$, podría tener lugar con la misma intensidad y sería posible observar, en su distribución de masa invariante $J/\psi\Lambda$, un posible compañero extraño de los dos estados de pentaquarks no (extraños) observados por la colaboración LHCb. Conviene tener presente que cuando las resonancias N^* de encanto escondido fueron teóricamente predichas como estados moleculares utilizando varios métodos basados en la unitarización, algunos compañeros extraños como los estados Λ^* fueron encontrados. Aprovechando esta información, hemos predecido qué tipo de señal dejarían estos estados en las distribuciones de masa invariante $\eta\Lambda$ y $J/\psi\Lambda$ de la reacción $\Lambda_b \to J/\psi\,\eta\Lambda$. Hemos visto que tomando los valores de las constantes de acoplamiento del estado Λ^* de encanto escondido a los canales $\bar{D}^{*0}\Xi_c'$ y $J/\psi\Lambda$ obtenidos por los métodos basados en la unitarización, uno observaría una señal clara y con un apreciable pico en la distribución de masa invariante $J/\psi\Lambda$ de la desintegración $\Lambda_b \to J/\psi\,\eta\Lambda$. También se estudió la dependencia de nuestros resultados a cambios razonables en los parámetros que caracterizaban los modelos involucrados en nuestra descripción del proceso, así como la dependencia en las posibles propiedades de dicho pentaquark. En todas los tests que se realizaron, la señal resonante seguía

siendo claramente visible en la distribución de masa invariante $J/\psi\Lambda$. Esto nos hace pensar que en el caso que se llevara a cabo tal experimento podría dar prueba de la existencia de este nuevo estado.

Este trabajo ha sido un primer paso hacia la construcción de un modelo quiral más completo en el sector $S = -1$ que nos será útil para analizar los venideros datos más precisos de la producción $K\Xi$. Además, los hallazgos y características observados en este estudio indican que la medida de observables analizados aquí proporcionaría una información valiosa, hasta ahora novedosa, que enriquecería nuestro conocimiento de la interacción mesón-barión y nos ayudaría a progresar en la comprensión de la dinámica de los hadrones.

Bibliography

[1] J. Gasser and H. Leutwyler, Annals Phys. **158**, 142 (1984).

[2] U. G. Meissner, Rept. Prog. Phys. **56**, 903 (1993).

[3] G. Ecker, Prog. Part. Nucl. Phys. **35**, 1 (1995).

[4] V. Bernard, N. Kaiser and U. G. Meissner, Int. J. Mod. Phys. E **4**, 193 (1995).

[5] A. Pich, Rept. Prog. Phys. **58**, 563 (1995).

[6] S. Scherer, Adv. Nucl. Phys. **27**, 277 (2003).

[7] N. Kaiser, T. Waas, W. Weise, Nucl. Phys. A **612**, 297 (1997).

[8] E. Oset, A. Ramos, Nucl. Phys. A **636**, 99 (1998).

[9] J. A. Oller, U. -G. Meissner, Phys. Lett. B **500**, 263 (2001).

[10] M. F. M. Lutz, E. Kolomeitsev, Nucl. Phys. A **700**, 193 (2002).

[11] B. Borasoy, E. Marco, S. Wetzel, Phys. Rev. C **66**, 055208 (2002).

[12] C. Garcia-Recio, J. Nieves, E. Ruiz Arriola and M. J. Vicente Vacas, Phys. Rev. D **67**, 076009 (2003).

[13] D. Jido, J. A. Oller, E. Oset, A. Ramos and U. G. Meissner, Nucl. Phys. A **725**, 181 (2003).

[14] A. Bahaoui, C. Fayard, T. Mizutani, B. Saghai, Phys. Rev. C **68**, 064001 (2003).

[15] B. Borasoy, R. Nissler, W. Wiese, Eur. Phys. J. A **25**, 79 (2005).

[16] V.K. Magas, E. Oset, A. Ramos, Phys. Rev. Lett. **95**, 052301 (2005).

[17] B. Borasoy, U. -G. Meissner and R. Nissler, Phys. Rev. C **74**, 055201 (2006).

[18] M. Bazzi, G. Beer, L. Bombelli, A. M. Bragadireanu, M. Cargnelli, G. Corradi, C. Curceanu (Petrascu) and A. d'Uffizi et al., Phys. Lett. B **704**, 113 (2011).

[19] Y. Ikeda, T. Hyodo, W. Wiese, Nucl. Phys. A **881**, 98 (2012).

[20] T. Hyodo, D. Jido, Progress in Particle and Nuclear Physics **67**, 55 (2012).

[21] Zhi-Hui Guo, J. A. Oller, Phys. Rev. C **87**, 035202 (2013).

[22] M. Mai and U. G. Meissner, Nucl. Phys. A **900**, 51 (2013).

[23] T. Mizutani, C. Fayard, B. Saghai and K. Tsushima, Phys. Rev. C **87**, 035201 (2013).

[24] L. Roca and E. Oset, Phys. Rev. C **87**, 055201 (2013).

[25] L. Roca and E. Oset, Phys. Rev. C **88**, 055206 (2013).

[26] M. Mai and U. G. Meissner, Eur. Phys. J. A **51**, 30 (2015).

[27] A. Feijoo, V. K. Magas and A. Ramos, Phys. Rev. C **92**, 015206 (2015).

[28] A. Ramos, A. Feijoo and V. K. Magas, Nucl. Phys. A **954**, 58 (2016).

[29] Letter of intent, *Physics Opportunities with Secondary KL beam at JLAB*, LOI-12-15-001.

[30] K. Nakayama, Y. Oh and H. Haberzettl, Phys. Rev. C **74**, 035205 (2006).

[31] J. K. S. Man, Y. Oh and K. Nakayama, Phys. Rev. C **83**, 055201 (2011).

[32] D. A. Sharov, V. L. Korotkikh and D. E. Lanskoy, Eur. Phys. J. A **47**, 109 (2011).

[33] A. Feijoo, V. K. Magas, A. Ramos and E. Oset, Phys. Rev. D **92**, no. 7, 076015 (2015); Erratum: [Phys. Rev. D **95**, no. 3, 039905 (2017)].

[34] A. Feijoo, V. K. Magas, A. Ramos and E. Oset, Eur. Phys. J. C **76**, no. 8, 446 (2016).

[35] J. J. Wu, R. Molina, E. Oset and B. S. Zou, Phys. Rev. Lett. **105**, 232001 (2010).

[36] J. J. Wu, R. Molina, E. Oset and B. S. Zou, Phys. Rev. C **84**, 015202 (2011).

[37] Z. C. Yang, Z. F. Sun, J. He, X. Liu and S. L. Zhu, Chin. Phys. C **36**, 6 (2012).

[38] C. W. Xiao, J. Nieves and E. Oset, Phys. Rev. D **88**, 056012 (2013).

[39] M. Karliner and J. L. Rosner, Phys. Rev. Lett. **115**, no. 12, 122001 (2015).

[40] R. Aaij *et al.* [LHCb Collaboration], Phys. Rev. Lett. **115**, 072001 (2015).

[41] R. Aaij *et al.* [LHCb Collaboration], Chin. Phys. C **40**, no. 1, 011001 (2016).

[42] L. Roca, J. Nieves and E. Oset, Phys. Rev. D **92**, no. 9, 094003 (2015).

[43] S. Weinberg, Physica A **96**, 327 (1979).

[44] C. Patrignani *et al.* [Particle Data Group], Chin. Phys. C **40**, no. 10, 100001 (2016).

[45] G. 't Hooft, Phys. Rept. **142**, 357 (1986).

[46] S. Durr *et al.*, Science **322**, 1224 (2008).

[47] S. R. Beane *et al.*, Phys. Rev. D **84**, 014507 (2011).

[48] W. Bietenholz *et al.*, Phys. Rev. D **84**, 054509 (2011).

[49] S. Aoki *et al.* [PACS-CS Collaboration], Phys. Rev. D **79**, 034503 (2009).

[50] C. Vafa and E. Witten, Nucl. Phys. B **234**, 173 (1984).

[51] B. Kubis, hep-ph/0703274 [HEP-PH].

[52] J. Gasser, H. Leutwyler and M. E. Sainio, Phys. Lett. B **253**, 252 (1991).

[53] R. Koch, Nucl. Phys. A **448**, 707 (1986).

[54] C. B. Dover and G. E. Walker, Phys. Rept. **89**, 1 (1982).

[55] N. Kaiser, T. Waas and W. Weise, Nucl. Phys. A **612**, 297 (1997).

[56] J. A. Oller and E. Oset, Phys. Rev. D **60**, 074023 (1999).

[57] P. C. Bruns, M. Mai and U. G. Meissner, Phys. Lett. B **697**, 254 (2011).

[58] J. A. Oller, E. Oset and A. Ramos, Prog. Part. Nucl. Phys. **45**, 157 (2000).

[59] N. Kaiser, P. B. Siegel, W. Weise, Nucl. Phys. A **594**, 325 (1995).

[60] R. H. Dalitz and S. F. Tuan, Annals Phys. **8**, 100 (1959); R. H. Dalitz and S. F. Tuan, Phys. Rev. Lett. **2**, 425 (1959); M. Jones, R. H. Dalitz and R. R. Horgan, Nucl. Phys. B **129**, 45 (1977).

[61] N. Kaiser, P. B. Siegel and W. Weise, Nucl. Phys. A **594**, 325 (1995).

[62] K. Moriya *et al.* [CLAS Collaboration], Phys. Rev. C **87**, no. 3, 035206 (2013).

[63] K. Moriya *et al.* [CLAS Collaboration], Phys. Rev. C **88**, 045201 (2013).

[64] K. Moriya *et al.* [CLAS Collaboration], Phys. Rev. Lett. **112**, no. 8, 082004 (2014).

[65] I. Zychor, M. Buscher, M. Hartmann, A. Kacharava, I. Keshelashvili, A. Khoukaz, V. Kleber and V. Koptev *et al.*, Phys. Lett. B **660**, 167 (2008).

[66] G. Agakishiev *et al.* [HADES Collaboration], Phys. Rev. C **87**, 025201 (2013).

[67] J. Beringer *et al.* [Particle Data Group], Phys. Rev. D **86**, 010001 (2012).

[68] R. Kaiser and H. Leutwyler, In *Adelaide 1998, Nonperturbative methods in quantum field theory* 15-29 [hep-ph/9806336].

[69] U. G. Meissner, U. Raha and A. Rusetsky, Eur. Phys. J. C **35**, 349 (2004).

[70] J. K. Kim, Phys. Rev. Lett. **14**, 89 (1965).

[71] T. S. Mast, et al., Phys. Rev. D **14**, 13 (1976).

[72] R. O. Bangerter, et al., Phys. Rev. D **23**, 1484 (1981).

[73] J. Ciborowski, et al., J. Phys. G **8**, 13 (1982).

[74] G. Burgun et al., Nucl. Phys. B **8**, 447 (1968).

[75] J. R. Carlson, et al., Phys. Rev. D **7**, 2533 (1973).

[76] P. M. Dauber, et al., Phys. Rev. **179**, 1262 (1969).

[77] M. Haque et al., Phys. Rev. **152**, 1148 (1966).

[78] G. W. London, et al., Phys. Rev. **143**, 1034 (1966).

[79] T. G. Trippe, P. E. Schlein, Phys. Rev. **158**, 1334 (1967).

[80] W. P. Trower, et al., Phys. Rev. **170**, 1207 (1968).

[81] R. J. Nowak et al., Nucl. Phys. B **139**, 61 (1978).

[82] D. N. Tovee et al., Nucl. Phys. B **33**, 493 (1971).

[83] P. G. Ratcliffe, Phys. Rev. D **59**, 014038 (1999).

[84] M. Lampton, B. Margon and S. Bowyer, Astrophys. J. **208**, 177 (1976).

[85] B. C. Jackson, Y. Oh, H. Haberzettl and K. Nakayama, Phys. Rev. C **91**, no. 6, 065208 (2015).

[86] A. Starostin et al. (Crystal Ball Collaboration), Phys. Rev. C**64**, 055205 (2001).

[87] D. F. Baxter et al., Nucl. Phys. B **67**, 125 (1973).

[88] M. Jones et al., Nucl. Phys. B **90**, 349 (1975).

[89] A. Berthon et al., Nuovo Cim. A **21**, 146 (1974).

[90] L. Roca, M. Mai, E. Oset and U. G. Meissner, Eur. Phys. J. C **75**, no. 5, 218 (2015).

[91] T. Aaltonen *et al.* [CDF Collaboration], Phys. Rev. Lett. **106**, 121804 (2011).

[92] R. Aaij *et al.* [LHCb Collaboration], Phys. Rev. Lett. **111**, 102003 (2013).

[93] R. Aaij *et al.* [LHCb Collaboration], JHEP **1407**, 103 (2014).

[94] E. Oset, A. Ramos and C. Bennhold, Phys. Lett. B **527**, 99 (2002); Erratum: [Phys. Lett. B **530**, 260 (2002)].

[95] J.P. Berge *et al.*, Phys. Rev. 147, 945 (1966).

[96] S.A.B.R.E. Collaboration, J.C. Scheuer *et al.*, Nucl. Phys. B **33**, 61 (1971).

[97] B. C. Jackson, H. Haberzettl, Y. Oh and K. Nakayama, EPJ Web Conf. **81**, 05015 (2014).

[98] R. Shyam, O. Scholten and A. W. Thomas, Phys. Rev. C **84**, 042201 (2011).

[99] K. A. Olive *et al.* [Particle Data Group Collaboration], Chin. Phys. C **38**, 090001 (2014).

[100] L. L. Chau, Phys. Rept. **95**, 1 (1983).

[101] L. Wolfenstein, Phys. Rev. Lett. **51**, 1945 (1983).

[102] S. Stone and L. Zhang, Phys. Rev. Lett. **111**, no. 6, 062001 (2013).

[103] W. H. Liang and E. Oset, Phys. Lett. B **737**, 70 (2014).

[104] M. Bayar, W. H. Liang and E. Oset, Phys. Rev. D **90**, no. 11, 114004 (2014).

[105] K. Miyahara, T. Hyodo and E. Oset, Phys. Rev. C **92**, no. 5, 055204 (2015).

[106] J. J. Xie, L. R. Dai and E. Oset, Phys. Lett. B **742**, 363 (2015).

[107] W. H. Liang, J. J. Xie and E. Oset, Phys. Rev. D **92**, no. 3, 034008 (2015).

[108] F. E. Close, "An Introduction to Quarks and Partons", Academic Press, London 1979, p 48.

[109] R. P. Pavao, W. H. Liang, J. Nieves and E. Oset, arXiv:1701.06914 [hep-ph].

[110] C. Albertus, E. Hernndez, C. Hidalgo-Duque and J. Nieves, Phys. Lett. B **738**, 144 (2014).

[111] H. Y. Cheng, C. K. Chua and C. W. Hwang, Phys. Rev. D **69**, 074025 (2004).

[112] R. N. Faustov and V. O. Galkin, Phys. Rev. D **87**, no. 9, 094028 (2013).

[113] A. Khodjamirian, T. Mannel, N. Offen and Y.-M. Wang, Phys. Rev. D **83**, 094031 (2011).

[114] U. G. Meissner and W. Wang, JHEP **1401**, 107 (2014).

[115] C. W. Bauer, D. Pirjol, I. Z. Rothstein and I. W. Stewart, Phys. Rev. D **70**, 054015 (2004).

[116] M. Beneke, G. Buchalla, M. Neubert and C. T. Sachrajda, Phys. Rev. Lett. **83**, 1914 (1999).

[117] M. Beneke, G. Buchalla, M. Neubert and C. T. Sachrajda, Nucl. Phys. B **606**, 245 (2001).

[118] P. Colangelo, F. De Fazio and W. Wang, Phys. Rev. D **81**, 074001 (2010).

[119] U. G. Meissner and W. Wang, Phys. Lett. B **730**, 336 (2014).

[120] B. El-Bennich, A. Furman, R. Kaminski, L. Lesniak, B. Loiseau and B. Moussallam, Phys. Rev. D **79**, 094005 (2009); Erratum: [Phys. Rev. D **83**, 039903 (2011)].

[121] J. T. Daub, C. Hanhart and B. Kubis, JHEP **1602**, 009 (2016).

[122] X. W. Kang, B. Kubis, C. Hanhart and U. G. Meissner, Phys. Rev. D **89**, 053015 (2014).

[123] Y. J. Shi and W. Wang, Phys. Rev. D **92**, no. 7, 074038 (2015).

[124] M. Döring, U. G. Meissner and W. Wang, JHEP **1310**, 011 (2013).

[125] J. -W. Li, D. -S. Du and C. -D. Lu, Eur. Phys. J. C **72**, 2229 (2012).

[126] J. X. Lu, E. Wang, J. J. Xie, L. S. Geng and E. Oset, Phys. Rev. D **93**, 094009 (2016).

[127] W. L. Wang, F. Huang, Z. Y. Zhang and B. S. Zou, Phys. Rev. C **84**, 015203 (2011).

[128] S. G. Yuan, K. W. Wei, J. He, H. S. Xu and B. S. Zou, Eur. Phys. J. A **48**, 61 (2012).

[129] S. Stone, PoS EPS **-HEP2015**, 434 (2015).

[130] R. Chen, X. Liu, X. Q. Li and S. L. Zhu, Phys. Rev. Lett. **115**, no. 13, 132002 (2015).

[131] J. He, Phys. Lett. B **753**, 547 (2016).

[132] U. G. Meissner and J. A. Oller, Phys. Lett. B **751**, 59 (2015).

[133] R. F. Lebed, Phys. Lett. B **749**, 454 (2015).

[134] L. Maiani, A. D. Polosa and V. Riquer, Phys. Lett. B **749**, 289 (2015).

[135] V. V. Anisovich, M. A. Matveev, J. Nyiri, A. V. Sarantsev and A. N. Semenova, arXiv:1507.07652 [hep-ph].

[136] R. Ghosh, A. Bhattacharya and B. Chakrabarti, arXiv:1508.00356 [hep-ph].

[137] V. V. Anisovich, M. A. Matveev, J. Nyiri, A. V. Sarantsev and A. N. Semenova, Int. J. Mod. Phys. A **30**, 1550190 (2015).

[138] H. X. Chen, W. Chen, X. Liu, T. G. Steele and S. L. Zhu, Phys. Rev. Lett. **115**, no. 17, 172001 (2015).

[139] Z. G. Wang, Eur. Phys. J. C **76**, no. 2, 70 (2016).

[140] N. N. Scoccola, D. O. Riska and M. Rho, Phys. Rev. D **92**, no. 5, 051501 (2015).

[141] F. K. Guo, U. G. Meissner, W. Wang and Z. Yang, Phys. Rev. D **92**, no. 7, 071502 (2015).

[142] X. H. Liu, Q. Wang and Q. Zhao, Phys. Lett. B **757**, 231 (2016).

[143] M. Mikhasenko, arXiv:1507.06552 [hep-ph].

[144] Y. Huang, J. He, H. F. Zhang and X. R. Chen, J. Phys. G **41**, no. 11, 115004 (2014).

[145] E. J. Garzon and J. J. Xie, Phys. Rev. C **92**, no. 3, 035201 (2015).

[146] Q. Wang, X. H. Liu and Q. Zhao, Phys. Rev. D **92**, no. 3, 034022 (2015).

[147] V. Kubarovsky and M. B. Voloshin, Phys. Rev. D **92**, no. 3, 031502 (2015).

[148] M. Karliner and J. L. Rosner, Phys. Lett. B **752**, 329 (2016).

[149] H. Y. Cheng and C. K. Chua, Phys. Rev. D **92**, no. 9, 096009 (2015).

[150] G. N. Li, X. G. He and M. He, JHEP **1512**, 128 (2015).

[151] A. Mironov and A. Morozov, JETP Lett. **102**, no. 5, 271 (2015).

[152] T. J. Burns, Eur. Phys. J. A **51**, no. 11, 152 (2015).

[153] H. X. Chen, W. Chen, X. Liu and S. L. Zhu, Phys. Rept. **639**, 1 (2016).

[154] H. X. Chen, L. S. Geng, W. H. Liang, E. Oset, E. Wang and J. J. Xie, Phys. Rev. C **93**, no. 6, 065203 (2016).

[155] E. Wang, H. X. Chen, L. S. Geng, D. M. Li and E. Oset, Phys. Rev. D **93**, no. 9, 094001 (2016).

[156] C. Fernandez-Ramirez, I. V. Danilkin, D. M. Manley, V. Mathieu and A. P. Szczepaniak, Phys. Rev. D **93**, no. 3, 034029 (2016).

[157] E. J. Garzon and E. Oset, Eur. Phys. J. A **48**, 5 (2012).

[158] D. Gamermann and E. Oset, Eur. Phys. J. A **33**, 119 (2007).

[159] K. Terasaki, Prog. Theor. Phys. **118**, 821 (2007).